School of Civil and Mechanical Engineering
Department of Mechanical Engineering

Numerical simulation of the effect of leading-edge tubercles on the hydrodynamic performance of hydrofoils at low and high Reynolds numbers

Peter Johnson

This thesis is presented for the degree of
Masters of Philosophy (Mechanical Engineering)
of
Curtin University

October 2018

[This page has been left blank intentionally]

Declaration

To the best of my knowledge and belief this thesis contains no material previously published by any other person except where due acknowledgment has been made.

This thesis contains no material which has been accepted for the award of any other degree or diploma in any university.

Signature: …….

Date: ……26/10/2018……...

[This page has been left blank intentionally]

Abstract

Despite its immense size, the humpback whale is one of the most acrobatic creatures inhabiting the oceans. It has been theorised that this can be attributed to the use of their pectoral flippers and more specifically the protuberances, also known as tubercles, that can be found along the leading-edges. There has been a growing tendency amongst design engineers to employ the method of biomimicry; imitating a design that exists in nature to solve an engineering problem or improve current systems, specifically in this case, passive flow control. To examine the effect of the tubercles on hydrofoil performance, flow properties were analysed using Computational Fluid Dynamics simulations on hydrofoils based of the NACA 0021 profile (as it closely resembles the cross section of a humpback's flipper) with multiple leading-edge tubercle amplitudes.

The tubercle amplitudes tested were 2.5%, 4%, and 10% of the mean chord length. Reynolds numbers of 120,000, 1,000,000 and 2,770,000 were used to test in both laminar and turbulent flow conditions. Very few studies have explored the effect of fully developed turbulent flow over different leading-edges, which is why two Reynolds numbers over 500,000 were tested. The Spalart-Allmaras turbulence model was used for all simulations, with symmetry boundary conditions at the ends of the hydrofoil. The purpose of this boundary condition was to eliminate tip vortices thereby isolating the tubercles from external influences impacting the flow.

For angles of attack lower than the critical angle, at which stall occurred, the tubercles caused a reduction in lift and an increase in drag in both laminar and turbulent flow. Additionally, in both types of flow, the velocity fields for hydrofoils with tubercles indicated that the flow remained attached at the tubercle peaks post-stall and separated in the troughs at lower angles of attack than the standard hydrofoil. For laminar flow simulated around the hydrofoils, post-stall, the coefficients of lift were much greater for hydrofoils with leading-edge tubercles compared to straight leading-edges, indicating that the tubercles provided additional lift. By contrast, the hydrofoils with leading-edge protuberances simulated in fully turbulent flow conditions, had lift coefficient values lower than those generated from the hydrofoil with a uniform leading-edge, pre- and post-stall. The values of lift decreased linearly post-stall for the unmodified hydrofoil as the angle of attack increased. The hydrofoil with the most

efficient hydrodynamic characteristics in turbulent flow (at high Reynolds number) was the unmodified hydrofoil as it had higher stall angles, mostly higher lift and lower drag values than hydrofoils with tubercles along the leading-edges.

Acknowledgements

The Author would like to extend gratitude to Dr James Jewkes, for providing knowledge in the fields of Computational Fluid Dynamics and Fluid Mechanics, and guidance for the first year of this project.

Thank you also to Dr Her Mann Tsai, whose expertise and advice about simulations throughout the first year pushed me to continuously improve on my work.

Thank you to Dr Andrew King who, assisted on my connection to the Magnus Super computer and was a great source of information whenever the author was perplexed.

The Author would like to give sincerest and greatest appreciation to Dr Julien Cisconni, who not only took over guidance once Dr Jewkes left, but gave advice, time and fresh ideas constantly. Thank you all for the roles you played in the Author's academic development.

The Author would also like to acknowledge Mrs Lison Johnson for her constant love, motivation and support during the course of the Masters of Philosophy (Mechanical Engineering) course. None of this would have been possible without you.

This work was supported by resources provided by The Pawsey Supercomputing Centre with funding from the Australian Government and the Government of Western Australia

[This page has been left blank intentionally]

Contents

List of Figures

[This page has been left blank intentionally]

List of Tables

[This page has been left blank intentionally]

Nomenclature

A=Surface area (m^2)

c=Mean chord length (m)

C_f =Friction coefficient (dimensionless)

C_p =Pressure coefficient (dimensionless)

C_l =Lift coefficient (dimensionless)

C_d =Drag coefficient (dimensionless)

D=Drag force (N)

k=Turbulent kinetic energy (m^2/s^2)

L=Lift force (N)

M=Mach number (dimensionless)

p=Pressure (Pa)

p_∞=Ambient pressure (Pa)

Re=Reynolds number based on chord length (dimensionless)

U_∞=Free-stream velocity (m/s)

x, y, z=Cartesian coordinate (m)

α=Angle of attack (°)

Γ=Vortex strength (circulation) (m^2/s)

ρ=Fluid density (kg/m^3)

λ=Wavelength (m)

τ_{wall}=Wall shear stress (Pa)

ν=Kinematic viscosity (m^2/s)

ν_t=Turbulent kinematic viscosity (m^2/s)

$\tilde{\nu}$ = *Spalart-Allmaras Variable (dimensionless)*

ω=*Specific turbulence dissipation (1/s)*

1.0 Introduction

Flow manipulation and control are important research topics in many fields of engineering, including hydrodynamics, aeronautics, and aerospace. Controlling the properties of a flow such as velocity, pressure, cavitation, and boundary layer separation, is essential for engineers to design useful fluid flow systems and to ensure proper operation of these systems. In recent years, researchers have focussed their investigations on biomimicry, in which designs of components are inspired by Nature.

Certain creatures, usually those which fly or swim, use passive or active control mechanisms to influence surrounding flow for enhanced propulsion, manoeuvrability or even stealth. Through biomimicry, there have been several recent advancements in fluid flow control. Examples of this include the Shinkansen Bullet Train which was made quieter, faster and more energy efficient with the remodelling of its front nose inspired by the beak of the kingfisher [1], and the shark skin riblets on the hulls of sailboats which reduce skin friction drag [2]. For this study, the aim was to contribute to the improvement of the hydrodynamic efficiency of hydrofoils using passive flow control mechanisms derived from the design of the humpback whale's pectoral flippers.

1.1 Humpback Whales

The humpback whale (*Megaptera Novaeanglia*) is one of the largest creatures on the planet and yet remains one of the most acrobatic in the ocean. It is a large mammal of the baleen whale family, cetacean species, that primarily inhabits the colder waters of the Southern Hemisphere, except during mating season when they migrate up the coast of Western Australia to tropical waters to give birth. They are typically between 50-80 tonnes in mass, 12-16 metres long when fully grown and can swim at a maximum velocity of approximately 7.2 m/s (see tables 1 and 2). The dynamic performance of any marine mammal in an aquatic environment is characterised by its inherent ability to control the flow of water around its body [3]. Like most sub-surface dwellers, the humpback whale benefits from features acting as passive flow control devices, such as the large barnacle-like protuberances, or tubercles, located along the leading-edge of

the pectoral flippers. The location of these tubercles corresponds to the positions of the cartilages of the manus [4]. The placement of the leading-edge tubercles is not the same for every whale as they correspond to the individual bone and cartilage structure of each humpback. The size of the tubercles decreases towards the tip of the flipper (see figures 2 and 3).

Figure 1: Humpback whale breaching [5]

The pectoral flippers, common to all cetacean mammals, provide hydrodynamic lift for manoeuvring. Humpback whales have the largest pectoral flippers of any cetacean species measuring up to 4.62 metres in length (see table 1), with the second largest belonging to the blue whale with a maximum length of 4 metres. These flippers typically have a span that is 28-33% of the total body length, which allows the whales to perform sharp turning circles only 1.5 meters in diameter [4]. The amplitude of the tubercles along the pectoral flipper range from 2.5% of the chord length at the tip to 12% of the chord length close to the shoulder, with the spacing between the tubercles ranging from 10% to 50% of the chord length [6].

The flippers can serve many functions by their design such as navigation in shallow waters, body thermoregulation (thin fin theory) and the production of signals towards other members of the pod by slapping the surface of the water. Per Fish and Battle (1995) [4], the pectoral flippers can be thought of as control surfaces which can create

force imbalances for manoeuvrability and maintain stability by allowing the humpbacks to "grip" the fluid as they turn. The manoeuvrability benefits provided by the unique design of the humpback's flippers is thought to be particularly important whilst the whale hunts. Unlike other cetacean mammals, humpback whales have two different styles of hunting, one associated with group feeding and another associated with individual feeding.

Table 1: Characteristics of the humpback whale morphology

Characteristic	**Value**
Average Adult Weight	50 – 80 t
Average Flipper Chord Length	0.704 m
Average Flipper Span	3.92 - 4.62 m
Average Body Length	14 m

When hunting in groups, humpback whales use a technique adopted exclusively by this species called "bubble netting". In this strategy, a single humpback from the pod will dive to a depth of approximately 50 meters, below a school of krill or small fish. It then begins circling the prey from below blowing bubbles to form a cylinder of air. During this process, the diameter of the circles formed by the whales gradually becomes smaller and smaller (up to 1.5m in diameter) as the circling whale rises forcing the krill closer to the surface. The rest of the pod will create whistles and clicks to confuse the prey. Once the school is sufficiently grouped together within the air cylinder at the surface, the humpbacks rise through the centre of the circle opening their jaws and catching everything inside. Upon breaching the surface of the water, they use the baleen at the forefront of their mouth to filter out the ocean keeping only the krill. A humpback whale does not create a bubble net when hunting alone. Instead, it will lunge at its prey in a sudden burst of speed to take it by surprise. This feeding method is simply called lunging (for velocity when feeding see table 2). The large surface area of the pectoral flippers (see figure 2) create a high Aspect Ratio (AR) (calculated by the square of the flipper span divided by the flipper surface area). The high aspect ratio flippers are also favoured for high velocity banking turns (similar to the ones made by humpbacks during bubble net feeding), due to their typically high

lift-to-drag ratio [4]. Although flexible and cartilaginous (whilst still containing bones), flippers remain flexed and immobile during feeding.

Figure 2: Pectoral flippers including tubercle leading-edge [7]

Table 2: Velocity characteristics and corresponding Reynolds numbers based on chord length of pectoral flippers

Characteristic	**Value**	**Reynolds Number**
Maximum Velocity	7.2 m/s	2,770,000
Average Velocity whilst Singing	0.684 m/s	263,000
Average Velocity when not Singing	1.11 m/s	427,000
Average Velocity during feeding	2.6 m/s	1,000,000

1.2 Hydrodynamics of Pectoral Fins

It has been hypothesised that the tubercles located on the pectoral flippers are a form of passive flow control devices. The experiments published in Miklosovic et al (2004) [8], demonstrated that the presence of tubercles on a hydrofoil caused an improvement in lift and a reduction in drag as well as increasing the angle of attack at which stall occurs. As the angle of attack increases flow separation starts to occur, beginning at the trailing edge as the adverse pressure gradient becomes too large for the fluid to maintain forward momentum. At a critical angle of attack, the flow separation occurs at the leading-edge of the hydrofoil, causing a sudden loss of lift and increase in drag. This is known as stall.

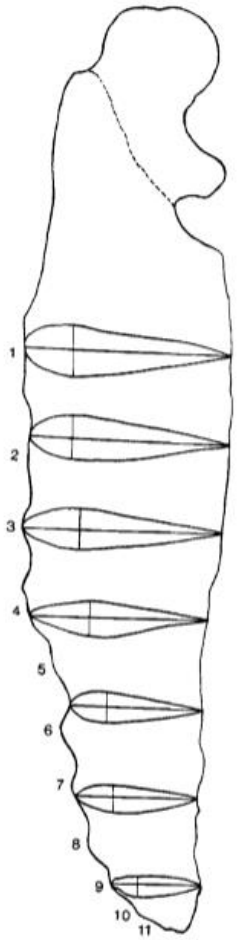

Figure 3: Pectoral flipper; top view with cross sectional shapes [8]

Initially, there were two theories which were developed to explain the benefit brought by the tubercles. The first theory suggested that the tubercles channel the flow over the pectoral flippers between the troughs of the protuberances, creating a faster flow which in turn lowers the pressure on the top surface resulting in higher lift. In the following, it is referred to as the flow channelling theory. This theory was developed after reviewing the work by Fish and Battle (1995) [4] which suggests that tubercles may channel the flow between the tubercles as a method of passive flow control. In keeping with the conservation of mass law, as the mass flow rate needs to remain constant through a system, the velocity of the flow must increase as the cross-sectional area in the spanwise direction (z-axis) that the fluid flows through decreases. The velocity inside the channel (between the tubercles), being greater in magnitude than in the freestream, and a reduction in the pressure along the top surface, acts to energise the flow (and subsequently the boundary layer) so that it remains attached to the top surface of the fin closer to the trailing edge. By delaying flow separation, the tubercles are thought to be able to increase the angle of attack at which stall occurs.

The second theory explored, which in the following is referred to as the vortex generator theory, postulated that the tubercles generate vortices at the leading-edge which causes boundary layer excitation delaying flow separation, thereby resulting in additional lift and reduced drag. Vortex generators are small elements such as dimples or ridges that create stream wise vortices forcing high-momentum fluid towards a solid surface. This increases the amount of energy in the boundary layer close to the surface resulting in delayed separation under conditions that would otherwise cause the fluid to move away from the surface [9]. A prime example of this can be seen in the dimples found on a golf ball. By exciting the boundary layer around the balls surface, separation is delayed allowing a reduction in drag. However, Skillen et al. (2014) [10], Rostamzadeh et al. (2014) [11] and Hansen et al. (2016) [12] have shown that, whilst the result of counter-rotating vortices exists for both hydrofoils with vortex generators and leading-edge tubercles, the underlying mechanism for creating them was vastly different. The tubercles are simply too large to act directly on the boundary layer of the flow.

In both the flow channelling and vortex generation theories, the flow patterns induced by the tubercles are thought to delay stall by energising the flow on the top surface of the pectoral fin. According to Rostamzadeh et al. (2014) [11], the tubercles affect the flow over the hydrofoil by creating regions of higher streamwise vorticity which energise the boundary layer. By extension, this phenomenon also delayed the flow separation and consequently stall. Therefore, it was theorised that the advantages of the leading-edge tubercles could be attributed to the streamwise vorticity. This theory will be examined later in Section 4.6.

1.3 Hydrodynamic Analysis of the Pectoral Flipper

1.3.1 Initial Observations

One of the earliest papers exploring drag reduction through bio-mimicry was the article by Bushnell and Moore (1991) [13]. In it, they discuss the unique leading edge of the tubercles on humpback whales' pectoral flippers and their role as a method of passive flow control which would diminish the effect of the tip flow on the overall dynamics. It also discusses the differences between skin-friction drag reduction and form drag reduction.

Fish and Battle (1995) [4] was the first to carry out an in-depth investigation on the leading-edge tubercles of the humpback whale and their role of flow control device providing more effective manoeuvrability in water. In this study, the pectoral flipper of a humpback whale was cut into 71 sections to record the cross-sectional geometry of the flipper and create an accurate model. This contribution has allowed detailed discussion on the flipper dimensions and has been used as reference data to create equivalent NACA hydrofoil models (see figure 3). Future simulations in the field have been largely based on this model.

1.3.2 Experimental and Numerical Analysis

Fish and Lauder (2006) [14] contained experimental data from tests conducted on the performance of humpback whale tubercles. Similar to the paper by Miklosovic et al. (2004) [8], Fish and Lauder (2006) [14] built a scale model for the purpose of performing flow experiments over the hydrofoil with tubercles along the leading-edge. It was found that the tubercles increase the possible angle of attack without stall by 4^0. In addition, the drag coefficient was found to be reduced by the presence of tubercles and the lift coefficient was significantly increased.

Johari et al. (2007) [15] examined and analysed how altering the size and frequency of tubercles on the leading-edge might affect the coefficients of lift, drag and moments. It also discussed flow separation and stall. For this paper, a NACA 63_4-021 airfoil was

used as the standard shape differing from many articles in this field which used the NACA 0021 or NACA 0020 model. Water tunnel tests were carried out on a standard airfoil as well as airfoils with protuberances ranging in amplitude from 2.5 to 12% of the total chord length and wavelengths from 25 to 50% of the total chord length meant to mimic the ranges of the size found on the humpback's pectoral flipper (see figure 4). It was found through the experiment that foils with tubercles did not stall the same way as the baseline airfoil. They generate less lift at angles of attack smaller than the stall angle [15]. Flow visualisation showed that flow over tubercles remained attached to the airfoil past the post stall angle of the standard mould, however, flow separation was observed mainly in the tubercle troughs with wavelength having a negligible influence on the flow separation. [15]

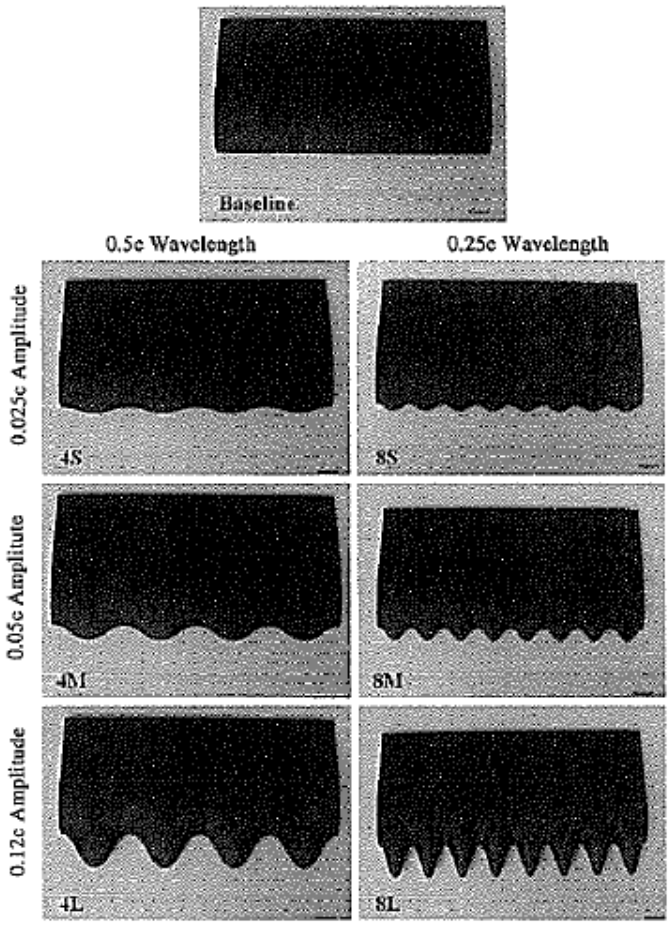

Figure 4: Airfoils with sinusoidal leading-edge protuberances taken from Johari et al. (2007) [15]

Watts and Fish (2001) [3] re-examined the research done on aquatic mammals. Although not dedicated solely to the species, a large portion of the document was

concerned with the unique design of the humpback's pectoral flipper. It described its physical attributes in detail such as the elliptical shape and high aspect ratio. It discussed how the morphological complexities on the flippers could be a way of reducing or using pressure variation at the tip to decrease drag, increase lift and prevent tip stall [3].

The leading-edge control devices are able to maintain lift and avoid stall at higher angles of attack and lower velocities. Drag reductions of up to 7.5% on a "wavy bluff body" were recorded when compared to a smooth leading-edged airfoil. It was found that lift was maintained after a lesser stall i.e. at higher angles of attack without a substantial drop in the lift coefficient, however the maximum value of lift did not increase as a result from the presence of protuberances along the leading-edge. The CFD model showed a different hydrodynamic performance as indicated by the flow patterns and a panel method revealed a 4.8% increase in lift, a 10.9% induced drag reduction and a lift to drag ratio increase of 17.6% for wing sections with a tubercle leading-edge. These results were taken for an angle of attack of 10° (pre-stall conditions) [3].

The last findings in this paper were consistent with other research presented in this field, that the separation of the fluid from the airfoil was delayed due to an increase in the pressure gradient on the suction side which locally reduced the adverse pressure gradient (see figure 5). The top surface of the hydrofoil had an adverse pressure gradient over a large area as minimum pressure was near the leading edge, where the flow velocity was highest, increasing towards the trailing edge. Additionally, in keeping with the results presented in the paper by Van Nierop et al. (2008) [16], the bumps altered the pressure distribution along the hydrofoil span such that separation of the boundary layer was delayed behind the bumps leading ultimately to a gradual onset of stall. Watts and Fish (2001) [3] concluded by claiming that there was a strong possibility that results from research on marine mammals can be directly applicable to the design of water vehicles and aircraft since both operate at similar Reynolds numbers, additionally stating that the advantages of passive flow control in engineering include the elimination of costly high-maintenance and heavy control mechanisms whilst improving performance [3].

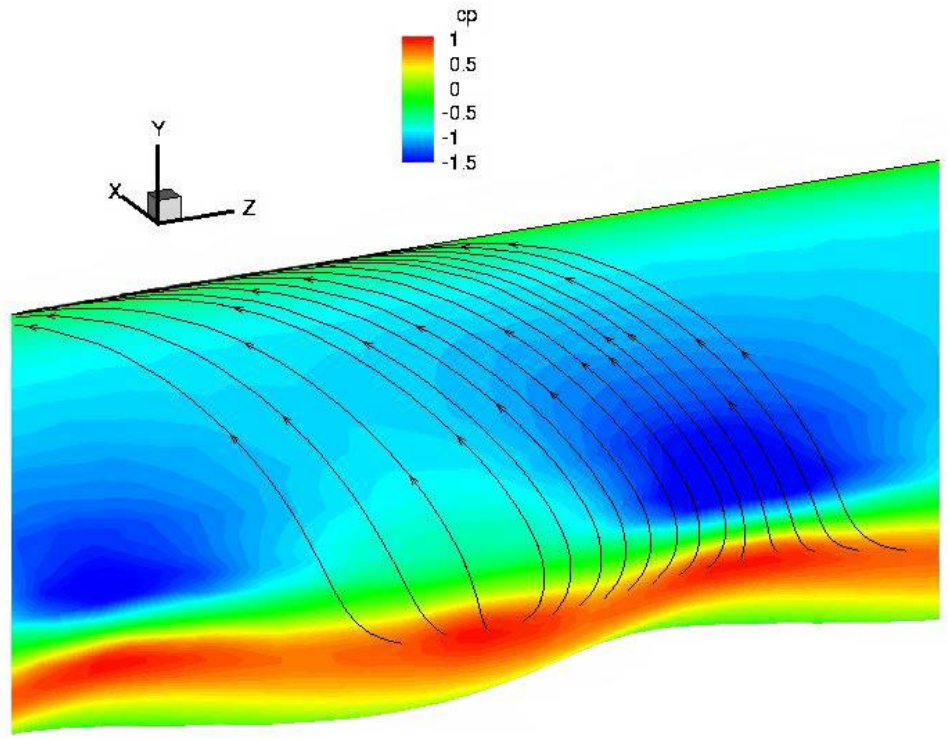

Figure 5: Surface pressure distribution and streamlines over an airfoil with a sinusoidal leading-edge taken from Watts and Fish (2001). [3]

The use of the Prandtl Lifting Line Theory as a modelling approach to predicting the overall lift and drag characteristics of an airfoil with a non-linear leading-edge was first considered in a paper by Rostamzadeh et al. (2013) [17]. The paper compared the Prandtl Lifting Line Theory to results from wind tunnel tests of undulated leading-edged airfoils and results generated in a CFD simulation. In the simulation, strong counter-rotating vortices in the wake of the foil pre-stall were reported to have been observed. The paper concluded that the Prandtl Lifting Line Theory successfully demonstrated that tubercles induce fluctuating vortices along the span and that the modified leading-edge is worth further investigation particularly post stall. [17]

Post stall, airfoils with a non-linear leading-edge showed higher lift coefficients (up to 50%) than that of a standard airfoil. In one case the lift coefficient was nearly constant from 10^0 to 26^0 angle of attack. Airfoils with tubercles had larger drag coefficients pre-stall. Post stall, leading-edge geometry does not appear to have a notable influence on the drag coefficient. Hence lift to drag ratio post stall increases significantly in the presence of leading-edge protuberances. It was also concluded that the frequency of

the undulations played a minor role on the force and moment coefficients, however the amplitude was highly influential.

The numerical study by Pedro and Kobayashi (2008) [18] explored the performance of modified NACA 0020 airfoils, with Reynolds numbers ranging from 500,000 to 520,000 using Detached Eddy Simulation (DES). Pedro and Kobayashi (2008) [18] used simulations of the airfoils built by Miklosovic et al. 2004 [8]; one with an unmodified leading-edge and one with a sinusoidal leading-edge as shown in figure 6, in an effort to produce the same results as the physical experiments. A series of simulations were conducted with attack angles ranging from 0° to 18° and an inlet velocity of 60m/s. The coefficients of lift and drag from the numerical study were compared with the experimental results from Miklosovic et al. (2004) [8] with strong agreement between the two validating the accuracy of the model. The study concluded that the Reynolds number influenced the type of separation observed on the flipper and that the higher aerodynamic performance of the scalloped flipper was due to the presence of stream-wise vortices, due to the leading-edge tubercles.

1.3.3 Conflicting Results

Contrary to Johari et al. (2007) [15], Miklosovic et al. (2004) [8] showed the tubercles affecting the fluid behaviour in a very different manner. The experiments were performed in a wind tunnel, using a NACA0020 airfoil as the base model in an incompressible fluid environment, on an idealised model of a humpback's left pectoral flipper. Two models were manufactured, one with a smooth leading-edge and the other with a scalloped leading-edge as can be seen in figure 6. The scalloped leading-edge flipper serves to delay the stall by generating greater lift at higher incidence angles. Higher lift is generated at the peak and lower drag, which is an evolutionary advantage to the humpback whale whilst hunting, manoeuvring and feeding. The results generated by the tubercles were similar to those of vortex generators typically found a third of the chord length along airplane wings. The tubercles were found to delay the stall angle by approximately 40%, increasing the coefficient of lift by 6%, lowering the drag coefficient by as much as 31% and improving peak performance from L/D=22.5 at $\alpha=7.5^0$ to L/D=23.2 at $\alpha=7.5^0$.

By contrast, Johari et al. (2007) [15] predict poor performance in the pre-stall region. The change in influence, that the presence of a scalloped leading-edge had on the airfoil performance post-stall between the studies, could be explained by the differences in the shape of the airfoils used and the magnitudes of the Reynolds numbers.

The airfoils used by Miklosovic et al. (2004) [8] are based on the NACA 0020 model, closely resembling a humpback flipper and are fixed at one end of the span whereas the airfoils used in Johari et al. (2007) [15] are based on the NACA 63_4-021 model, have uniform mean chord lengths and are fixed at both ends. Therefore, the flow behaviour of the fluid pre- and post-stall would be significantly different. Another difference between the two studies is the Reynolds number. In [15] the Reynolds number was 183,000 (less than 500,000) thus the flow was laminar/transitional whereas in [8] the Reynolds number was 505,000 (greater than 500,000) making the flow fully turbulent. Boundary layer separation occurs more readily in laminar flow since the fluid flow in the boundary layer closest to the surface of the airfoil is not as energised compared with turbulent flow, which is the reason airfoils (and hydrofoils) have poorer aerodynamic (and hydrodynamic) performance in laminar flow.

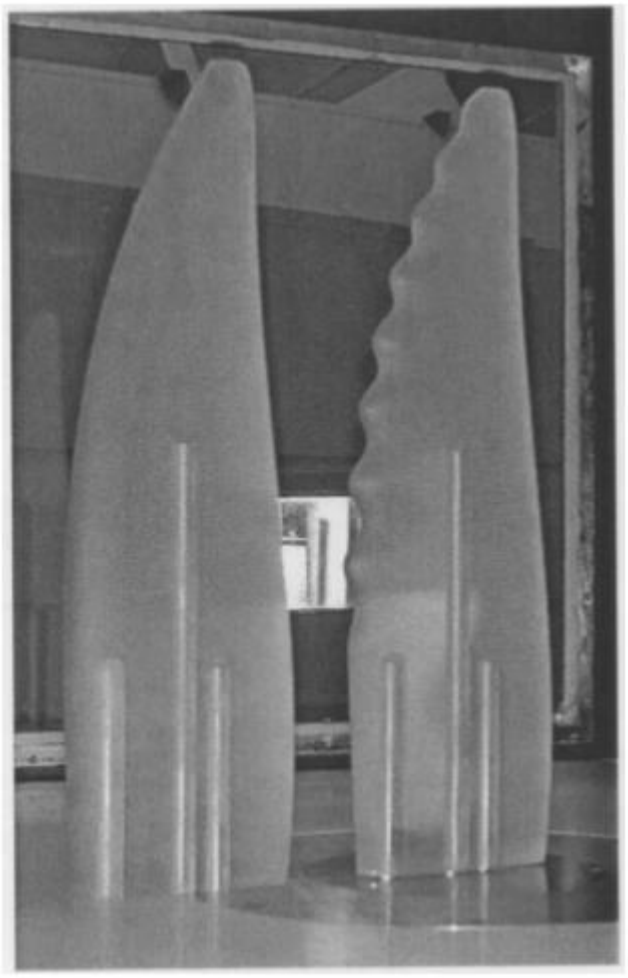

Figure 6: Hydrofoils based on pectoral flipper and NACA 0020 shape with a smooth leading-edge (left) and scalloped leading-edge (right) [8]

Since the publication of Bushnell and Moore (1991) [13], hydrodynamic researchers have been fascinated with the humpback's pectoral flipper leading-edge design. Although many experiments have been conducted on hydrofoils with tubercle leading-edge patterns, none have conclusively proven how the protuberances influence the fluid flow. Most of the experiments were performed in wind/water tunnels and do not explore the different effects of laminar and turbulent flow fields on hydrodynamic performance.

1.4 Objectives

Most previous experiments in water or wind tunnels and theoretical modelling on hydrofoils (or airfoils) with leading-edge tubercles have been performed at low Reynolds numbers, with the exceptions of Rostamzadeh et al. (2017) [19] or Pedro and Kobayashi et al. (2008) [18]. In the two previously mentioned studies, in-depth analysis was performed on airfoils with different leading-edges at Reynolds numbers which would indicate turbulent flow conditions (500,000 – 550,000). What is excluded from these studies, are comparisons between these results and data collected from testing the same airfoils in different conditions (laminar/transitional flow). In addition, the airfoils are not tested in Reynolds numbers above 1,000,000.

Most cases examining flow with Computational Fluid Dynamics (CFD) simulations (using either LES or RANS), examine a slow-moving flow with a low Reynolds number not being truly representative of the flow conditions for a humpback whale swimming. In addition, using CFD to analyse the flow is predominantly found as a component of a larger study and therefore is usually only tested for one set of tubercles on the leading-edge or for a single set of boundary conditions. The CFD simulations have been run to compare with the results of the physical model and therefore are run in the same laminar flow conditions with low Reynolds numbers (less than 500,000).

Experiments in turbulent flow conditions on hydrofoils with tubercles have not been performed extensively due to the limitations of the wind and water tunnels.

This study focuses on the effects of the protuberances along the hydrofoil's leading-edge in both laminar and turbulent flow fields for tubercles of varying amplitudes. The possibility of tip vortices was eliminated by simulating hydrofoils with an infinite span. Four different hydrofoils were tested under laminar and turbulent flow conditions using OpenFOAM to create the simulations.

The primary objectives for this project were to:

- Perform CFD simulations using boundary conditions and parameters based on previous wind/water tunnel experiments on airfoils/hydrofoils to demonstrate the validity of the employed numerical approach in predicting the values of lift, drag, pressure and wall shear stress.
- Analyse the impact of altering the amplitude of the leading-edge tubercles on the flow around a NACA 0021 hydrofoil.
- Simulate hydrofoils with different leading-edge tubercle magnitudes at Reynolds numbers over 500,000 to ensure fully turbulent flow and compare the changes in the hydrodynamic characteristics of the hydrofoils, the stall angle of attack and the flow behaviour.

The third objective was the focus for this study as CFD simulations and physical experiments have not been performed extensively at high Reynolds numbers (as mentioned previously). High Reynolds numbers correspond to the hunting speeds of the humpback whale. As this is theorised to be when tubercles are most useful, it is important to observe the change in hydrodynamic properties of the hydrofoil under these flow conditions. Fully turbulent flow-based simulations that have been conducted previously, primarily contain tubercles of a singular amplitude and do not explore the effects of different tubercle magnitudes and types of flow such as in Rostamzadeh et al. (2017) [19] and Pedro and Kobayashi et al. (2008) [18].

[This page has been left blank intentionally]

2.0 Modelling and Theory

2.1 Navier-Stokes Equations

The Navier-Stokes equations are found by incorporating the viscous effects into the general equations of fluid motion. The governing principles of fluid flow can be represented by the mathematical equations of the conservation laws of physics; that the mass and energy of a fluid are always conserved. Additionally, the momentum of each fluid particle is equal to the sum of the forces on a fluid particle as per Newton's second law.

Using these laws, the physical properties of a fluid particle can be described along the Cartesian coordinates (x, y, z). The Navier-Stokes equations were built on the Newtonian model of viscous stresses within the fluid medium. The motion of any fluid may be described in three dimensions using a system of four partial differential equations [20]. For a Newtonian fluid, the viscous stresses are proportional to the rates of deformation. The compressible fluid sets of equations are not used in this report as the flow is simulated as incompressible. For an incompressible fluid with a constant density, the equation to describe the conservation of mass in the system is given by:

$$\frac{du}{dx} + \frac{dv}{dy} + \frac{dw}{dz} = 0 \qquad \text{Eq.1}$$

Substituting Eq.1 into the momentum equations in the x, y and z directions, respectively, gives:

$$\rho\left(\frac{du}{dt} + u\frac{du}{dx} + v\frac{du}{dy} + w\frac{du}{dz}\right) = -\frac{dp}{dx} + \rho g_x + \mu\left(\frac{d^2u}{dx^2} + \frac{d^2u}{dy^2} + \frac{d^2u}{dz^2}\right) \qquad \text{Eq.2}$$

$$\rho\left(\frac{dv}{dt} + u\frac{dv}{dx} + v\frac{dv}{dy} + w\frac{dv}{dz}\right) = -\frac{dp}{dy} + \rho g_y + \mu\left(\frac{d^2v}{dx^2} + \frac{d^2v}{dy^2} + \frac{d^2v}{dz^2}\right) \qquad \text{Eq.3}$$

$$\rho\left(\frac{dw}{dt}+u\frac{dw}{dx}+v\frac{dw}{dy}+w\frac{dw}{dz}\right)=-\frac{dp}{dz}+\rho g_z+\mu\left(\frac{d^2w}{dx^2}+\frac{d^2w}{dy^2}+\frac{d^2w}{dz^2}\right) \quad \text{Eq.4}$$

Equations 2 to 4 are the Navier-Stokes equations and are the basis for all Computational Fluid Dynamics simulations.

2.2 Reynolds Decomposition

Reynolds decomposition is a mathematical technique to separate an instantaneous quantity into a time averaged part and a time fluctuating part [21]. For instance, with the velocity component *u* described in a 3-D Cartesian coordinate system.

$$u(x,y,z,t)=\overline{u(x,y,z)}+u'((x,y,z,t) \quad \text{Eq.5}$$

Where:

- u is the instantaneous velocity
- u' is the velocity fluctuation at a given time
- $\bar{u}$ is the average (steady) velocity

The Navier-Stokes equations can be altered by substituting in the velocity values as the steady velocity and the velocity fluctuations. When the velocity fluctuations are integrated over a total time-period, the resultant must be equal to zero. The equation which comes as the product of this method, contains non-linear terms called the *Reynolds stresses* which is how the turbulence present in the flow is modelled.

2.3 External Forces Acting on the Hydrofoil

The forces acting on the hydrofoil were analysed for comparison to those from previous experiments and to test the change in hydrodynamic characteristics of the hydrofoil as conditions changed. Figure 7 illustrates the external forces acting on the hydrofoil. The change in momentum of the fluid particles impacting the hydrofoil surface creates a force acting on the body which in figure 7 has been labelled as the Resultant. The vertical and horizontal components of this force are the lift and drag respectively. The lift always acts perpendicular to the direction of the flow and the drag always acts parallel to the direction of the flow. The friction forces (found from the wall shear stresses) act along the hydrofoil as a result of the fluid flowing over the surface. The lift, drag, pressure and the wall shear stress (caused by the friction) are defined in equations 6–9, expressed as non-dimensional coefficients.

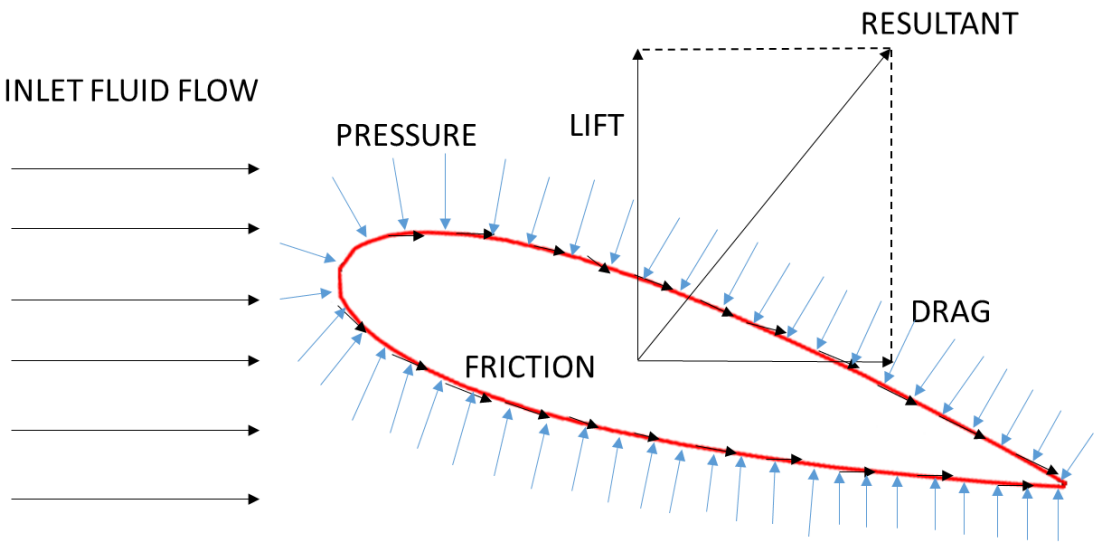

Figure 7: Hydrofoil Free Body Diagram

Lift is proportional to the density of the fluid and proportional to the velocity squared. The magnitude of lift generated is higher if the fluid does not separate from the surface. Wing tip vortices contribute to the total lift as well for finite hydrofoils. For the research conducted in this paper dimensionless values, called coefficients, are used for

the measuring of the strength of the forces acting on the hydrofoil. The lift coefficient is given by equation 6 below.

$$C_l = \frac{L}{\frac{1}{2}\rho_\infty {U_\infty}^2 A} \qquad \text{Eq.6}$$

Drag force always acts in the direction of the flow. There are several forms of drag such as skin friction drag which results from the surface roughness of the solid object immersed in the flow, parasitic drag due to passive flow control elements and form drag (or pressure drag) which occurs as a result of the pressure differential between the front and rear surfaces. In laminar flow, pressure drag is generally high and friction drag is low whereas in turbulent flow pressure drag is low and friction drag is high. Total drag increases with boundary layer separation in both laminar and turbulent flow.

$$C_d = \frac{D}{\frac{1}{2}\rho_\infty {U_\infty}^2 A} \qquad \text{Eq.7}$$

The pressure of the fluid acting on the hydrofoil changes with fluid density, flow velocity and the angle of attack. The pressure coefficient is used as it is a non-dimensional property. The pressure value used in equation 8 is the relative pressure between the pressure at the point of measurement and the freestream pressure. As pressure is measured in Pascals and therefore the result is independent of the surface area of the hydrofoil.

$$C_p = \frac{p - p_\infty}{\frac{1}{2}\rho_\infty {U_\infty}^2} \qquad \text{Eq.8}$$

The wall shear stress is the stress resulting from the frictional forces incurred by the flow and the viscosity of the fluid. The non-dimensional value in equation 9 is the

friction coefficient, which is what was measured for the current study to examine the friction lines on the surfaces of the hydrofoils.

$$C_f = \frac{\tau_{wall}}{\frac{1}{2}\rho_\infty {U_\infty}^2} \quad \text{Eq.9}$$

2.4 Finite and Infinite Hydrofoil

Symmetry boundary conditions were set at either end of the span of the hydrofoils used in simulations for the current study making them infinite. Hydrofoils of infinite span will have different hydrodynamic characteristics than finite hydrofoils as finite hydrofoils have tip vortices which are eliminated in an infinite span. Tip vortices are circular patterns of rotating fluid caused by the pressure differential between the bottom and top surfaces of the hydrofoil when lift is generated [22]. Without tip vortices, for the unmodified hydrofoil cases, there would not be any flow along the span. With the addition of tubercles at the leading edge, counter rotating vortices will be generated downstream of the sinusoids on the suction side of the hydrofoil (see Rostamzadeh et al. (2014) [11]. Vortices also increase the parasitic drag of the hydrofoil.

The Prandtl lifting line theory predicts the lift on an airfoil (with a span of length b) by superimposing an infinite number of theoretical vortices, all with the theoretical vortices coincident along a single line known as the *lifting line*. According to the Kutta-Joukowski theorem a vortex filament of strength Γ which is somehow fixed at a location in the flow will experience a lift force shown in Eq. 10

$$L = \rho_\infty V_\infty \Gamma \quad \text{Eq.10}$$

The downwash induced by the vortices can be represented mathematically by:

$$w(y) = -\frac{\Gamma}{4\pi}\frac{b}{\left(\frac{b}{2}\right)^2 - y^2} \qquad \text{Eq.11}$$

Which resulted in w approaching -∞ as y approached –b/2 or b/2. This issue was resolved by the superimposition of an infinite number of vortices as shown in figure 8.

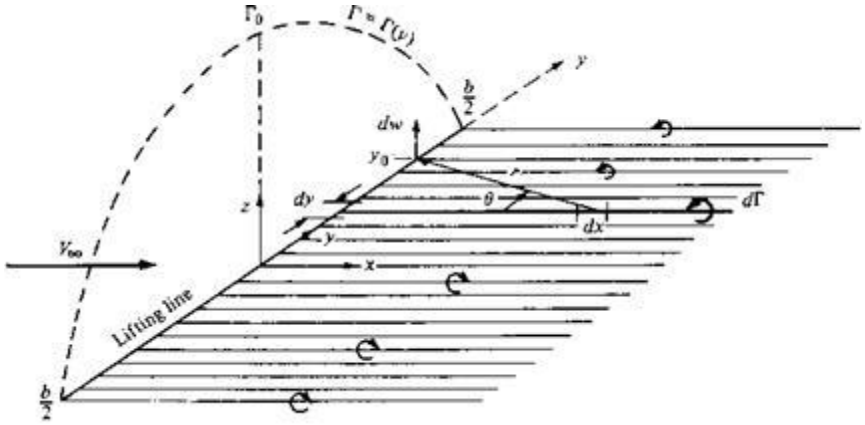

Figure 8: Superposition of an infinite number of horseshoe vortices along the lifting line [22]

Taking an infinitesimally small segment, dy, located at the coordinate y where the circulation is Γ(y), the change in circulation over the segment dy is Γ(y) = (dΓ/dy) dy. The downwash induced by the trailing vortex located at y can be integrated at y_0 to give:

$$w(y_0) = -\frac{1}{4\pi}\int_{-b/2}^{b/2}\frac{\left(\frac{d\Gamma}{dy}\right)dy}{y_0 - y} \qquad \text{Eq.12}$$

The induced angle of attack α_i is given by:

$$\alpha_i(y_0) = -\frac{w(y_0)}{V_\infty} = \frac{1}{4\pi V_\infty}\int_{-b/2}^{b/2}\frac{\left(\frac{d\Gamma}{dy}\right)dy}{y_0 - y} \qquad \text{Eq.13}$$

Equation 13 is an expression for the induced angle of attack in terms of the circulation distribution Γ(y) along the wing. This equation shows the importance of the relationship between the angle of attack and the resultant vortex strength. The lift coefficient for the airfoil section located at y_0 is shown below:

$$C_l = \alpha_0\left[\alpha_{eff}(y_0) - \alpha_{L=0}\right] = 2\pi\left[\alpha_{eff}(y_0) - \alpha_{L=0}\right] = \frac{2\Gamma(y_0)}{V_\infty c(y_0)} \qquad \text{Eq.14}$$

Substituting Eq.14 into Eq.13, solving for α_{eff}, and rearranging gives:

$$\alpha(y_0) = \frac{\Gamma(y_0)}{\pi V_\infty c(y_0)} + \alpha_{L=0}(y_0) + \frac{1}{4\pi V_\infty}\int_{-b/2}^{b/2}\frac{\left(\frac{d\Gamma}{dy}\right)dy}{y_0 - y} \qquad \text{Eq.15}$$

Equation 15 is the fundamental equation of Prandtl's lifting-line theory. The equation states that the geometric angle of attack is equal to the sum of the effective angle plus the induced angle of attack expressed in terms of Γ and an integral containing dΓ/dy. The effective angle of attack for the leading edge of modified hydrofoils will be different at the same geometric angle of attack given the sinusoidal pattern, i.e. the effective angle of attack at the peak will differ from that of the trough. The lift and drag coefficients can therefore be represented by equations 16 and 17.

$$C_l = \frac{L}{q_\infty S} = \frac{2}{V_\infty S}\int_{-b/2}^{b/2}\Gamma(y)dy \qquad \text{Eq.16}$$

$$C_d = \frac{D_i}{q_\infty S} = \frac{2}{V_\infty S}\int_{-b/2}^{b/2}\Gamma(y)\alpha_i(y)dy \qquad \text{Eq.17}$$

2.5 Boundary Layer and Separation

The boundary layer of a fluid flow is the small region close to a surface where the flow is retarded because of the friction between the solid surface and the fluid. The viscosity of the fluid causes friction as it passes over a surface, with the fluid particle layer in direct contact with the surface stopping, resulting in the 'no slip condition'. The boundary layer velocity varies from 0 at the surface to 99% of the free-stream velocity at the edge of the boundary layer (see figure 9).

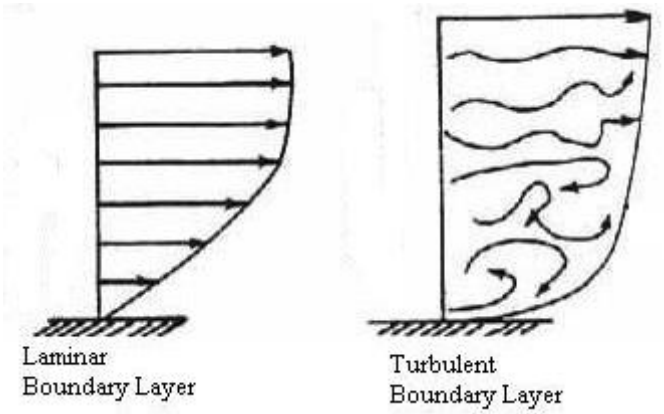

Figure 9: Boundary layer velocity profile for laminar and turbulent flow [22]

The different profiles in figure 9 are for laminar and turbulent flow. As can be seen, the streamlines in the laminar flow are all parallel whereas the streamlines in the turbulent flow are orientated randomly but with a higher average velocity in the direction of the flow. As the flow becomes turbulent the boundary layer profile becomes steeper close to the wall. As the fluid travels further over the surface the velocity of the flow is reduced by the friction imposed on the fluid by the surface. As the adverse pressure gradient increases over the hydrofoil top surface due to a combination of the shape of the hydrofoil and angle of attack, the kinetic energy of the fluid particles in the boundary layer will decrease and the flow will slow down.

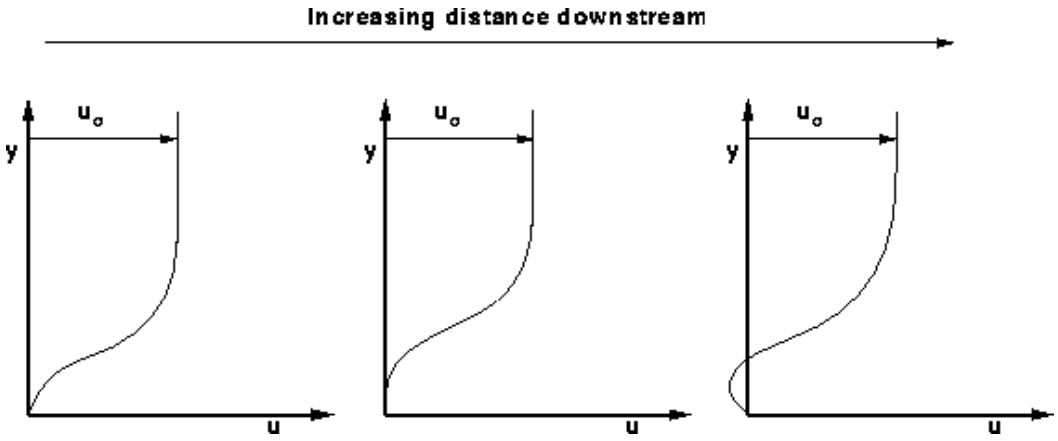

Figure 10: Change in velocity profile with wall boundary layer separation [9] in an adverse pressure gradient

If within the adverse-pressure-gradient region, (see figure 10), the flow is insufficiently energised to surmount the pressure hill, the motion of the fluid particles nearest to the wall will halt. At some point along the flow, the viscous layer "breaks away" from the wall surface as the adverse pressure gradient causes the flow to reverse. The fluid layer closest to the wall then leaves the bounding surface and the boundary layer has been classed as separated. This causes a significant increase in pressure drag and loss of lift.

At separation, the rotational flow region next to the wall abruptly thickens, the normal velocity component increases, and the boundary-layer approximations are no longer valid. Additionally, at separation, a back flow is created from the adverse pressure gradient. Back flow occurs once the pressure gradient becomes strong enough to cause the fluid close to the surface of the hydrofoil to flow in the opposite direction to the ambient flow (see figure 10). Flow separation causes large energy losses to occur within the system which often limits the performance ability of devices. It is therefore of crucial importance to understand and control the boundary layer separation, to enhance performance efficiency. Boundary layer separation is more likely to occur in laminar flow as the flow in the boundary layer has less momentum than in turbulent flow and hence a lower adverse pressure gradient causes stall.

2.6 Computational Fluid Dynamics

Computational fluid dynamic simulations resolve the motion of fluids using a wide variety of models of fluid motion. The three most widely used formulations in research are Direct Numerical Simulation (DNS), Large Eddy Simulation (LES) and Reynolds Averaged Navier-Stokes (RANS) Equations. According to Mahesh et al. 2012 [23], in recent years, the detail to which flow fields can be resolved have improved dramatically. Additionally, the flow simulations have progressed forward from Reynolds Averaged Navier-Stokes computations to be replaced more frequently by Direct Numerical Simulation or Large Eddy Simulations. For this reason, both DNS and LES were given consideration as a method of simulation for the current study.

2.6.1 Direct Numerical Simulation (DNS)

Of the three traditional simulation methods, Direct Numerical Simulation or DNS is the most accurate as the Navier-Stokes equations are solved numerically without any turbulence model. This means that the entire range of spatial and temporal scales of the turbulence must be resolved in the computational mesh. The biggest drawbacks of this method are the requirements for a very fine mesh, the extended run to reach convergence (which increases rapidly with higher Reynolds numbers) and the processing power required to produce results, since without a turbulence model the whole range of temporal and spatial scales of turbulence must be resolved. As the time-averaged flow was of primary interest, the use of this method was deemed unnecessary to obtain useful data and hence was not selected for simulating the flow as it would have been far too time consuming for a project requiring over 100 simulations.

2.6.2 Large Eddy Simulation (LES)

Large Eddy Simulations (LES) are generally reserved for complex and irregular shapes. In LES the idea is to reduce the computational cost of DNS by reducing the range of time-scales and length-scales which are being solved by filtering the Navier-Stokes equations. Although faster in processing than the DNS model, LES would still

have had a large processing time in addition to requiring a more refined mesh. A hybrid of LES and RANS was briefly considered as a viable alternative however the computational time required for that method still would not have been practical and hence LES was not used for the simulations.

2.6.3 Reynolds Averaged Navier-Stokes (RANS)

The Reynolds Averaged Navier-Stokes (RANS) equations (see Section 2.7 for equations) are the most commonly used of the CFD formulations. The reason that the RANS model is sufficient for most engineering purposes, is that the majority of the time, for problems solved in CFD, the programmer is primarily concerned with the time-averaged properties of the flow. Many prior computational studies which have been focussed on the modifications of airfoils and hydrofoils using passive leading-edge flow control elements have used RANS (see [3], [8], [14], [15], [17], [10]). After careful consideration (which will be covered in detail in Section 3.4.4) RANS equations were selected for use in the CFD model of the flow.

2.7 Reynolds Averaged Navier-Stokes Equations

For use in the Reynolds Averaged Navier-Stokes equations, the value of the fluctuating component goes to zero as the results are time averaged and over any measured period the fluctuating total must equal zero [21]. Using the Reynolds decomposition, the Navier-Stokes equations can be expressed as:

$$\rho\left(\frac{d\bar{u}}{dt}+\bar{u}\frac{d\bar{u}}{dx}+\bar{v}\frac{d\bar{u}}{dy}+\bar{w}\frac{d\bar{u}}{dz}\right)=\rho g_x-\frac{d\bar{p}}{dx}+\mu\Delta\bar{u}-\rho\left(\frac{d\overline{u'u'}}{dx}+\frac{d\overline{u'v'}}{dy}+\frac{d\overline{u'w'}}{dz}\right) \quad \text{Eq.18}$$

$$\rho\left(\frac{d\bar{v}}{dt}+\bar{u}\frac{d\bar{v}}{dx}+\bar{v}\frac{d\bar{v}}{dy}+\bar{w}\frac{d\bar{v}}{dz}\right)=\rho g_y-\frac{d\bar{p}}{dy}+\mu\Delta\bar{v}-\rho\left(\frac{d\overline{v'u'}}{dx}+\frac{d\overline{v'v'}}{dy}+\frac{d\overline{v'w'}}{dz}\right) \quad \text{Eq.19}$$

$$\rho\left(\frac{d\bar{w}}{dt}+\bar{u}\frac{d\bar{w}}{dx}+\bar{v}\frac{d\bar{w}}{dy}+\bar{w}\frac{d\bar{w}}{dz}\right)=\rho g_z-\frac{d\bar{p}}{dz}+\mu\Delta\bar{w}-\rho\left(\frac{d\overline{w'u'}}{dx}+\frac{d\overline{w'v'}}{dy}+\frac{d\overline{w'w'}}{dz}\right)$$

Eq.20

or in reduced general form:

$$\rho\frac{D\overline{u_i}}{Dt}=\rho g_i-\frac{d\bar{p}}{dx_i}+\mu\Delta\overline{u_i}-\rho\left(\frac{d\overline{u_i{}'u_j{}'}}{dx_j}\right)$$

Eq.21

Where $\left(\frac{d\overline{u_i{}'u_j{}'}}{dx_j}\right)$ is the Reynolds-stress term [22] and $-\rho\overline{u_i{}'u_j{}'}$ is the Reynolds stress.

Therefore:

$$\tau_{Reynolds}=-\rho\overline{u_i{}'u_j{}'}=\mu_t\frac{d\bar{u}}{dy}$$

Eq.22

Where:

$$\mu_t=\rho*\nu_t$$

Eq.23

- μ_t is the turbulent dynamic viscosity
- ρ is the density of the fluid
- ν_t is the turbulent kinematic viscosity

2.8 RANS Turbulence Models

Prior to the selection of Spalart-Allmaras as the turbulence model used in the study, other models considered for calculating turbulent viscosity were k-ε, k-ω and k-ω SST which are all two equation models. The k-ε turbulence model is commonly used in RANS for turbulent flow conditions, where k is the turbulent kinetic energy and ε is the dissipation of turbulence energy. The k-ε model focuses primarily on the mechanisms which affect turbulent kinetic energy, with the underlying assumption that the turbulent viscosity is isotropic [20]. This model however, has low accuracy when predicting the turbulence in flows with high adverse pressure gradients, curved boundary layers and rotating flows, all of which make it an inappropriate choice for the flow close to the hydrofoil [20].

The k-ω turbulence model is a two-equation model which predicts turbulence by two partial differential equations for the variables k and ω. As with the k-ε model, k is the turbulence kinetic energy and ω is the specific rate of dissipation for the turbulence kinetic energy into internal thermal energy [20]. This model is better than the k-ε model for predicting results with high adverse pressure gradients, rotating flows or results of a curved boundary layer. The problem with this model is the high processing time.

A k-ω SST model combines k-ε and k-ω so that k-ω is used close to a surface and k-ε is used in the free stream flow, such that the model with higher accuracy is used in critical locations and the other model helps resolve the unimportant areas, such as the free flow area, faster that if the k-ω model was solely used. The k-ω SST model was the first turbulence model used in this study to generate results, however, the results were found to be inaccurate and the simulations were taking many time steps to converge or else not reaching convergence at all. The alternative turbulence model used was the Spalart-Allmaras model which is discussed further in Section 2.9.

2.9 Spalart-Allmaras Equations

The Spalart-Allmaras model is a one equation model for turbulent viscosity. The Spalart-Allmaras model was used however as it provided faster results which have a higher chance of reaching convergence in a CFD simulation as it is a linear eddy viscosity model [24]. Additionally, it was a model designed specifically for wall boundary layer flows and gave good results for boundary layers subjected to an adverse pressure gradient. It solves a transport equation for the turbulent kinematic viscosity v_t and the variable $\tilde{\nu}$ (nu tilde also known as the Spalart-Allmaras variable) which can be calculated by:

$$\nu_t = \tilde{\nu}\left(\frac{\left(\frac{\tilde{\nu}}{\nu}\right)^3}{\left(\left(\frac{\tilde{\nu}}{\nu}\right)^3 + {C_{v1}}^3\right)}\right) \qquad \text{Eq.24}$$

Where:

$C_{v1} = 7.1$

According to [8], the value of the Spalart-Allmaras variable is between 3 to 5 times that of the turbulent kinematic viscosity. Therefore, for the purpose of this report let:

$$\tilde{\nu}_{freestream} = 3\nu_{freestream} \qquad \text{Eq.25}$$

Taking the ratio between them to be 3 and substituting in the values, equation 25 above becomes:

$$\nu_t = \tilde{\nu}\left(\frac{(3)^3}{((3)^3 + 7.1^3)}\right) \qquad \text{Eq.26}$$

Therefore:

$$\nu_t = \tilde{\nu}*0.0701 \quad \text{Eq.27}$$

Equation 28 determines the characteristics of the flow according to the Spalart-Allmaras model.

$$\frac{d\nu}{dt} + u_j \frac{d\hat{\nu}}{dx_j} = 0.1355(1 - f_{t2})\hat{S}\hat{\nu} - \left[3.239 f_w - \frac{0.1355}{0.41^2} f_{t2}\right]\left(\frac{\hat{\nu}}{d}\right)^2 + \frac{3}{2}\left[\frac{d}{dx_j}\left((\nu + \hat{\nu})\frac{d\hat{\nu}}{dx_j}\right) + 0.622\frac{d\hat{\nu}}{dx_i}\frac{d\hat{\nu}}{dx_i}\right. \quad \text{Eq. 28}$$

Where:

$$f_{t2} = 1.2\exp\left(-0.5\left(\frac{\tilde{\nu}}{\nu}\right)^2\right) \quad \text{Eq.29}$$

$$g = \min\left[\frac{\tilde{\nu}}{0.41^2\hat{S}d^2}, 10\right] + 0.3\left(\left(\min\left[\frac{\tilde{\nu}}{0.41^2\hat{S}d^2}, 10\right]\right)^6 - \min\left[\frac{\tilde{\nu}}{0.41^2\hat{S}d^2}, 10\right]\right) \quad \text{Eq.30}$$

$$f_w = g\left[\frac{65}{g^6+64}\right]^{\frac{1}{6}} \quad \text{Eq.31}$$

$$S = \Omega + \frac{\tilde{\nu}}{0.41^2 d^2} \quad \text{Eq.32}$$

Ω is the magnitude of the vorticity and d is the distance from the field point to the nearest wall.

[This page has been left blank intentionally]

3.0 Methodology

The simulations of the flow around the different hydrofoils were created using the open sourced software OpenFOAM v 3.0.1 on the Linux based operating system Xubuntu, to model time averaged flow over hydrofoils with unmodified leading-edges and with sinusoidal leading edges. Two tubercles, beginning and ending at the trough, were included in the model of sinusoidal leading-edge hydrofoils at several incidence angles. To capture the laminar and turbulent natures of the flow, the Spalart-Allmaras model was employed, the transport equations for this model can be found in Section 2.8. A C-Grid topology with hexahedral elements was constructed to designate the computational domain. The angle of attack (α) was changed at the inlet via the velocity components and symmetry boundaries were assigned to the side planes to simulate the flow over a section of hydrofoil with infinite span.

3.1 Geometry

Based on [4], [8], [17] and [25], it was concluded that the NACA 0021 airfoil profile (see figure 11) of chord length *c*, closely resembled the pectoral flipper of the humpback whale (see figure 12). A NACA 0021 hydrofoil has a symmetrical cross section mirrored along the x axis (see figure 11) and has a maximum thickness of 0.21c located at 0.3c from the leading-edge. The humpback's maximum thickness for its pectoral flipper has been measured to be between 20 and 28% of the chord length [8].

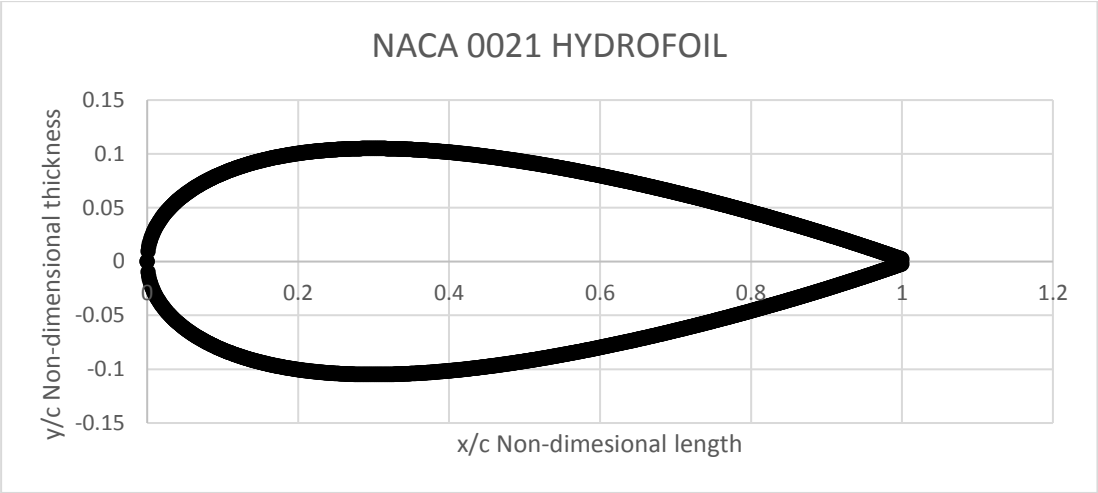

Figure 11: NACA 0021 hydrofoil cross-section profile

Figure 12: Cross-section of a humpbacks' pectoral flipper [14].

The NACA 0021 profile was used to generate hydrofoils in 2-D and 3-D. Four 3-D geometries were designed, one with a uniform leading-edge and 3 with different leading-edge tubercle profiles. All leading-edge profiles generated can be represented by equation 33 which corresponds to the sinusoid along the leading-edge of the hydrofoil in figure 13. The tubercles were generated with a wavelength of 30/70c, which is approximately 0.43c in keeping with the leading-edge protuberances generated in Rostamzadeh et al. (2013) [17], and all hydrofoils had a mean chord length of 1 as measured from the centreline (mean) of the sinusoids to the trailing edge.

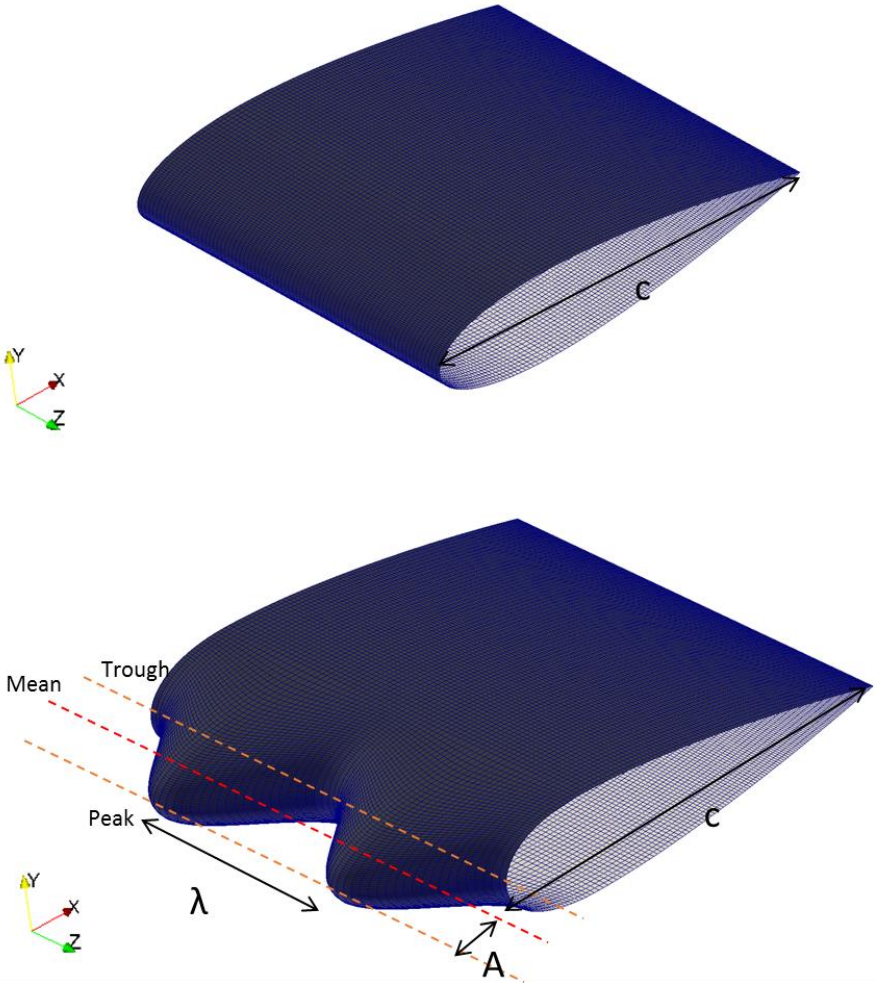

Figure 13: Unmodified hydrofoil and hydrofoil with a sinusoidal leading-edge profile

$$x(z) = A * \cos\left(\left(\frac{1}{\lambda}\right) * \pi * z\right) - A \qquad \text{Eq.33}$$

Where:

- A=Amplitude in meters
- λ=Wavelength of the leading-edge tubercles as measured from peak to peak in metres.

The first 3-D model was of a hydrofoil with an unmodified leading-edge. The unmodified leading-edge was used to establish base line values for the lift and drag results and to compare with the results generated in 2-D. For the first simulation with tubercles along the leading-edge, the design was modelled after a leading-edge tubercle profile found along a uniform airfoil in source [17], with an amplitude of 5.71%. This size was selected as it corresponded to a wind tunnel test performed on a hydrofoil with the same leading edge in source [17]. Throughout the study the magnitude of the wavelength of the sinusoidal tubercles remained constant for comparison of the hydrodynamic performances of the hydrofoils. This is important to note as reducing the wavelength, (up to a point), leads to improvements in the lift characteristics including the results pre-stall, post-stall and the critical angle. Similarly, increasing the wavelength would lead to a decrease in the values of lift at each attack angle according to the results from Hansen et al. (2011) [26].

The other two tubercle amplitudes used were 2.5% and 10% of the chord length (see table 8). It was hypothesised that the 2.5% leading-edge tubercles would give the closest results to the standard hydrofoil results when it came to lift, drag and to boundary layer separation. This size is also approximately equal to the smallest tubercle-to-fin-width ratio that is present along the leading-edge of a humpback's pectoral flipper and so is a pertinent size for experimentation in a study based on humpback whale biomimicry.

For tubercles of amplitude 10% of the chord length, the hypothesis was that the fluid would be forced to flow between the tubercles to be much faster than the fluid in the freestream. This size would cause the flow channelling effect to have greater impact on the hydrodynamic properties of the hydrofoil in comparison to the vortices generated at the tips of the hydrofoil. As the largest observed amplitude of tubercles found on the leading-edge of a pectoral flipper is 12.5% which are the tubercles furthest from the tip close to the whales' body, the 10% chord amplitude was used, as it is within parameters of what is found in Nature.

Table 3: Comparison of leading-edge profiles

Leading-edge Profiles	**Tubercle Amplitude (% of c)**
Unmodified Hydrofoil	0
Hydrofoil with Leading-edge for Validation [17]	5.71
Hydrofoil with Leading-edge Tubercles at an Amplitude of 4% of Total Chord Length	4
Hydrofoil with Leading-edge Tubercles at an Amplitude of 2.5% of Total Chord Length	2.5
Hydrofoil with Leading-edge Tubercles at an Amplitude of 10% of Total Chord Length	10

3.2 Mesh Generation

The meshing of the flow domain around the different hydrofoils was done using the blockMesh utility. Two-dimensional simulations were created first to check that the mesh and boundary conditions would give useable data without a high time cost. The leading edge was created by interpolating the points in the z axis along a sinusoidal equation (Eq. 33). A structured C-mesh was used around the hydrofoil, so the blocks were perpendicular to the hydrofoil surface as can be seen in figure 14.

The curves at the front of the hydrofoil were created by interpolation from the leading edge to the maximum thickness at 0.3c. There is a larger concentration of blocks at the leading and trailing edges of the hydrofoil. The 3-D mesh cells used were hexahedrons. The size of the cells in the y-direction needed to be smaller than the boundary layer thickness so that the change in the mean velocity within the boundary layer could be measured and hence, a y^+ value of less than 1 was required [17]. To accommodate this, the layer of blocks next to the hydrofoil surface was refined until the desired y^+ value was reached. The 2-D mesh contained 55,316 cells and the y^+ values after mesh refinement ranged from a minimum of 0.00788864 to a maximum of 0.519126 with an average value of 0.218109. Figure 14 is shown from the perspective of the x-y plane with x values increasing towards the right of the page, y values increasing towards the top of the page and z values increasing coming out of the page.

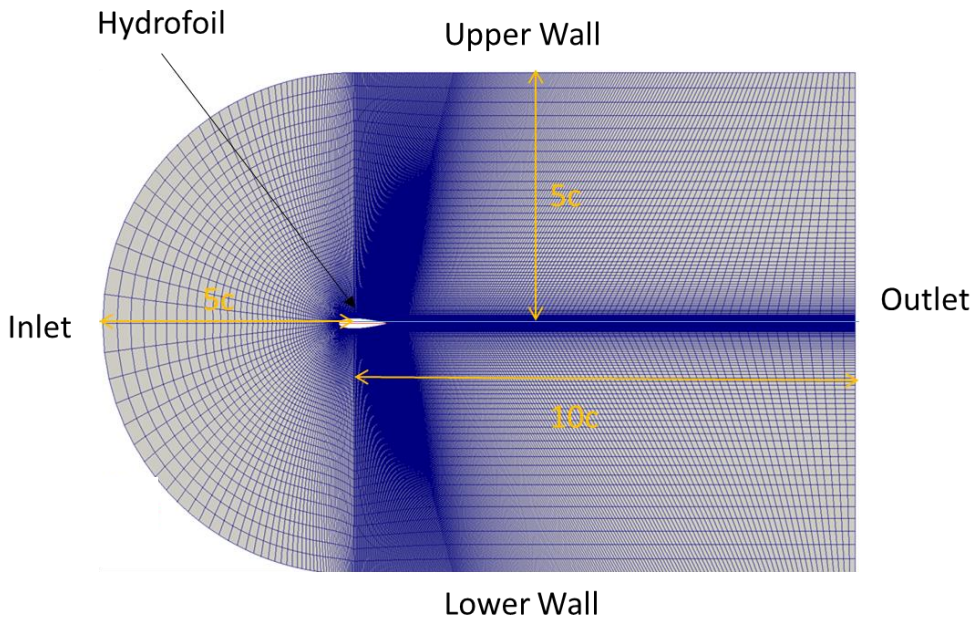

Figure 14: Wireframe representation for the 2-D mesh around NACA 0021 hydrofoil

Changing from 2-D to 3-D simulations, the cell count increases from 55,316 to 4,425,280 as the z-axis cell count was increased from 1 to 80.

Figures 15 and 16 show the wireframe meshes of all the different leading-edges used from top and isometric views. As can be seen from the figures, the blocks along the surface are all quadrilaterals. The cell concentration along the y-axis remained the same for 3-D simulations.

A mesh independence study was conducted to establish a mesh independent solution. Of the generated grids, the one with the total number of nodes equal to 55,000 for 2-D and 4,400,000 for 3-D proved to be sufficient for grid independence (see Section 4.1.4).

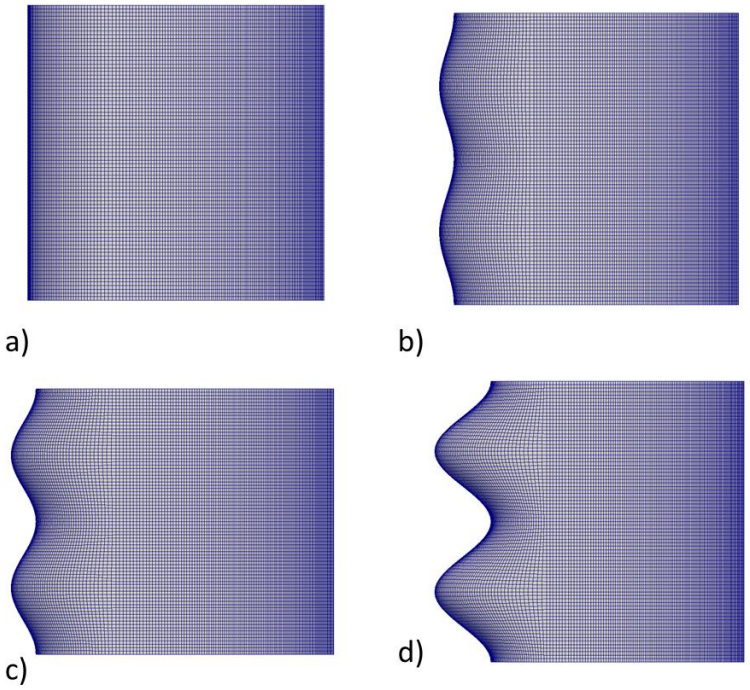

Figure 15: Hydrofoil models generated in 3-D (top view) standard leading-edge (a), amplitudes 2.5% of the chord length (b), 4% of the chord length (c), 10% of the chord length (d)

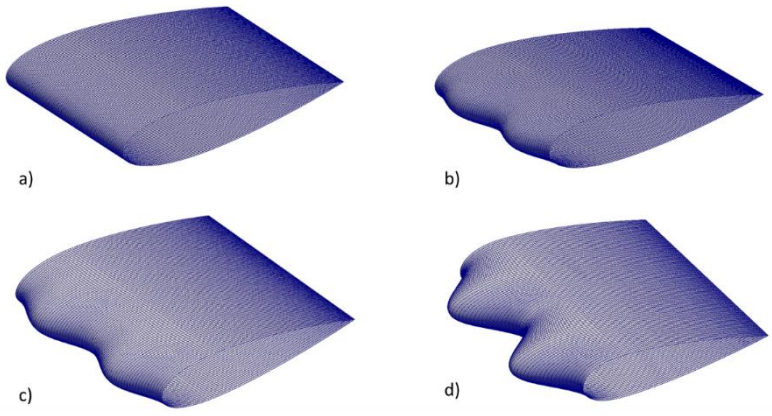

Figure 16: Hydrofoil models generated in 3-D (isometric view) standard leading-edge (a), amplitudes 2.5% of the chord length (b), 4% of the chord length (c), 10% of the chord length (d)

3.3 Boundary Conditions

The mesh in figure 14 has 7 patches, the locations and names of which are described in the figure with the exception of patches *Front* and *Back* which are located at either end of the span of the hydrofoil out of the page and into the page respectively. The 2-D simulation was run in 3-D by elongating the hydrofoil along the span (z-axis) and changing the empty boundary condition to symmetry, creating a hydrofoil with an infinite span.

Table 4: Patches and boundary conditions

Patches	**Boundary Condition**
Inlet	Freestream
Outlet	Freestream
Hydrofoil	Wall (no slip)
Front	Empty (2-D), Symmetry (3-D)
Back	Empty (2-D), Symmetry (3-D)
Upperwall	Freestream
Lowerwall	Freestream

As can be seen from table 4 there are 4 different boundary conditions used in the simulations. The *Freestream* boundary condition provides a mixed flow derived from the inlet/outlet condition. The mode of operation changes between a fixed value (free stream) and zero gradient based on the sign of the flux. This boundary condition is commonly used in CFD for simulations of external flow. The *Empty* boundary condition provides no flow in or out of the planes without imparting any forces onto the flow the way a solid surface would. The *Symmetry* boundary condition assumes that the two sides of the boundary have the same physical processes, variable magnitudes and gradients. Effectively, it acts as a mirror and is used in this study to simulate hydrofoils with an infinite span. The *Wall* boundary condition creates a solid surface at the patch which no fluid may pass through and a no slip condition at the closest layer to the patch. The hydrofoil remained fixed at the orientation in figure 12 for different angles of attack. The direction of the velocity at the inlet was altered for

different angles of attack. The initial values of the variables at different patches is given below in table 5.

Table 5: Values of the initial boundary conditions for RANS Spalart-Allmaras simulation of Re=120,000

Patch	**Pressure**	**Velocity (in direction of the flow)**	**Kinematic Turbulent Viscosity**	**Spalart-Allmaras Variable**
Inlet	0 gradient	1	0	3/Re
Outlet	0 gradient	1	0	3/Re
Hydrofoil	0 gradient	0	0	0
Upperwall	0 gradient	1	0	3/Re
Lowerwall	0 gradient	1	0	3/Re

3.4 Parameters

3.4.1 Non-Dimensional Simulation

To avoid medium specific results and for simplicity the length of the hydrofoil and the variables in the surrounding boundary field were intentionally set to unity, hence:

- $U_\infty = 1\ m/s$
- $c = 1\ m$

To simulate at different Reynolds numbers, the velocity and chord length remained constant at 1 and the kinematic viscosity was altered to create the desired flow field. The relationship between the Reynolds number and the kinematic viscosity was represented by equation 39, given the unity simulation parameters.

$$\nu = \frac{1}{Re} \qquad \text{Eq.39}$$

3.4.2 Simulation Reynolds Numbers

The Reynolds numbers used in the simulation were based on previous experiments [8], the dimensions of a humpback whale's pectoral flipper (c=0.704), humpback whale movement speeds and the kinematic viscosity of ocean water at standard temperature and pressure ($\nu=1.83\text{x}10^{-6}$ m^2/s). The Reynolds numbers used are given in table 6.

Table 6: Flow characteristics of the test cases

	Velocity *(m/s in the direction of the flow)*	Reynolds Number	Mach Number
Low Velocity	0.31	120,000 (*laminar-transitional*)	0.0002 (*incompressible*)
Feeding Velocity	2.6	1,000,000 (*fully turbulent*)	0.00173 (*incompressible*)
Maximum Velocity	7.2	2,770,000 (*fully turbulent*)	0.00480 (*incompressible*)

Using equation 39 and the Reynolds numbers in table 6, the kinematic viscosities for use in the CFD simulations were calculated and are included in table 8.

3.4.3 Incompressibility of the Flow

To ensure that assuming incompressible flow (ρ=constant) would not impact the results of the simulation, the Mach number was calculated for the flow conditions. A Mach number lower than 0.3 indicates that the flow can be considered incompressible [22]. This can be seen in table 6 based on the speed of sound in sea water at STP which is $c_{(water)}$=1500m/s. As all Mach numbers are far below 0.3, the flow was assumed to be incompressible.

3.4.4 Turbulence Models and Numerical Methods

The following considerations were used for selecting a turbulence model:

- For the current study, the area of interest is in the time averaged properties of the flow. The flow at the inlet is uniform and the hydrofoil remained stationary for all simulations.
- As the flow is turbulent in the wake region of the flow after separation, the turbulence needs to be modelled.
- The Spalart-Allmaras equations were developed for computer models involving hydrofoils and airfoils. The model was tested with computational experiments and the results compared with previous studies (see Section 4.1), showing good results

Given these parameters, the appropriate model appears to be RANS using the Spalart-Allmaras turbulence model as was used in a similar CFD study in Cai et al. (2015) [27]. It is worth noting that the same model was used for both low and high Reynolds number flow. In addition, the values of ν_t and $\tilde{\nu}$ were set to a value of 3/Re, as indicated in table 5 as the Spalart-Allmaras variable, which corresponds to a low turbulence intensity.

The discretisation practice used was a standard Gaussian finite volume integration. Gaussian integration is based on summing the values on the cell faces, which must be interpolated from the centre of the cells. A linear interpolation scheme was used for predicting values between the cell centres to cell face centres. The interpolation is based on the flux of the flow velocity. The solver used for the pressure was a generalised geometric-algebraic multi-grid solver whereas the solver used for the velocity and Spalart-Allmaras variable was a linear solver using a smoother. The matrix solver used was iterative i.e. based on reducing the equation residual over a succession of solutions. The residual is a measure of the error between iterations, so

the lower the residual, the lower the error. The simulation was considered converged once the residual for each variable had at least reached 0.0001.

3.5 Simulation Execution

In order to ascertain that the simulations were giving accurate results the first simulation was a recreation of the wind tunnel experiment performed in [17], using the same flow conditions and leading-edge profiles as indicated in table 7. A flow with this Reynolds number over a hydrofoil suggests laminar flow at the inlet and in the freestream. On validation of the data, the remaining hydrofoils were tested under the same parameters. The hydrofoils were all simulated in flow field with the inlet angle of attack (α) ranging from 0° to 26° increasing in increments of 2°.

Table 7: Validation test cases

	Reynolds Number	Leading-edge Amplitude	Leading-edge Wavelength
Straight leading-edge	120,000	0	0
Modified Leading-edge	120,000	5.71% of chord length	43% of chord length

Following the simulations at Re=120,000, every hydrofoil was tested again for attack angles ranging from 0° to 26°, having the Reynolds number coincide with the whales' lunge velocity which is Re=1,000,000. The results of these simulations where compared to those of the same leading-edge profile recorded at Re=120,000 to see if the tubercles were advantageous in fully developed turbulent flow. The hydrofoils were tested again in turbulent boundary conditions at a Reynolds number of 2,770,000. The reason for this was to test the efficiency at higher velocity and to observe any parasitic drag effects occurring resulting from the leading-edge tubercles or the difference in the lift generated between this and feeding speeds.

4.0 Results and Discussion

4.1 Verification and Validation for Re=120,000

4.1.1 2-D Hydrofoil

Before progressing to a three-dimensional mesh, the results from the 2-D simulations were analysed and compared to known physical properties to confirm that the boundary conditions, flow conditions, mesh and modelling were accurate. One method used for analysis was plotting the pressure coefficients over the hydrofoil at angles of attack of 0° and 6° and comparing it with results from Gregorek, et al. (1989) [28], which were presented in Wolfe and Ochs (1997) [29]. The values of the coefficient of pressure taken from the 2-D simulations have been plotted against the experimental data in figure 17. It was observed that the values generated through the OpenFOAM simulation were consistent with those found in the experiments performed by Gregorek et al. (1989) [28], along the surface of the hydrofoil.

The corresponding pressure and velocity magnitude fields to the plots in figure 17 are shown in figures 18 and 19. Both the pressure and velocity magnitude fields were symmetrical on the top and bottom of the hydrofoil in figure 18, indicating that the shape of the hydrofoil did not generate lift when the angle of attack was 0°. In the velocity magnitude fields in figures 18 and 19, the dark blue line around the hydrofoil, indicated that at the surface, the velocity of the flow was 0. Just adjacent, was the thin boundary layer surrounding the solid hydrofoil indicated by lighter blue.

In figure 18, the highest pressure on the hydrofoil was located at the stagnation point on the leading-edge tip. At the stagnation point, the velocity of the flow was 0 as the fluid impacted the hydrofoil at a location perpendicular to flow. This corresponded with the top plot seen in figure 17, at the highest value of the pressure coefficient. Additionally, the lowest recorded pressures were located near maximum hydrofoil thickness where the velocity was at 1.3 from an initial uniform inlet velocity of 1. For the 6° angle of attack, the pressure field in figure 19 showed an area of low pressure on the top surface close to the leading edge. The corresponding maximum velocity was at the same location as the minimum pressure and there appeared to be a small region

of slow-moving fluid close to the tip. The stagnation point also moved to below the hydrofoil as indicated in figure 19 by the location of highest pressure.

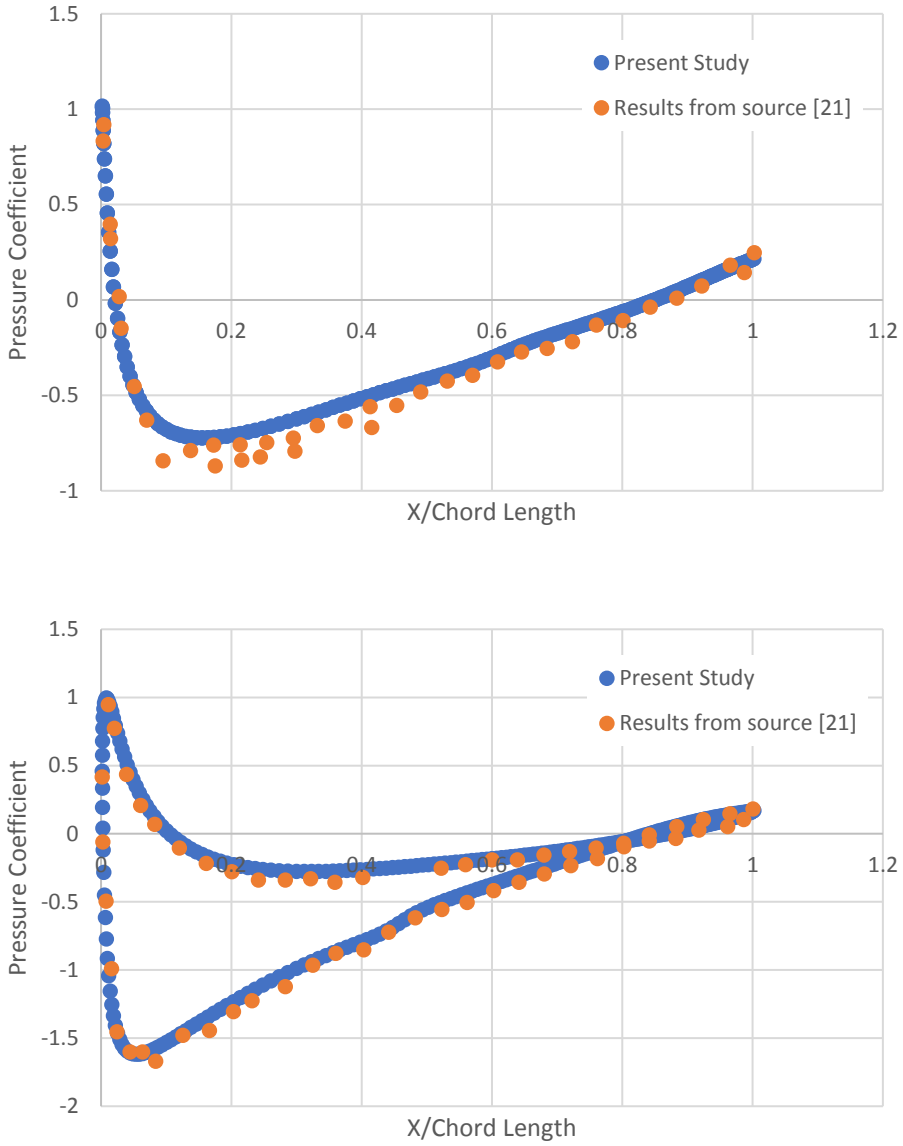

Figure 17: Coefficient of pressure profile for NACA0021 hydrofoil at Re=120,000 for 0° angle of attack (top) and 6° angle of attack (bottom)

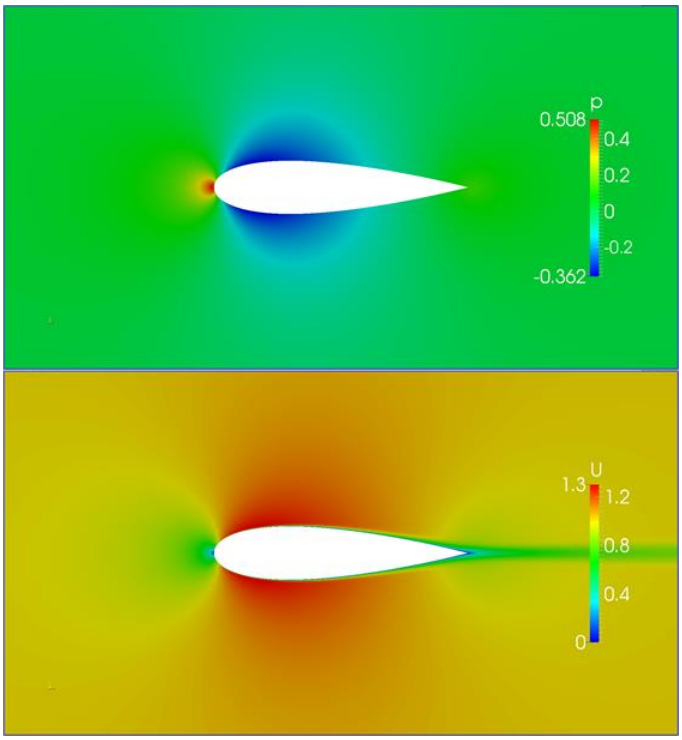

Figure 18: 2-D Hydrofoil at 0° angle of attack pressure field (top) and velocity magnitude field (bottom) at Re=120,000

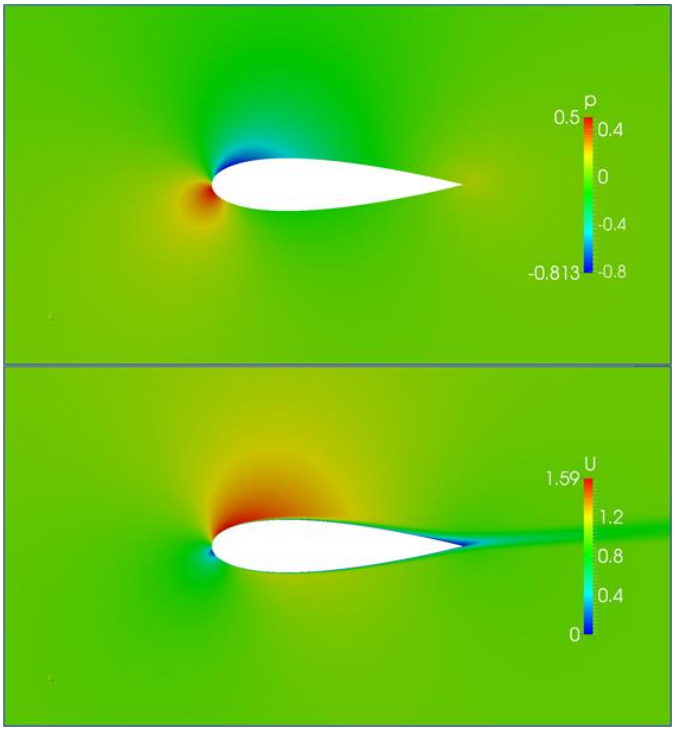

Figure 19: 2-D Hydrofoil at 6° angle of attack pressure field (top) and velocity magnitude field (bottom) at Re=120,000

The results from the 2-D model accurately predicted the values taken from [29] hence the mesh and boundary conditions were expanded into 3-D and used to generate reliable models of the hydrofoil with modified leading-edges.

4.1.2 3-D Standard Hydrofoil

The first 3-D simulations were run on the NACA 0021 hydrofoil with no modification to the leading-edge. The purpose of this was to generate a baseline model with which to compare the values recorded from the modified leading-edge simulations as well as the results from the 2-D simulation. Values from the physical experimental results of the standard NACA 0021 airfoil straight leading-edge from Rostamzadeh et al. (2013) [17] have been compared to the results produced by OpenFOAM.

From initial observations, the lift coefficient (C_l) and drag coefficient (C_d) results of the 3-D hydrofoil simulation in figure 20 showed moderate agreement with the results from [17] and with the results from the 2-D simulation, although there was a 30% difference in the results values predicted in CFD post-stall in the C_l plot and a corresponding 24% difference in the C_d results. The discrepancies in the results between the two could be explained by the model in this study not capturing the separation bubble that is characteristic of the NACA 0021 hydrofoil at a Reynolds number of 120,000. According to Rostamzadeh et al. (2014) [11] not modelling the separation bubble phenomenon increases the lift curve slope beyond the maximum value. However, according to Crivellini et al (2014) [30], the RANS CFD method in conjunction with a standard Spalart-Allmaras turbulence model with a low turbulent kinematic viscosity, can capture the behaviour of the separation bubble adequately. This is because, with a fine enough resolution, the model solutions remain laminar up to the separation point. Downstream, flow separation and the production of vorticity activates the Spalart-Allmaras production term which models the turbulent transition [30]. This behaviour captures the separation bubble behaviour almost exactly which is why it was not modelled separately for this study. The separation bubble is discussed further in Section 4.1.3. The CFD results for the 3-D simulation predicted less drag and lift pre-stall than in [17], and higher values of lift post stall. Stall occurred when

the flow closest to the surface broke away due to an adverse pressure gradient resulting in a rapid increase in drag and decrease in lift.

On the coefficient of lift graph before 5°, all the lift coefficients generated in CFD and determined experimentally were the same. The results from [17] became higher from that point until the stall angle of 12°. At 12°, the hydrofoil in the 3-D simulation also stalled whereas the lift coefficient of the hydrofoil in the 2-D simulation continued to rise and stalled at approximately 14°. Post-stall the results from [17] were lower than the results from the 3-D simulation and much higher than those generated in the 2-D simulations (from about 15° onward).

At angles of attack higher than 16° the values of lift from [17] and those generated in the 3-D simulation were very close. By contrast, in the drag coefficient graph, the three cases compared had differing values pre-stall with the 2-D simulation results giving the highest drag and 3-D simulation results giving the lowest drag.

The maximum percentage difference between the simulation values of the drag coefficient plot was 24%, at 14°. Post-stall, the 2-D and 3-D simulations showed identical results but, the values from [17] were higher than either of the simulations. The gradients of the lines in pre-stall, post stall and during stall remained consistent between the simulations and the experiment from [17]. All results have been retained in this study, even if they do not show good agreement with data from experimental or other numerical studies. They have been kept and included in the study as evidence of the limitations of the model at the higher angles of attack (>22°).

One possible explanation for the higher prediction of lift for the 2-D simulation compared with the 3-D model is that the 2-D results had empty boundary conditions on each side of the hydrofoil span which would reduce the amount of viscous forces present in the fluid as the results from the external source and 3-D model which had symmetry boundary conditions. Both the 3-D model and the external source experiment stalled at the same angle of attack, with almost the same value of C_l. This is further supported by the drag coefficient graph in figure 20 where the points begin

to separate slightly at the higher angles of attack pre-stall, and post-stall the difference between the values was much greater.

The results were close enough between the wind tunnel experiment in [17] and the simulations in this study to confirm that the values generated from the CFD model had strong qualitative agreement with good prediction of the stall angle.

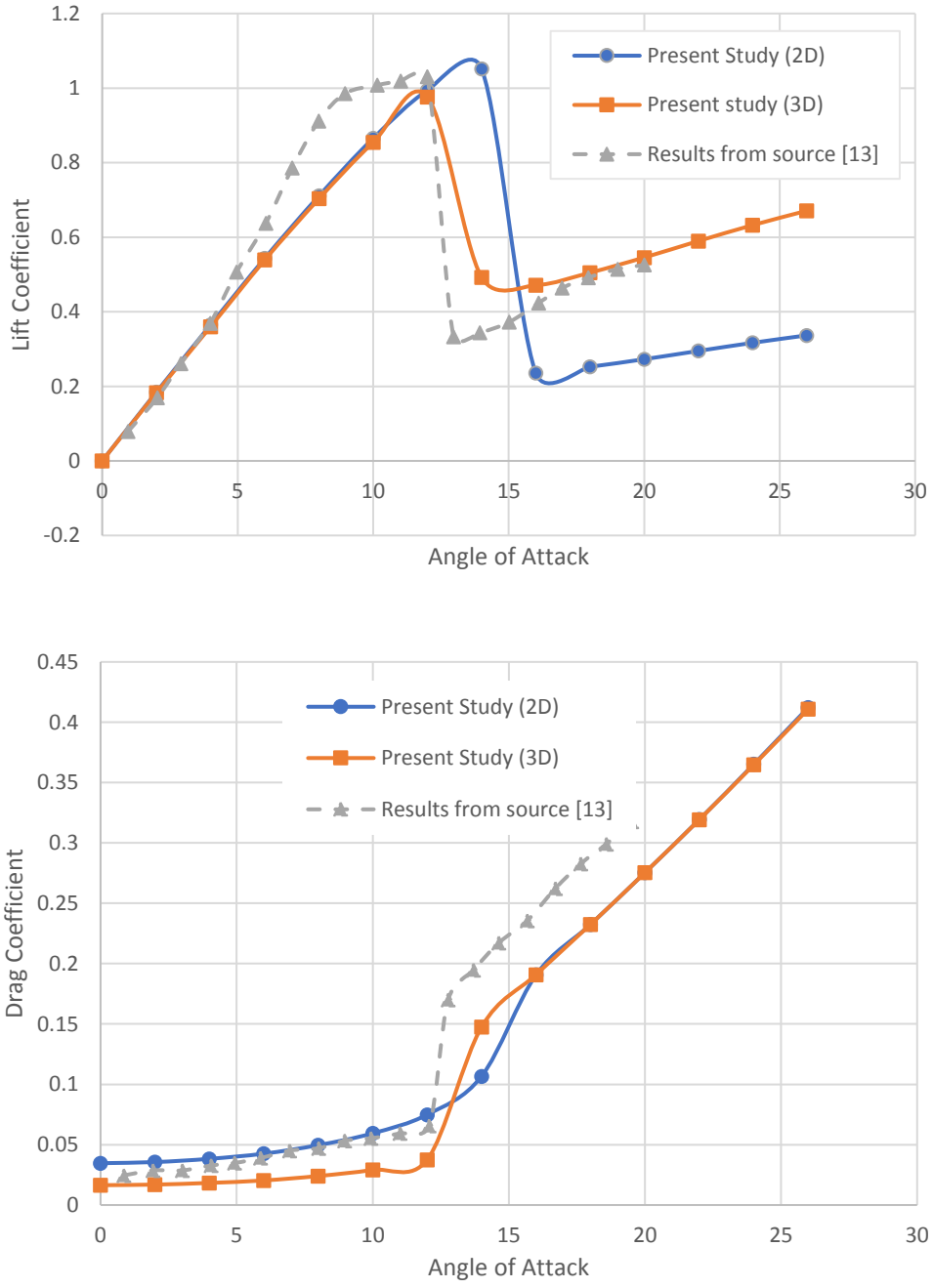

Figure 20: Lift coefficients vs. angle of attack of a standard hydrofoil (top) and drag coefficients vs. angle of attack of a standard hydrofoil (bottom) at Re=120,000

4.1.3 3-D Hydrofoil with Sinusoidal Leading-Edge of 5.71%

To further validate the CFD model, the first leading-edge tested was modelled on the amplitude and frequency of the leading-edge in [17] labelled as A8λ30. As a result, the leading-edge tubercles had an amplitude of approximately 5.71% of the mean chord length measured from mean amplitude to peak for 2 periods of the sinusoidal leading-edge (see figures 15 and 16).

The results from the lift coefficient plot in figure 21 showed values with good general qualitative agreement as the values recorded in [17]. The C_l values remained the same until 6° when the results from source [17] became slightly higher than the CFD predictions. The stall angle predicted in this study, was in agreement with the angle recorded in [17]. Post-stall, the CFD predictions changed from under- to over-predicting the value of lift at 16°. The percentage differences in the values were never greater than 14% and were therefore within the acceptable margin of error [31].

The coefficients of drag from the present study in figure 21 had a maximum percentage difference of 12% when compared with the results taken from the wind tunnel in [17]. The maximum difference in results was close enough to show that the simulations were accurately predicting the values of C_d. Note that for this case, the simulation of the hydrofoil with an attack angle of 12° encountered an unknown internal error which resulted in failure to converge. The simulation was excluded from the study.

The results of the pressure and friction coefficients from the CFD simulations were compared with results from Rostamzadeh et al. (2014) [11], as the same hydrofoil was used in their experiments, and the results plotted in figures 22 and 23. Figure 22 shows the data for pressure coefficients on the hydrofoils for an attack angle of 0° (top) and 8° (bottom) in the streamwise direction starting at the tubercle peaks, whereas, figure 23 shows the friction coefficients only for an attack angle of 8° in the streamwise direction starting at the tubercle troughs. Examining the data in figure 22 (top), the results from the hydrofoils appear to be almost identical along the leading-edge with a slight deviation towards the trailing-edge. Comparing the results from the hydrofoil troughs indicate that the pressure coefficient generated in the simulation is too high.

This could be caused by 3-D complex flow in this area which is difficult to resolve using RANS. In figure 22 (bottom), there is a larger difference between the results from [11] and those from the model. The peak results for each study are overlaid for most points along the hydrofoils, there appear to be outlying results at the leading-edge. The results from the troughs are quite close with a maximum percentage difference of 8%.

According to Rostamzadeh et al. (2014) [11], the relatively low chordwise pressure gradient is an indication of the presence of a laminar separation bubble on the suction side of the trough. The pressure coefficient distribution graph suggests that the flow on the unmodified hydrofoil undergoes separation and re-attachment, manifesting as the appearance of a laminar separation bubble (LSB). A bursting of the LSB leads to a sudden loss of lift. As the attack angle increases, the bubble moves towards the leading edge. With the corresponding rise in the adverse pressure gradient the re-attachment point disappears, and stall is occurring near the leading-edge [11]. By contrast, the hydrofoil with leading-edge tubercles undergoes a more gradual loss of lift indicating the absence of an LSB.

The friction coefficient results from [11] started at one of the leading-edge troughs and continued downstream along the surface of the hydrofoil. The results are displayed in figure 23, along with the results from the same hydrofoil used in this study. Despite having a few high varying values, the data collected from the simulations matches almost exactly the results from the external source. There are some slightly higher datum points at 0.3 and 0.45 of the chord lengths, with errors of approximately 20%. However, as they are only two outlying points, the rest of the data is considered reliable.

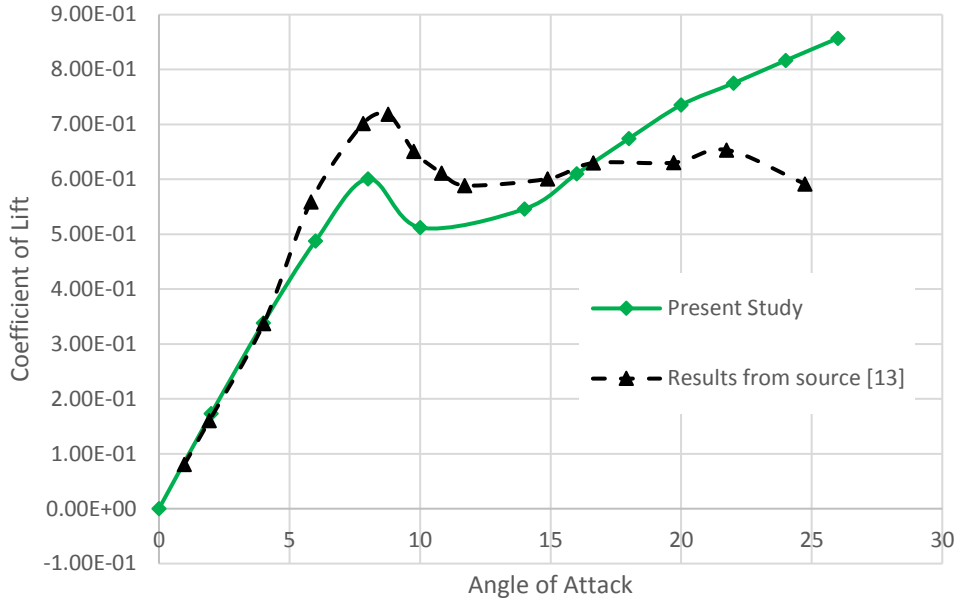

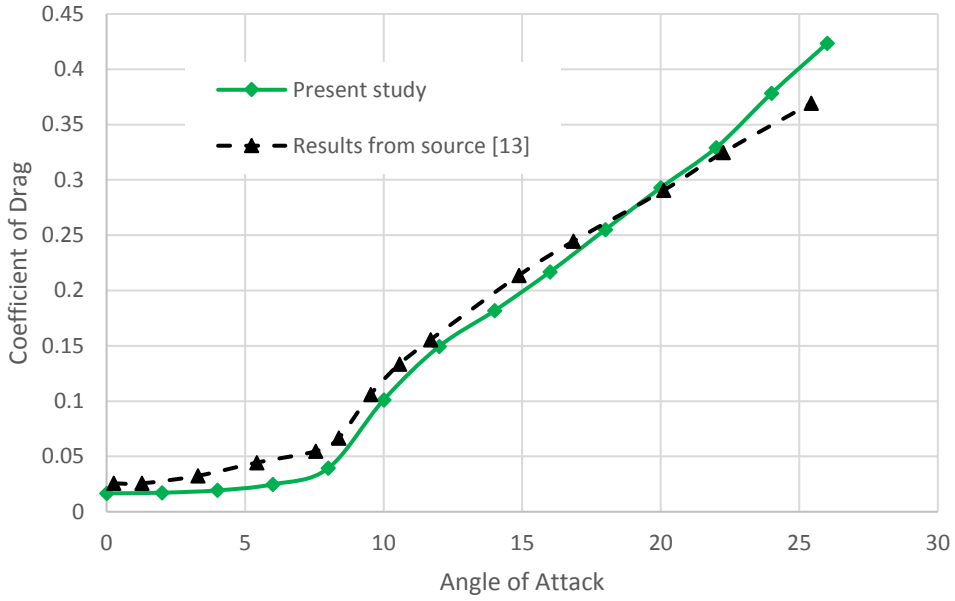

Figure 21: Lift coefficients vs. angle of attack of a hydrofoil with a 5.71% sinusoidal leading-edge (top) and drag coefficients vs. angle of attack of a hydrofoil with a 5.71% sinusoidal leading-edge (bottom) at Re=120,000

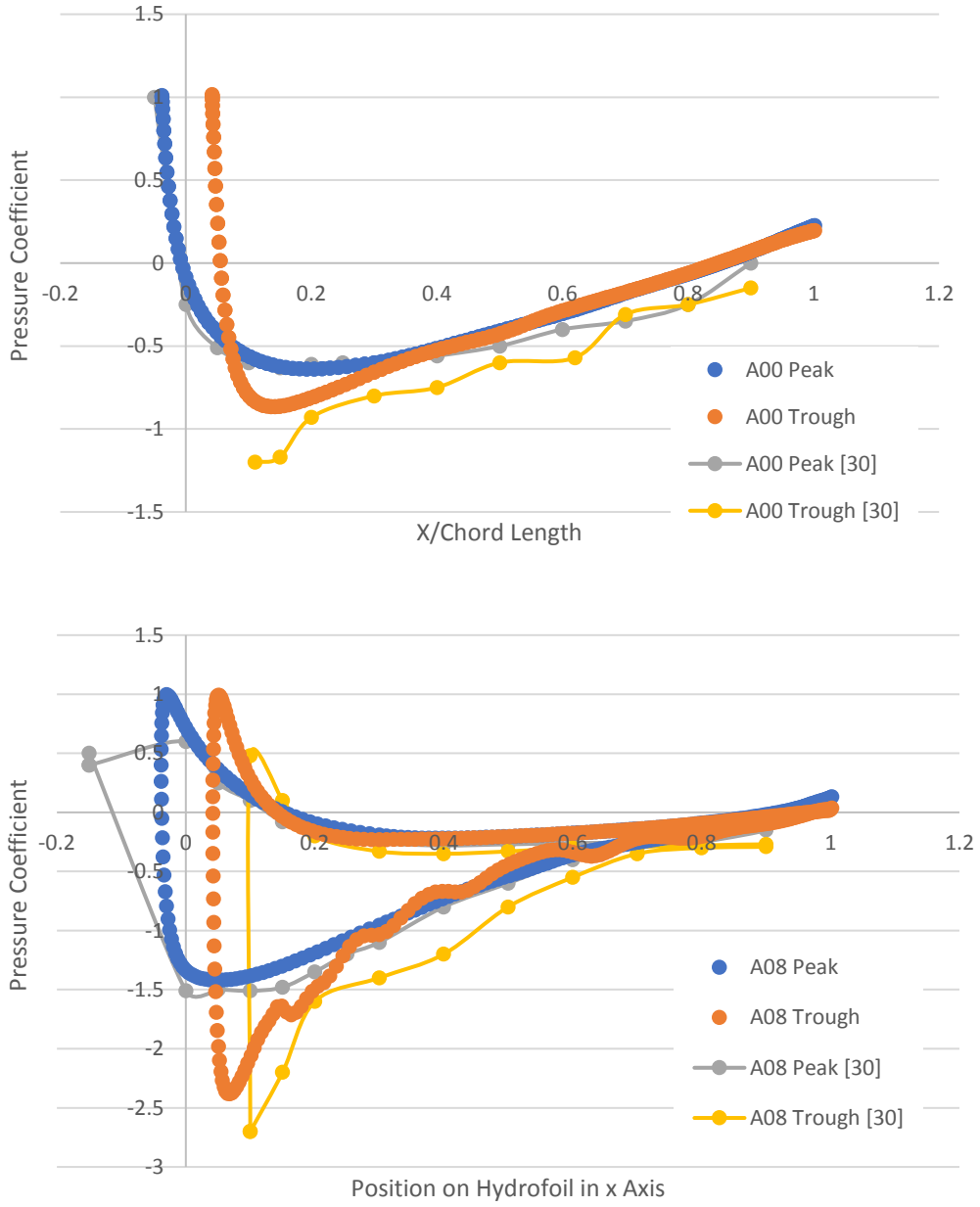

Figure 22: Pressure coefficients along the hydrofoil in study and [11] for (top) 0° attack angle and (bottom) 8° attack angle at Re=120,000.

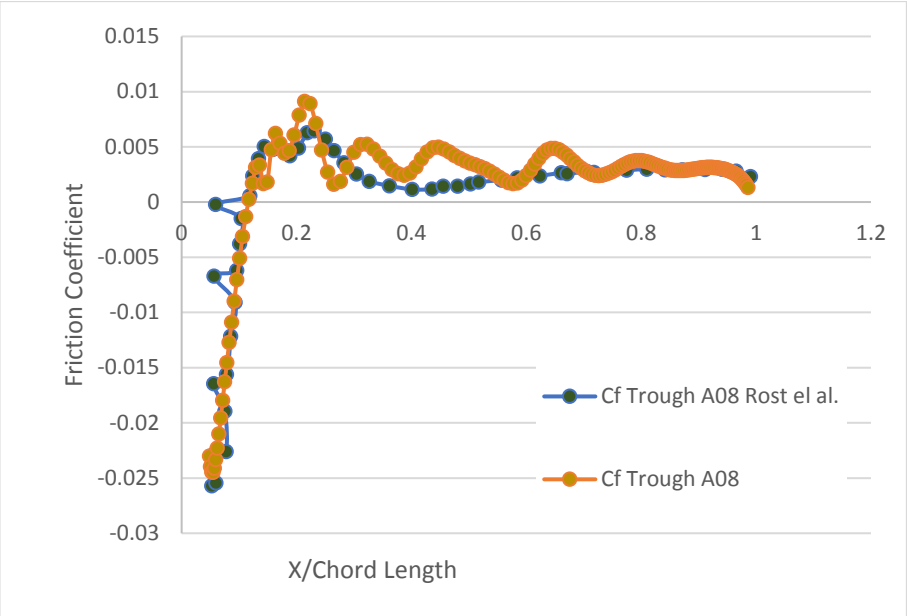

Figure 23: Friction coefficient comparison between study and [11] at attack angle of 8° in the tubercle trough in the x-axis at Re=120,000.

As the lift, drag, pressure and friction coefficients had values consistently close with previous experiments, the model has been validated for hydrofoils with leading-edges for a Reynolds number of 120,000.

4.1.4 Mesh Independence Study

To verify that the results being generated in the simulations were independent of the grading of the mesh selected, a mesh independence study was performed for the 2-D and 3-D simulations of the hydrofoil with a uniform leading-edge. Angles of attack of 6° and 18° were used to verify for both pre- and post-stall simulations.

The square markers on the graph in figures 24 and 25 indicate the mesh cell count used. Figure 24 shows that mesh densities higher than those used in the 2-D simulations in this study gave the same results pre- and post-stall as those recorded at a cell count of 55,316. Therefore, the 2-D results produced in the simulations were independent of the mesh. Similarly, figure 25 showed that the value of the lift coefficient for both angles of attack tested had the same result for any mesh count higher than 4,425,280.

Since the lift coefficients did not change between the final two meshes used, it was concluded that the mesh counts of 55,316 and 4,425,280 for 2-D and 3-D simulations respectively, were adequate to use for the CFD analysis of the hydrofoils with confidence that the mesh would not interfere with the accuracy of the results.

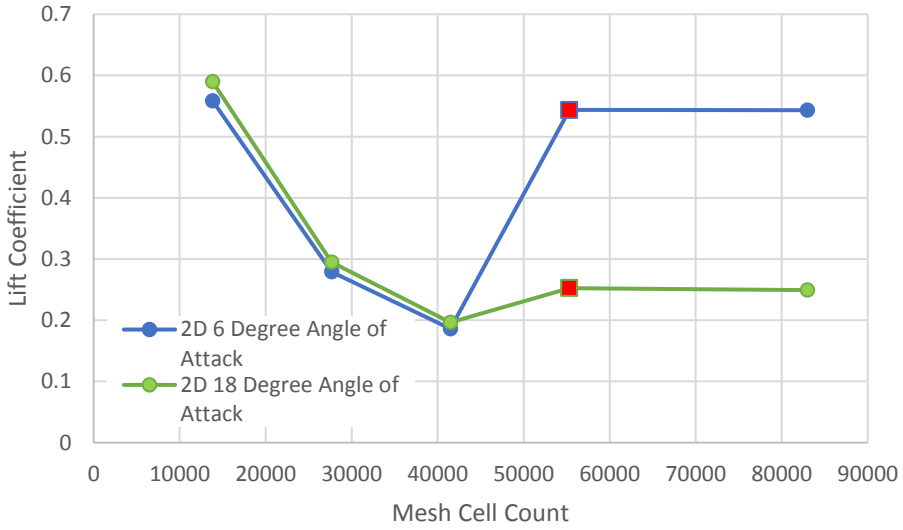

Figure 24: Lift coefficient vs mesh cell count for mesh independence study in 2-D

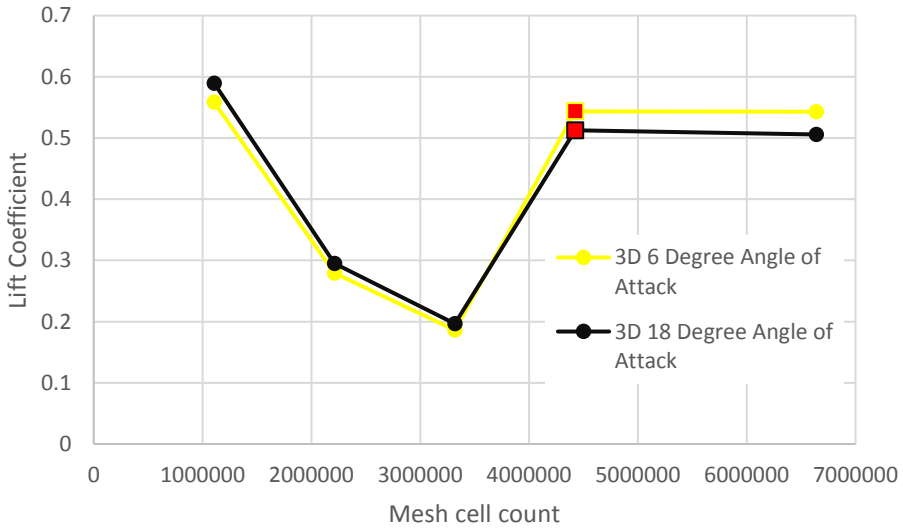

Figure 25: Lift coefficient vs mesh cell count for mesh independence study in 3-D

4.2 Effect of Leading-Edge Tubercles for Re=120,000

4.2.1 Effect of Sinusoidal Leading Edge

After using the values of the lift and drag coefficients to verify the simulation accuracy in Section 4.1, the wall shear stress, pressure and velocity magnitude fields were further examined to determine flow behaviour at different angles of attack. It should be noted that all wall shear stress, pressure and velocity magnitude figures are non-dimensional.

The wall shear stress on the top of the hydrofoil, as well as corresponding pressure fields, are shown in figures 26 and 27, in addition to a side view of the velocity field in figures 28 and 29 With an unmodified leading-edge, the fluid flowed uniformly over the surface. The friction lines of the flow in figure 26 for angles of attack of 0°, 8°, 16° and 24°, remained parallel as the flow transitioned from laminar to turbulent over the top surface of the hydrofoil, along the x-axis, for both post- and pre-stall angles of attack.

Comparing the wall shear stress along the top of the standard hydrofoil to the hydrofoil with a sinusoidal leading-edge of 4% amplitude in figure 26 for the angles of attack of 0°, 8°, 16° and 24° respectively, it can be seen how the tubercles impacted the flow close to the surface of the hydrofoil. At 0° angle of attack the scalloped hydrofoil appeared to have similar friction line patterns as the unmodified leading-edge which was also reflected in the pressure fields in figure 27 (a and e). The pressure was almost uniform at the leading-edge for the modified hydrofoil and in the velocity magnitude fields in figures 28 and 29 since the flow was symmetrical over the top and bottom surfaces.

The friction lines shown in figure 26 (f) were non-uniform for 8° angle of attack, which showed lines of stress moving around the tubercles, lines converging to a node in the trough, diverging line patterns from the node continuing downstream with counter-rotating spiral patterns emerging on either side, with two nodes downstream of each other, directly downstream of the peaks and mixing towards the trailing-edge. Whereas, post-stall, at an angle of attack of 16°, the wall shear stress pattern changed

drastically to indicate lines of stress converging downstream of the trough with a lower stress region indicated by the lighter blue shading in figure 26 (g). At 16°, there appeared to be an area of high wall shear stress closer to the tubercles, beginning at the peaks and curving into the troughs downstream of the leading edge.

From examination of figure 27 for the standard hydrofoil at the pre-stall angles of attack, the pressure was at its minimum value close to the leading-edge of the top surface of the hydrofoil where the fluid experienced maximum velocity. The surface pressure results showed that, as the angle of attack increased, there was a larger concentration of strong negative pressure coefficient values towards the leading-edge between the tubercles. As was seen in figure 27, almost the entire surface had a negative pressure coefficient, although the values were less than they had been whilst the flow as still attached pre-stall. In the absence of tubercles, the pressure field was uniform along the span.

Comparison of the modified hydrofoil with the standard hydrofoil in figure 27 showed that at the same angle of attack, the top surface of the modified hydrofoil experienced lower pressure, particularly between the tubercles. The low pressure became localised to the troughs pre-stall and continued post-stall as indicated in figure 27. This was an indication of faster moving fluid between the tubercles and showed that the flow was channelled even post stall.

The pressure field predicted by the CFD simulation became asymmetrical in figure 27 (h) at $\alpha=24°$ along the span of the hydrofoil, which should not occur given the infinite span of the hydrofoil and the uniform amplitude and frequency of the sinusoidal leading edge. This indicated that although the simulation had reached convergence, the result was not a realistic representation of a hydrofoil with an infinite span. It is possible that the complexity of the 3-D flow present in the turbulent region of the wake at high values of α was beyond the solving capability of RANS and a different CFD method would have been more appropriate. This would also explain why the lift coefficient in figure 21 for the angle of attack had such a difference compared to the result from source [17]. This was a limitation of the RANS model and the Spalart-

Allmaras turbulence model which had difficulty resolving the flow in the presence of a high adverse pressure gradient.

At 16° in figure 28 stall had occurred, and the flow was separated from the top surface almost completely as indicated by the large area of slow moving fluid just downstream of the leading-edge on the suction side of the hydrofoil. The wake behind the hydrofoil was much larger, as indicated by the light and dark blue area. At 24°, the wake region developed further and was larger than at 16°. Note that in this region the flow was not stagnant as it is in the blue region at the point of first contact of the hydrofoil, it was just moving in the x direction (downstream) much slower as a lot of the momentum of the fluid particles was mixing in the turbulent wake region and flowing along the z axis (along the span).

Examining the velocity magnitude field in figure 29 for the hydrofoil with a sinusoidal leading-edge, at $\alpha=0°$, the flow field is symmetrical over the hydrofoil and the maximum fluid velocity occurred near the hydrofoil maximum thickness on the top and bottom of the surface, downstream of the stagnation point at the leading-edge. For an angle of attack of 8° in figure 29 (b), there was a region at the top surface, closer to the leading-edge than figure 29 (a), where the velocity was at maximum and a small turbulent region close to the surface towards the trailing-edge, as indicated by the slow-moving fluid, showing the beginning of separation.

For the hydrofoil with leading-edge tubercles in figure 29, at the trough, the velocity field closely resembled that of the unmodified leading-edge although there appeared to be a larger wake region post-stall possibly due to the channelling effect of increased flow between the tubercles. By contrast, the wake region at the peak was much smaller than at the trough. At 8° the wake region was almost the same as at 0° at the peak. The fluid appeared to remain attached to the surface at the peak detaching about one third of the chord length from the leading-edge of the hydrofoil where the wake region began.

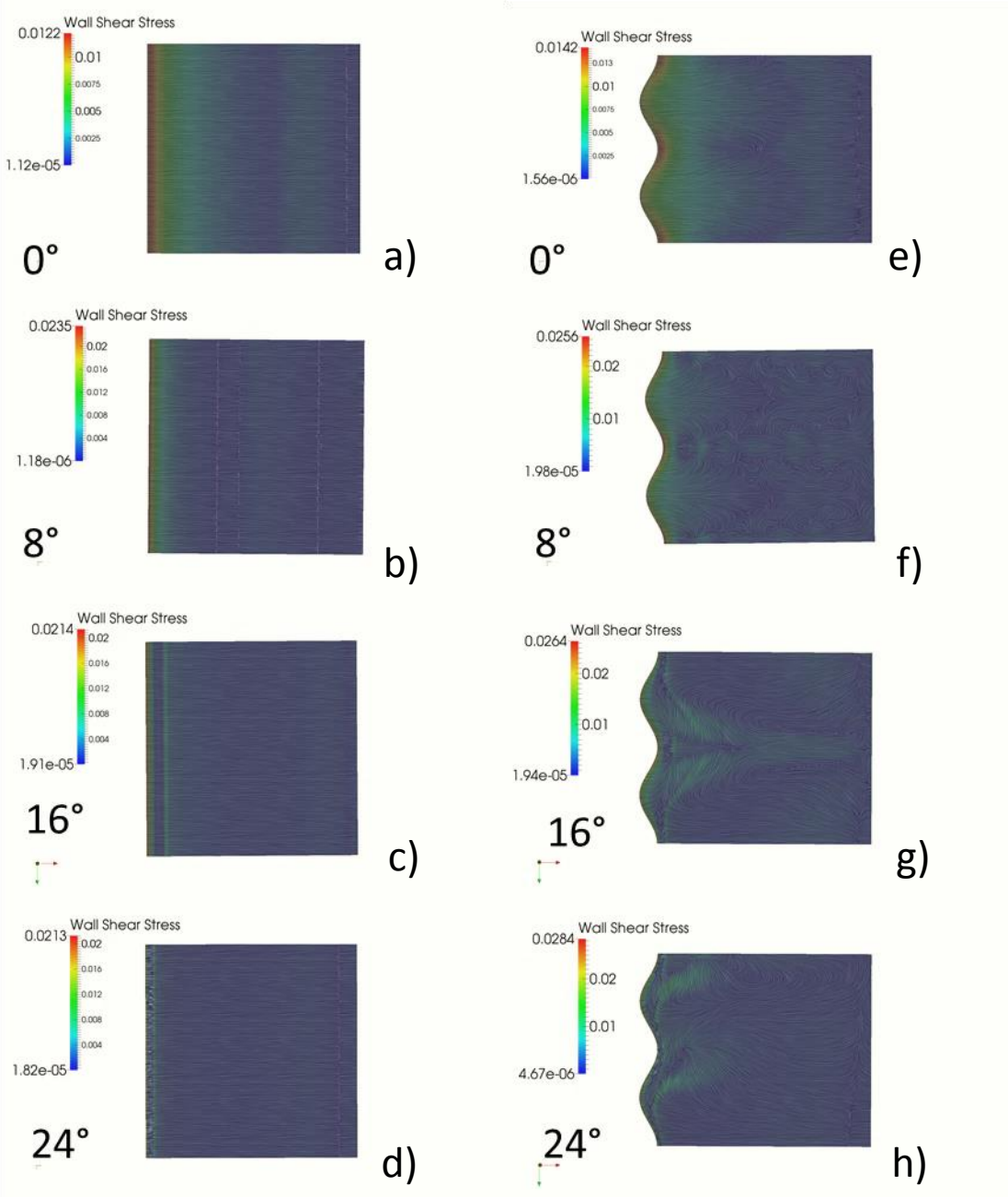

Figure 26: Wall shear stress magnitude field with friction lines on the top surface of a standard hydrofoil (left) and a hydrofoil with a sinusoidal leading-edge of 4% amplitude (right) at α=0°, α=8°, α=16°, α=24° at Re=120,000

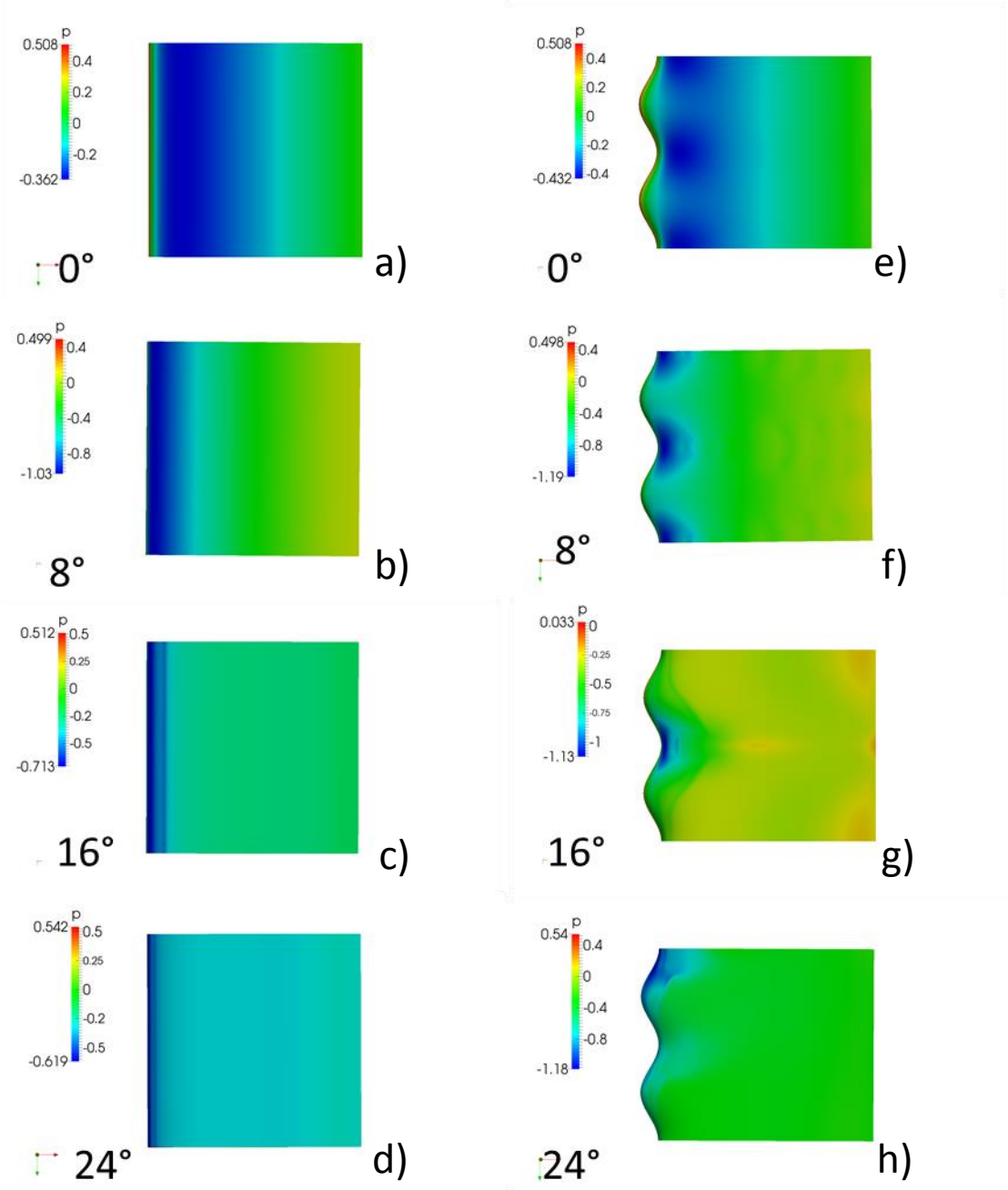

Figure 27: Pressure field on the top surface of a standard hydrofoil (left) and a hydrofoil with a sinusoidal leading-edge of 4% amplitude (right) at α=0°, α=8°, α=16°, α=24° at Re=120,000

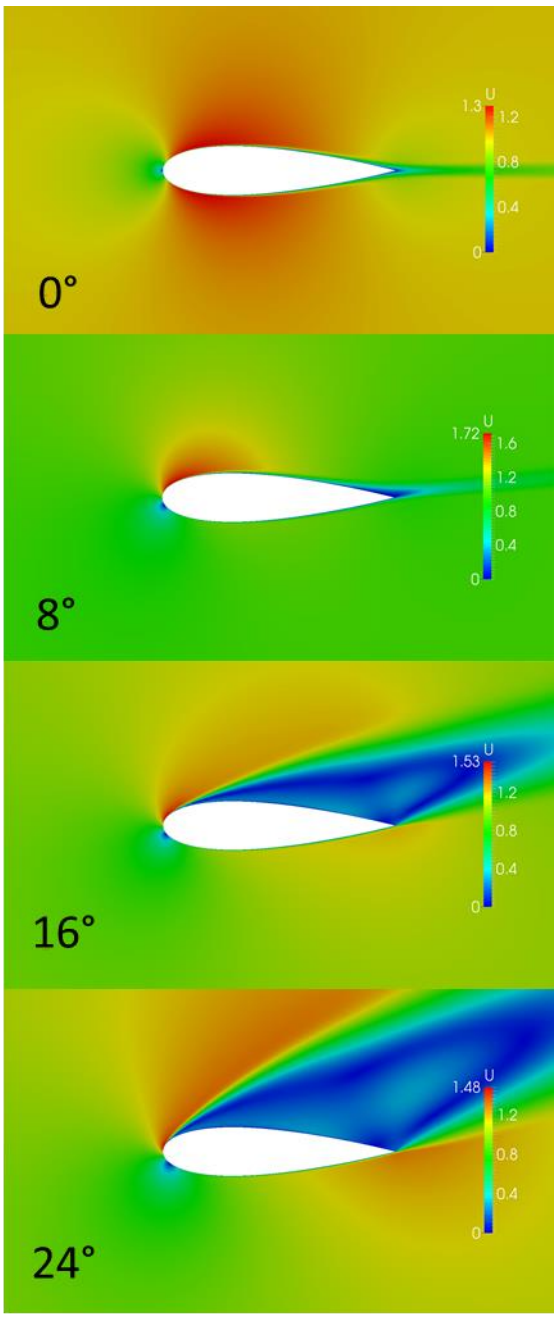

Figure 28: Velocity magnitude field of a standard hydrofoil at α =0°, α =8°, α =16°, α =24°. Slice taken at centre of span at Re=120,000.

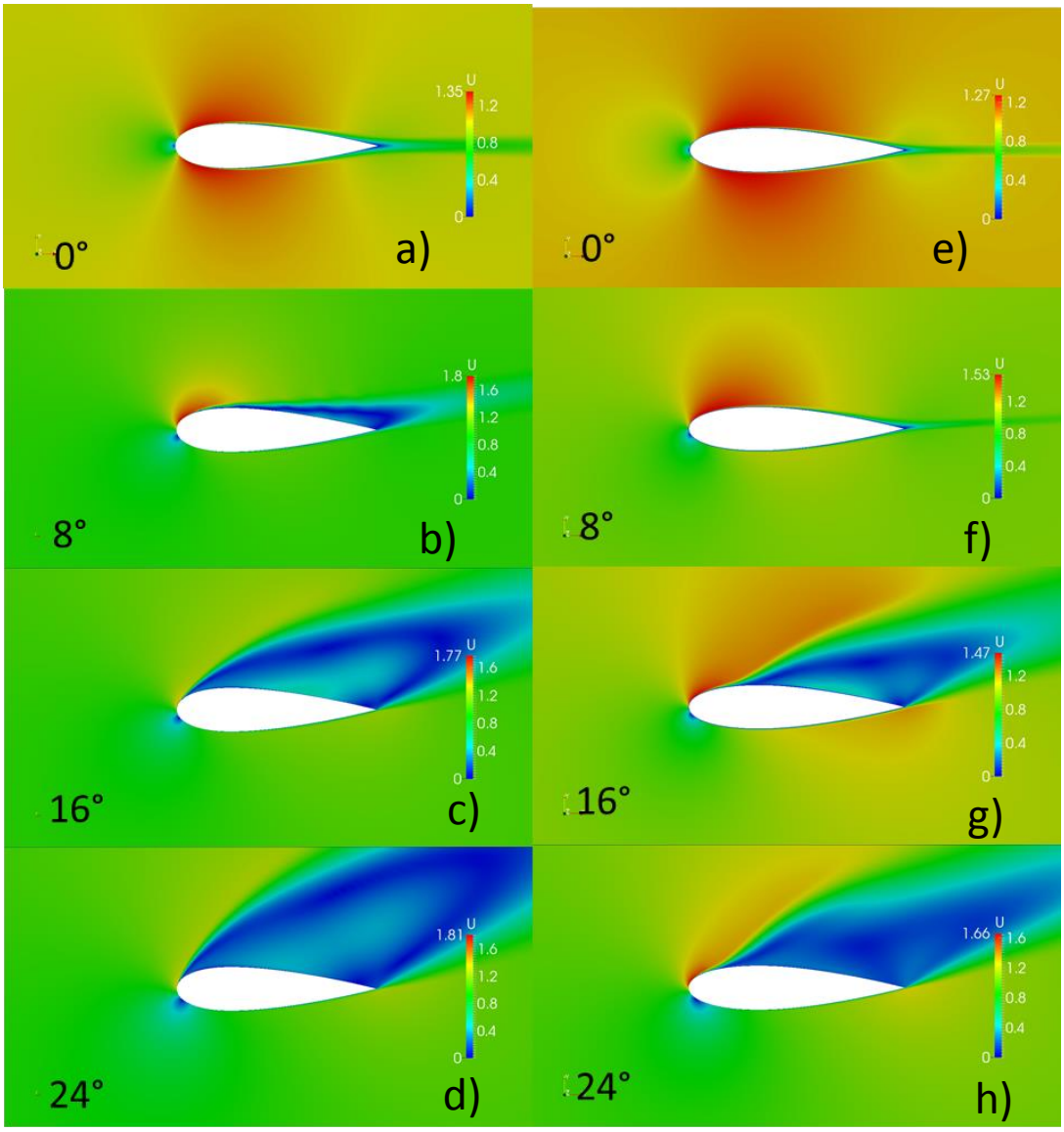

Figure 29: Velocity magnitude field of a hydrofoil with a sinusoidal leading-edge with a 4% amplitude, at the trough (left) and at the peak (right) at α =0°, α =8°, α =16°, α =24° at Re=120,000

4.2.2 Effect of Tubercles Amplitude

To test the theories about the method of passive flow control employed by the humpback whale, two simulations were run with a Reynolds number of 120,000 for hydrofoils with sinusoidal leading-edges of 2.5% and 10% of the chord length respectively. Modifying the leading-edge tubercle amplitude to 2.5% of the chord length was to test if the reduction in amplitude would yield results closer to that of the standard hydrofoil. The tubercles with an amplitude of 10% of the chord length were generated to test if the intensity of the counter-rotating vortices generated would increase around the tubercles and what effect that would have on the stall conditions. The lift and drag coefficients of all the hydrofoils tested under laminar flow conditions are presented in figure 30.

For angles of attack below 12°, the standard hydrofoil had the highest values of lift coefficients as per figure 30, reaching a maximum value of 0.99 at 12°. In this range (pre-stall), figure 30 indicates that the lift generated on the hydrofoil appears to be inversely related to the amplitude of the tubercles, as was the angle at which stall occurred. Stall occurred most rapidly on the hydrofoil with tubercles of amplitude 10% at 6°, reaching a C_l value of 0.5. The hydrofoil with 4% leading-edge tubercles stalled at 8°, reaching a value of 0.61 and the hydrofoil with tubercles of 2.5% of the chord length amplitude reached a maximum of 0.86 at 10° before stalling.

For angles of attack greater than 12°, the hydrofoils with leading-edge tubercles generate higher values of lift than a standard hydrofoil. For the hydrofoil with tubercle 10% of the chord length, the protuberances had a severe adverse effect on the lift coefficient of the hydrofoil in the pre-stall region, particularly as it encourages the foil to stall at only 6°. Post-stall however, the lift coefficient rose immediately after the drop at 8° almost linearly. For all scalloped hydrofoils, the drop in lift experienced at the critical angle appeared to be much lower in magnitude with the introduction of leading-edge tubercles and inversely proportional to the tubercle amplitude. Pre-stall, for a fluid flow with a Reynolds number of 120,000, the hyrdofoils with tubercles provided no benefit to hydrodynamic performance when compared to an unmodified hydrofoil.

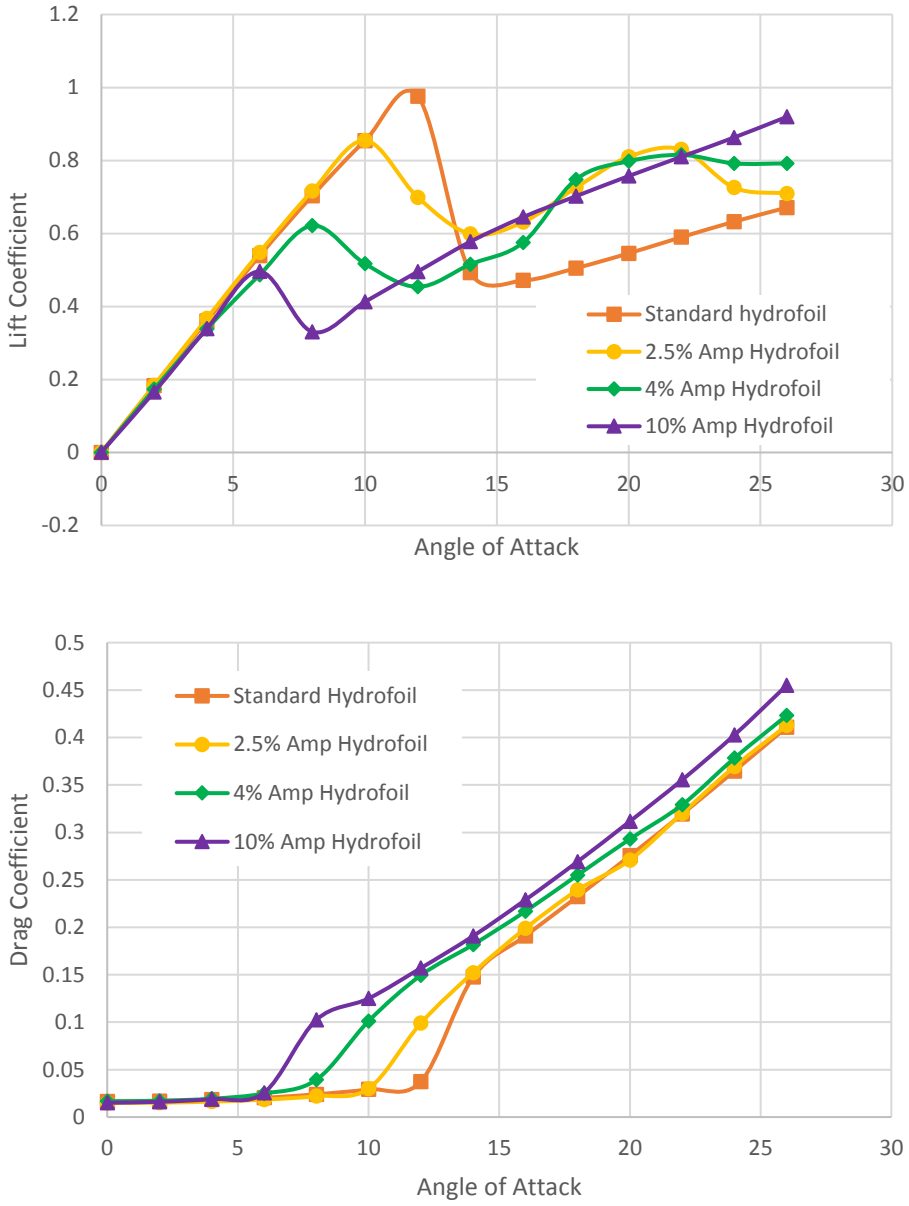

Figure 30: Lift coefficients (top) and drag coefficients (bottom) vs. angle of attack of hydrofoils with standard, 2.5, 4% and 10% amplitude sinusoidal leading-edges, for a Reynolds number of 120,000.

For all cases, the sudden drop in value of the lift coefficient plots in figure 30 following the maximum of the curves, indicated boundary layer separation at the leading-edge of the hydrofoils. With the presence of tubercles, boundary layer separation was not uniform along the span at the leading edge, hence stall could not be defined as the full separation of fluid at the leading edge. Instead, stall for hydrofoils with sinusoidal leading edges was redefined as the sudden loss of lift and increase in drag due to the

strong retarding forces of the flow in the boundary layer caused by flow separation at the tubercle troughs.

It was observed from the drag coefficients in figure 30 that the values of C_d for each hydrofoil up to 6° were the same. At stall, the value of C_d increased rapidly. The stall angle for each hydrofoil, as indicated by the sudden increase in drag, was different depending on the leading-edge and corresponded to the stall angle in the lift coefficient plot. Post-stall, the values of C_d rose almost linearly with close to the same gradient. It appeared that the earlier the stall, the higher the C_d in the post stall region when comparing the hydrofoils. The hydrofoil with the leading-edge tubercles of 2.5% of the chord length overlapped the unmodified hydrofoil results post stall despite stalling at 10° whereas the straight edged hydrofoil stalled at 12°. The presence of tubercles did not delay stall as each hydrofoil with a sinusoidal leading-edge stalled at an angle of attack lower than that of a standard hydrofoil. However, for the hydrofoils with tubercles in figure 30, there was not a sudden drop in the lift coefficient as there has been for other hydrofoils. The manner of stall was different between the modified and standard hydrofoils in the flow with a low Reynolds number, in that there was still a loss of lift beyond the critical angle, but full boundary layer separation was not present along the entire leading edge.

From figure 31, the 2.5% amplitude tubercle hydrofoil appeared to channel flow between the tubercles given the pattern in the friction lines on the hydrofoil surface, though not as significantly as the hydrofoil with the 10% amplitude. At α=16° a crescent pattern of high wall shear stress was formed downstream of the leading-edge tubercles which was vastly different from the 10% amplitude tubercle hydrofoil.

From the wall shear stress images in figure 31, the hydrofoil with 2.5% amplitude had friction lines which were parallel to the direction of the flow, whereas for the hydrofoil with 10% amplitude the friction lines were more significantly influenced by the tubercles, particularly in (f) (g) and (h). For the 10% amplitude hydrofoil, the flow pattern shows the stress lines converging downstream of the leading-edge trough pre- and post -stall, whereas in figure 31 (e), stress lines are almost in parallel rather than being forced into the centre of the span. When compared with the C_l and C_d plots in

figure 30, the tubercles did not appear to delay stall as was originally hypothesised, however the flow does appear to remain attached at the peaks of the tubercles, even post-stall.

If flow was channelled into the tubercle troughs, it was expected that there were negative pressure coefficients between the tubercles that continued downstream of the leading edge. The faster flow between the tubercles created low pressure regions in the troughs. This is consistent with the results from Rostamzadeh et al (2014) [11], which states that the trough region is susceptible to flow separation due to locally large adverse pressure gradients. This is further supported by the fluid velocity diagrams in figures 33 and 34 which show larger turbulent wakes in the troughs for both sets of tubercles commencing at the leading edge. by the plots of lift and drag in figure 30 for the 10% amplitude tubercle leading-edge hydrofoil.

The pressure had a non-uniform spread along the span showing that fluid was moving faster between the tubercles even at 0° angle of attack. Post-stall, what was observed were similar velocity profiles of different magnitudes depending on the amplitude of the leading-edge with a larger wake region at the trough and flow attachment at the tubercle peak for higher angles of attack. At 16° in figure 33, the wake region over the trough for 2.5% amplitude tubercles remained much smaller than the simulation with 10% amplitude tubercles. This could be a result of the more uniform pressure profile on the hydrofoil with the leading-edge tubercles of 2.5% amplitude. It did not appear to delay stall as indicated in figure 30 when compared to the standard hydrofoil plot. Examining the velocity fields, the results in figures 33 and 34 demonstrated a larger difference in the flow profile of the peak and trough at the larger tubercle amplitude. The development of the wake at the trough and the delay of the boundary layer separation of the peak was also shown. In figure 34 for the 10% amplitude hydrofoil, at 8°, there appears to be separation occurring further downstream from the peak leading-edge despite the hydrofoil stalling at 6° (figure 30). At 16° a wake region was indicated in the velocity magnitude field by the slow-moving fluid region in the trough area on the surface of the hydrofoil (figure 34).

There appears to be a slight skewness in the results in figures 31 and 32 (d and h). It is possible that at the higher angles of attack, the fluid flow in the wake region on the top

rear surface is too complex to be adequately resolved by a time averaged solver. This might explain why the pressure distribution and wall shear stress distribution are not uniform along the top surface of the hydrofoils. This was also observed in Section 4.2.1 at high angles of attack.

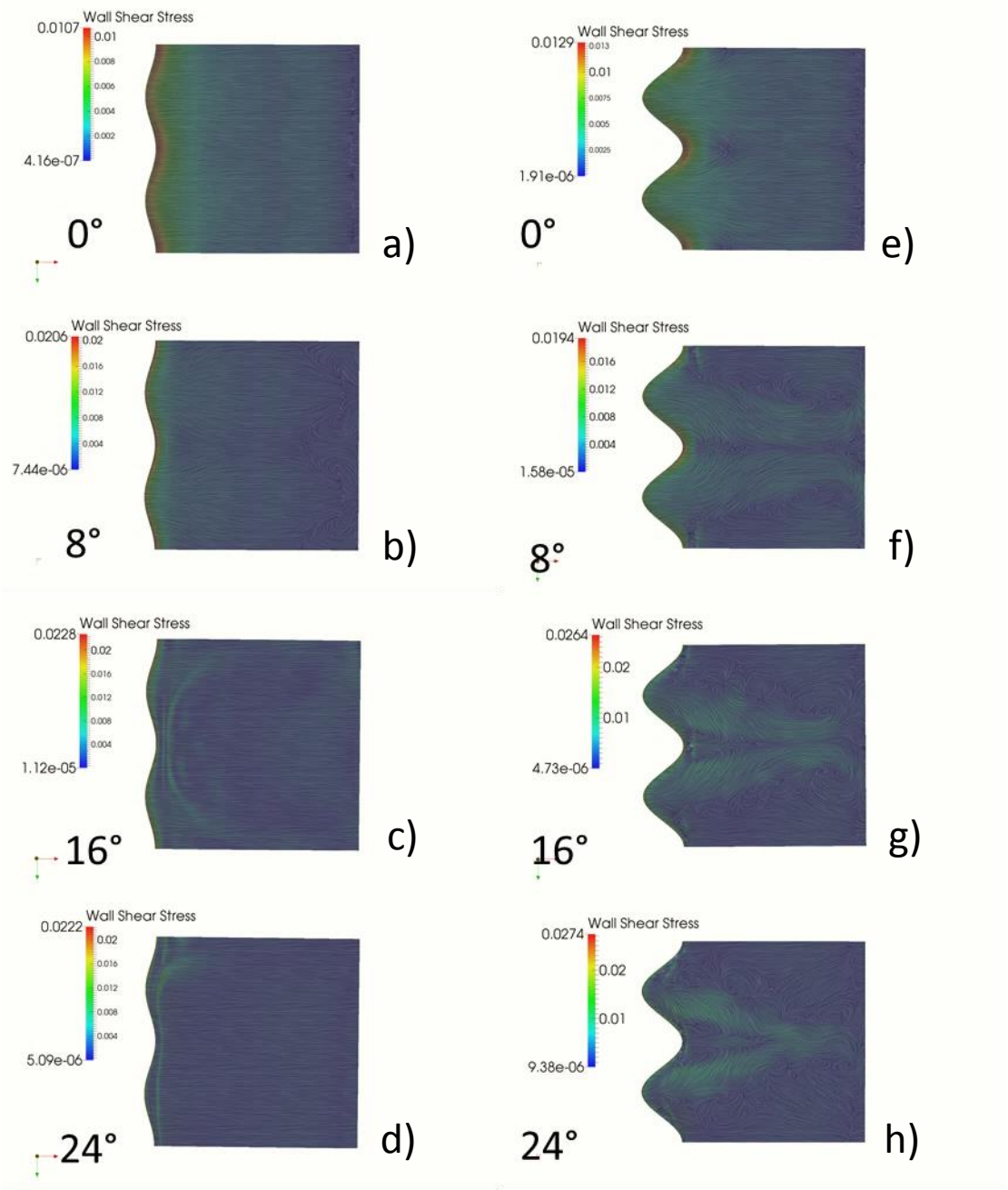

Figure 31: Wall shear stress magnitude field with friction lines on the top surface of a hydrofoil with a sinusoidal leading-edge of 2.5% amplitude (left) and 10% amplitude (right) at α=0°, α=8°, α=16°, α=24° at Re=120,000

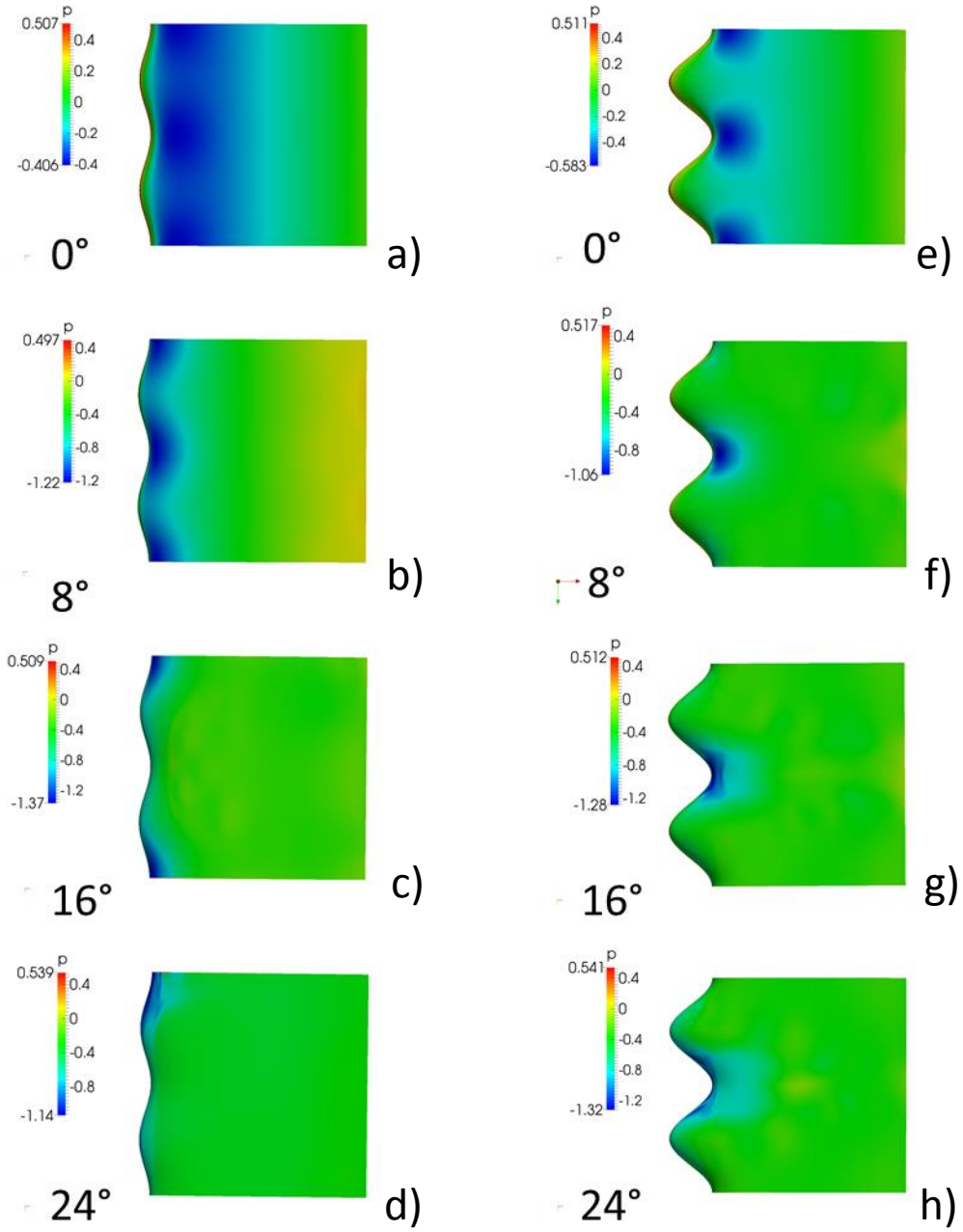

Figure 32: Pressure field on the top surface of a hydrofoil with a sinusoidal leading-edge of 2.5% amplitude (left) and 10% amplitude (right) at α=0°, α=8°, α=16°, α=24° at Re=120,000

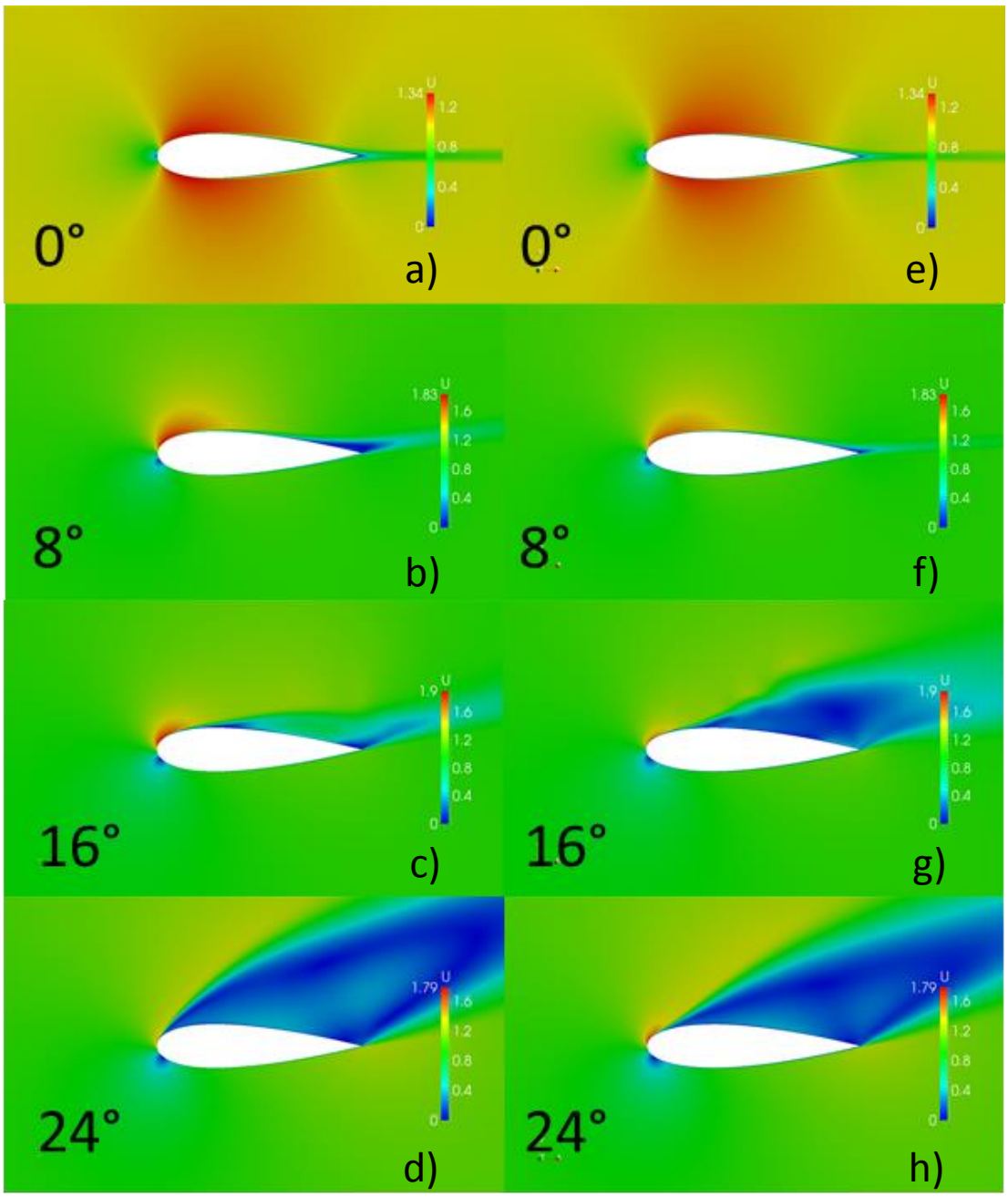

Figure 33: Velocity magnitude field of a hydrofoil with a sinusoidal leading-edge with a 2.5% amplitude, at the trough (left) and at the peak (right) at α=0°, α=8°, α=16°, α=24° at Re=120,000

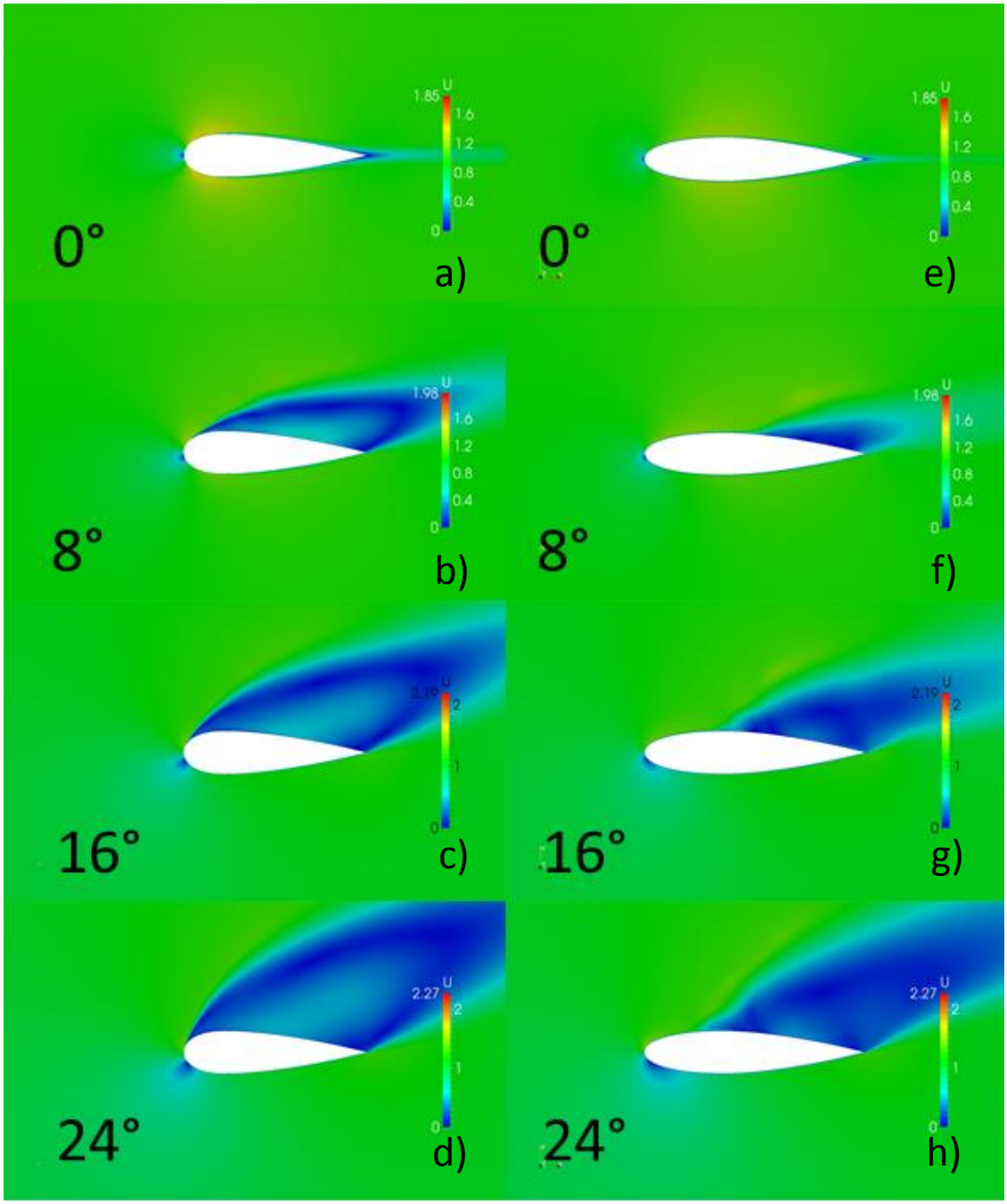

Figure 34: Velocity magnitude field of a hydrofoil with a sinusoidal leading-edge with a 10% amplitude, at the trough (left) and peak (right) at α=0°, α=8°, α=16°, α=24° at Re=120,000

4.3 Verification and Validation for Re=1,000,000

Using the same NACA 0021 profile, a set of simulations were executed with a Reynolds number of 1,000,000. The reason for this being that it has been theorised that the humpbacks tubercle pectoral flippers exist on this species of cetacean whale and no others because of the whales' unique bubble net feeding method. When a humpback lunges through a school of krill they travel at a velocity of (on average) 2.6m/s towards their target which means that the whale has an approximate Reynolds number of 1,000,000. At this value the flow will be fully turbulent as Re > 500,000 [17], [6]. To verify that the simulation was accurate for fully turbulent flow conditions, the CFD results were compared to the experimental results in [29].

Since flow behaviour was different in fully turbulent conditions, the standard hydrofoil simulation was run in 2-D first and then in 3-D and compared with experimental results from [29]. Similar to the verification for the standard hydrofoil with a Reynolds number of 120,000, the 2-D simulation predicted stall at a higher angle of attack than the 3-D simulation. The 3-D simulation predicted stall at the same angle of attack as the results presented in [29], which was 14°, but also predicted a higher lift coefficient of 1.3 at the critical angle. Both simulations in this study predicted higher lift coefficients in the post-stall results when compared with the work done in [28] and presented in [29]. The 2-D simulation predicted stall at 16° for a value of 1.38 remained higher than the 3-D simulation until 20° where the two simulations started predicting almost identical results. Post-stall, the results from [29] fluctuated as the angle of attack increased, whereas for the simulations, the results created a linear plot for the C_l graph. Examining the drag, the results from the 3-D simulation were the same as the results from [29]. The 2-D simulation appeared to over-predict the drag coefficient.

The results from the CFD simulations, in figure 35, were consistent with the experimental results from Gregorek, et al. (1989) [28] presented in Wolfe and Ochs (1997) [29] and therefore should accurately predict the averaged fluid behaviour for the modified leading-edges. In the lift coefficient plot, the externally sourced values were constantly lower than the CFD generated results in the post-stall region. The results from source [29] slowly declined in a similar way to the results generated in CFD. The maximum difference in lift values between the 3-D simulation and the wind

tunnel experiment was only 0.2 which is within the margin of error (<20%) in the turbulent complex flow fields. Hence, the results are sufficiently close to indicate that the CFD model appeared to reflect the wind tunnel results and hence further predictions generated in fully developed turbulent flow were reliable.

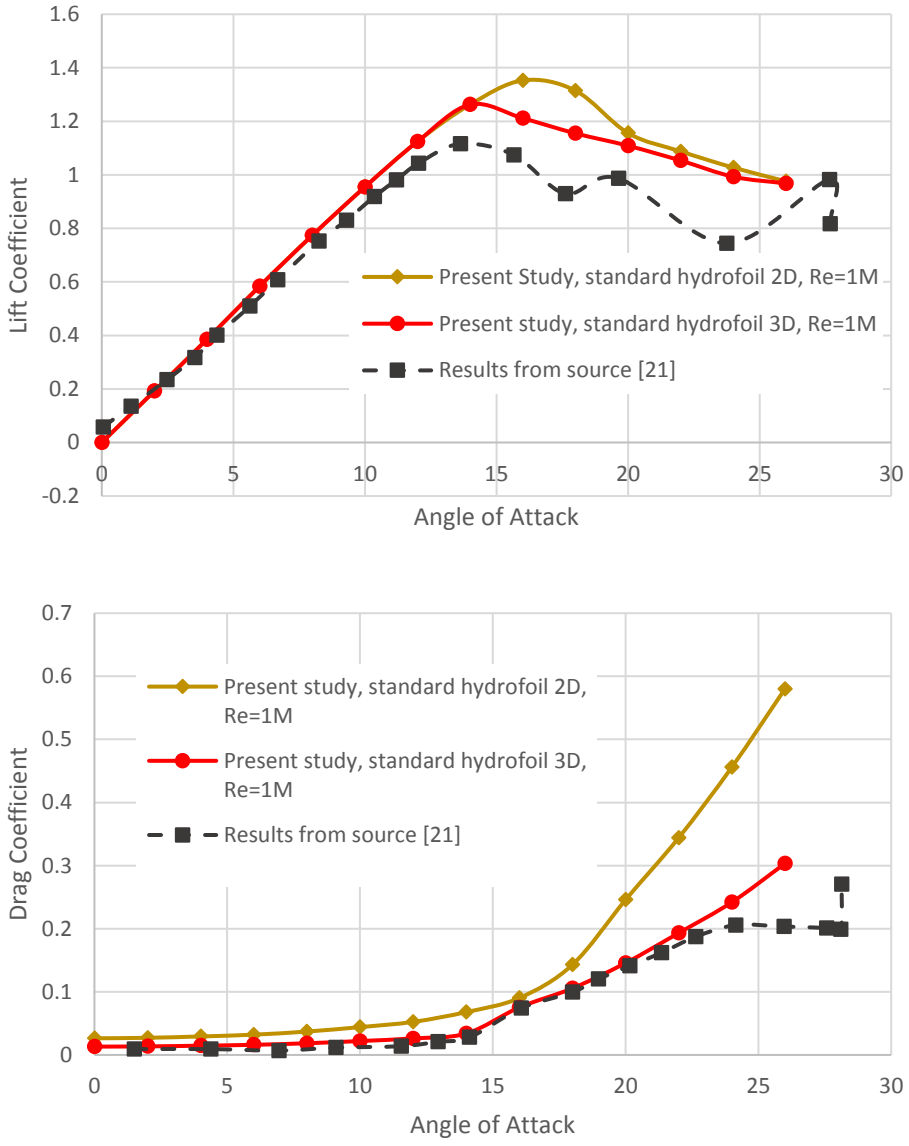

Figure 35: Lift coefficients vs. angle of attack of a standard hydrofoil in 2-D and 3-D (top) and drag coefficients vs. angle of attack of a standard hydrofoil in 2-D and 3-D (bottom), at Re=1,000,000

4.4 Effect of Leading-Edge Tubercles for Re=1,000,000

Following the verification of the standard hydrofoil in a flow with a high Reynolds number by examination of the lift and drag coefficients, the wall shear stress, pressure and velocity magnitude fields were again recorded. Figures 36 to 38 show comparisons of these fields between the standard hydrofoils simulated for flows of Re=120,000 and Re=1,000,000.

The friction lines remain essentially parallel over the hydrofoil for 3 of the angles of attack in figure 36, for the standard hydrofoil simulated in fully turbulent flow conditions. At 16°, a spiral pattern emerged in the friction lines on the top surface of the hydrofoil which could indicate that the turbulence model was unable to resolve the flow. The flow pattern was more uniform at an angle of attack of 24° as indicated in figures 36 (with the friction lines) and 37 (with the uniform pressure field at 24° compared to 16°).

The surface pressure shading in figure 37 suggested that the flow separates almost completely from the top surface of the hydrofoil indicated by the high surface pressure field. A strong negative pressure field at the leading-edge corresponding to the location of the high velocity fluid particles was observed as in figure 37 for both laminar/transitional and turbulent flow conditions.

It could be seen from figure 38 that the change in flow conditions had a significant impact on the fluid with the hydrofoil. Comparing 0° and 8° for different flow conditions in figure 38, the flow fields did not change too much pre-stall although the maximum velocity for the turbulent simulations is slightly higher. Examining the velocity magnitude field results at 16° and 24°, the flow fields look very different to each other in the post-stall regime. The wake regions in figure 38 in the turbulent flow, did not begin at the leading edge like in laminar flow. This was important as it demonstrated that with higher fluid momentum, the flow was remaining attached along the surface of the standard hydrofoil for greater values of α and therefore generating higher lift at those angles. This was further indicated by the lift coefficient plot in figure 35.

As with the simulations performed at Reynolds number of 120,000, there is a skewness in the results. It is seen in figures 36 and 37 for the pressure magnitude and wall shear

stress magnitude, however the skewness in the results appears to start at a lower angle of attack with the higher Reynolds number. This is probably due to the higher Reynolds number which is reflective of fully turbulent flow, so the magnitude of the negative adverse pressure gradient will be much greater and therefore more difficult for RANS to accurately resolve.

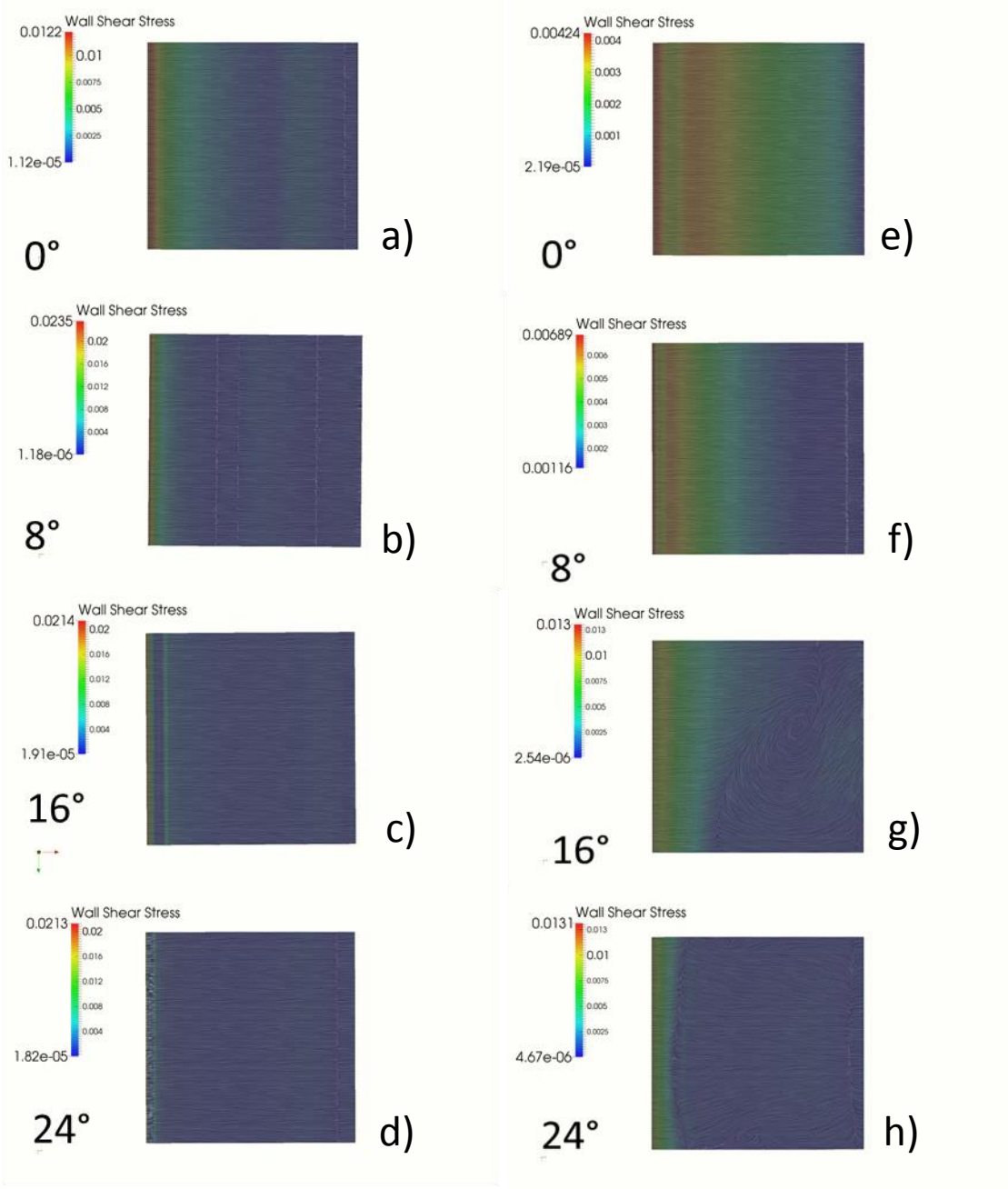

Figure 36: Wall shear stress magnitude field with friction lines on the top surface of a standard hydrofoil for Re=120,000 (left) and Re=1,000,000 (right) at α=0°, α=8°, α=16°, and α=24°

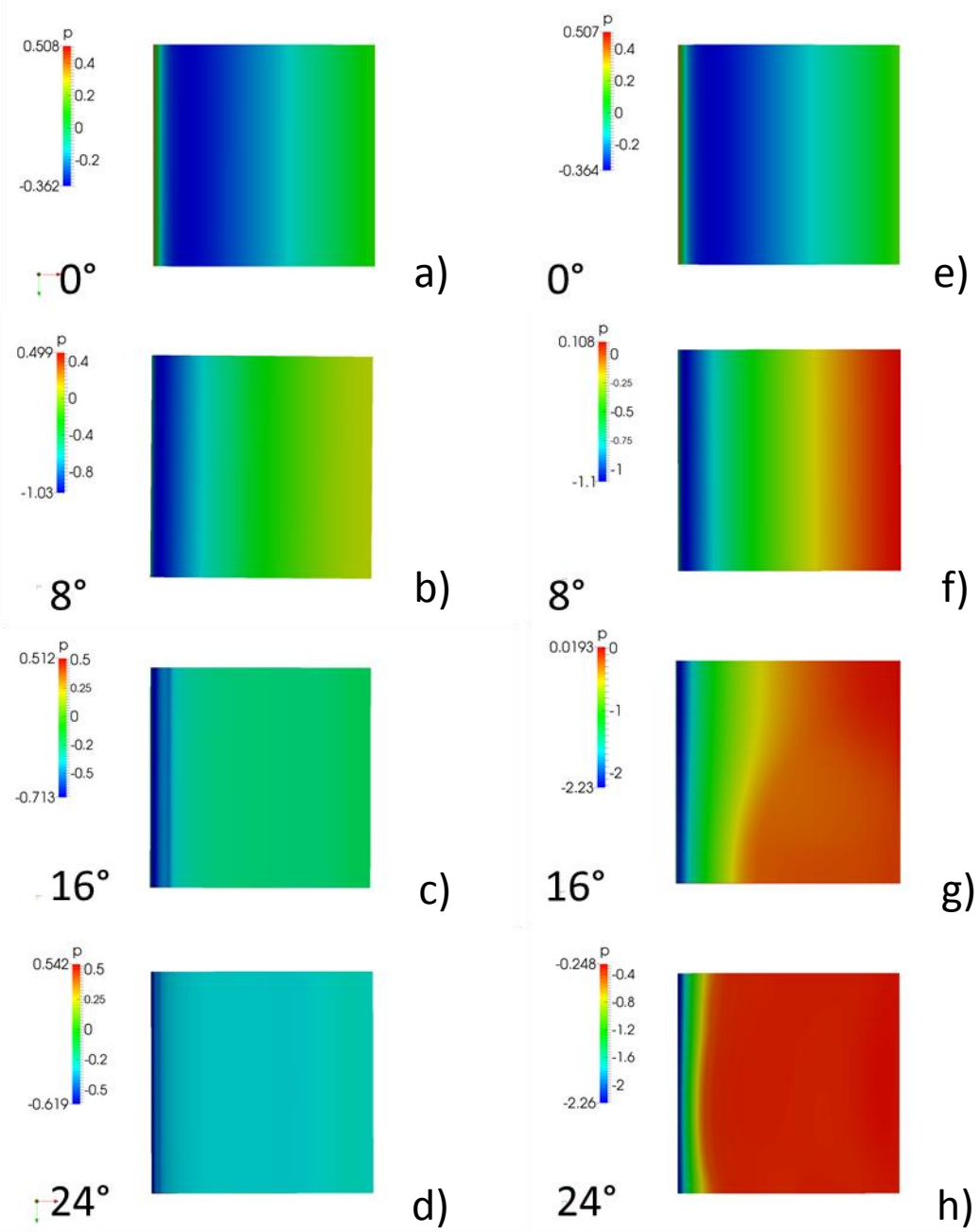

Figure 37: Pressure field on the top surface of a standard hydrofoil for Re=120,000 (left) and Re=1,000,000 (right) at α=0°, α=8°, α=16°, and α=24°

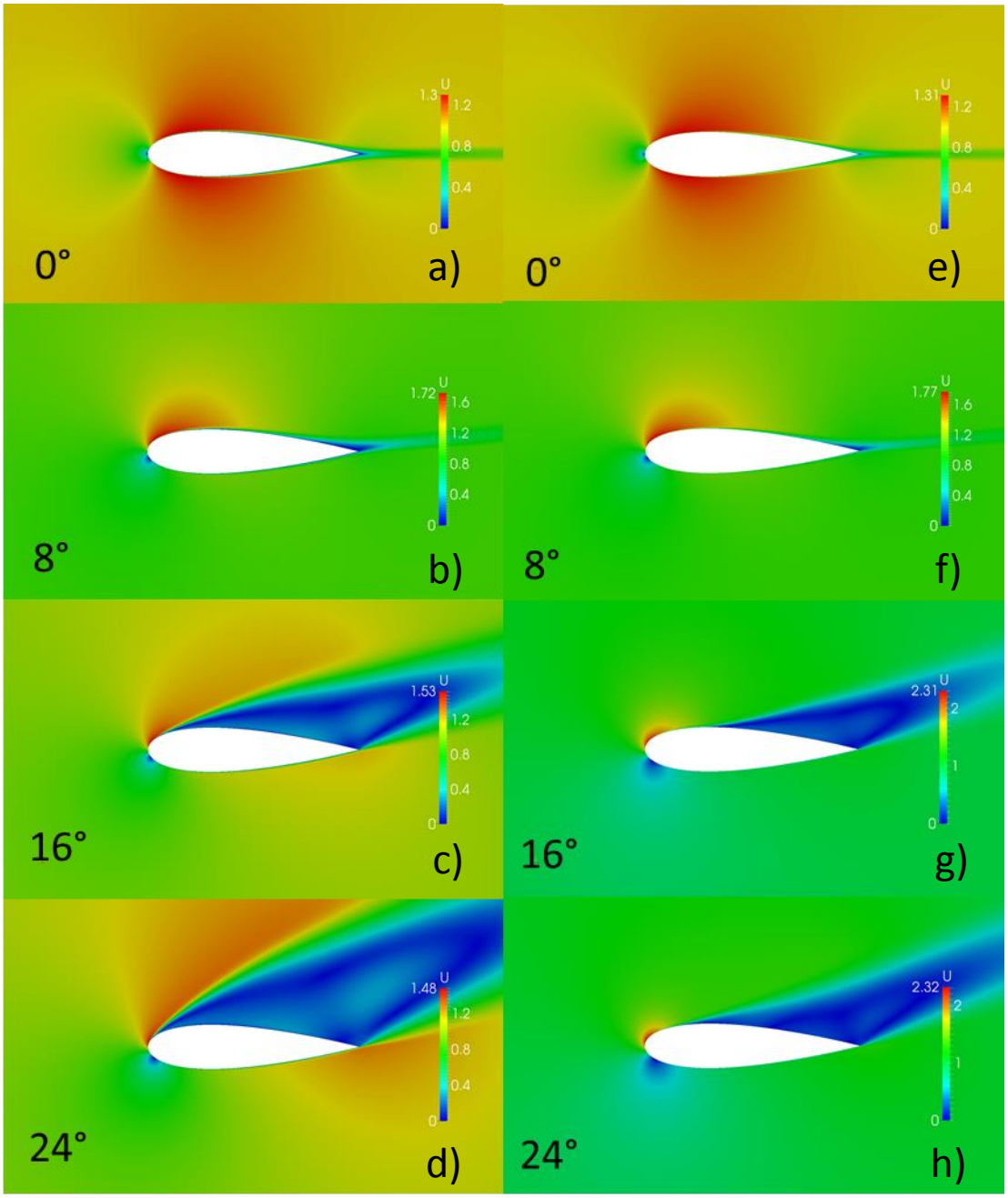

Figure 38: Velocity magnitude field of a standard hydrofoil for Re=120,000 (left) and Re=1,000,000 (right) at α=0°, α=8°, α=16°, and α=24°

The three tubercle profiles of the leading-edges were tested under the same conditions as the standard hydrofoil. The value of Re=1,000,000 was much more significant to the research when compared with the lower Reynolds number tested, as it simulated

velocities and flow conditions experienced by the humpback whale during hunting. The specific reasons for testing at this value for Re and tubercle profiles were:

a) These tubercle amplitudes along leading-edge lead to the hydrofoil experiencing complex 3-D flow once the angle of attack exceeded 20° indicated on the C_l plot (figure 30) and the wall shear stress fields (figures 24 and 31), therefore it was desirable to see if that still held true under lunge speed conditions.
b) It had been theorised that the humpbacks tubercle pectoral flippers exist on this particular species of cetacean whale and no others because of the whales' unique bubble net feeding method. Hence testing under feeding conditions for a leading-edge that resembled closely a section of the humpbacks was necessary to see if the simulations supported the hypothesis.

The lift and drag coefficients for all the hydrofoils tested at Re=1,000,000 are recorded in figure 39. The C_l and C_d plots in figure 39 indicated that the addition of the tubercles did not have a positive impact on the hydrodynamic performance of the hydrofoil in the pre-stall region for turbulent flow as was also the case with laminar flow. The difference post-stall, when compared to laminar flow predictions, was that the hydrofoil with the uniform leading-edge generates greater lift post-stall in addition to pre-stall when compared to any of the hydrofoils with sinusoidal leading-edges. For the 10% amplitude hydrofoil, the lift coefficient had the most gradual stall starting at 6° and ending at 14°. The results of the other two hydrofoils in the lift coefficient plot post-stall, deviate from the expected values between the angles of 14° and 20° attack angle when compared to results from [17], [11], [10] and [26]. The hydrofoil with the 2.5% leading-edge appears to have a sharp drop in lift coefficient over this post-stall linear region of the graph whereas the 4% leading-edged hydrofoil lift coefficient values increase slightly as the angle of attack increases. Errors in the results post-stall are likely the result of a high adverse pressure gradient magnitude and the limitations of the RANS and Spalart-Allmaras models. This is discussed further in Section 4.9. Looking at the drag plot in figure 39, the drag coefficient is still lower for the unmodified hydrofoil. The overall drag on the hydrofoils appeared to be affected by the addition of leading-edge tubercles with greater values recorded for hydrofoils with

larger tubercles as can be seen in figure 39. The simulation which produced the lowest C_d values was again the standard hydrofoil. The hydrofoil with the highest C_d values had tubercles along the leading-edge 10% of the chord length.

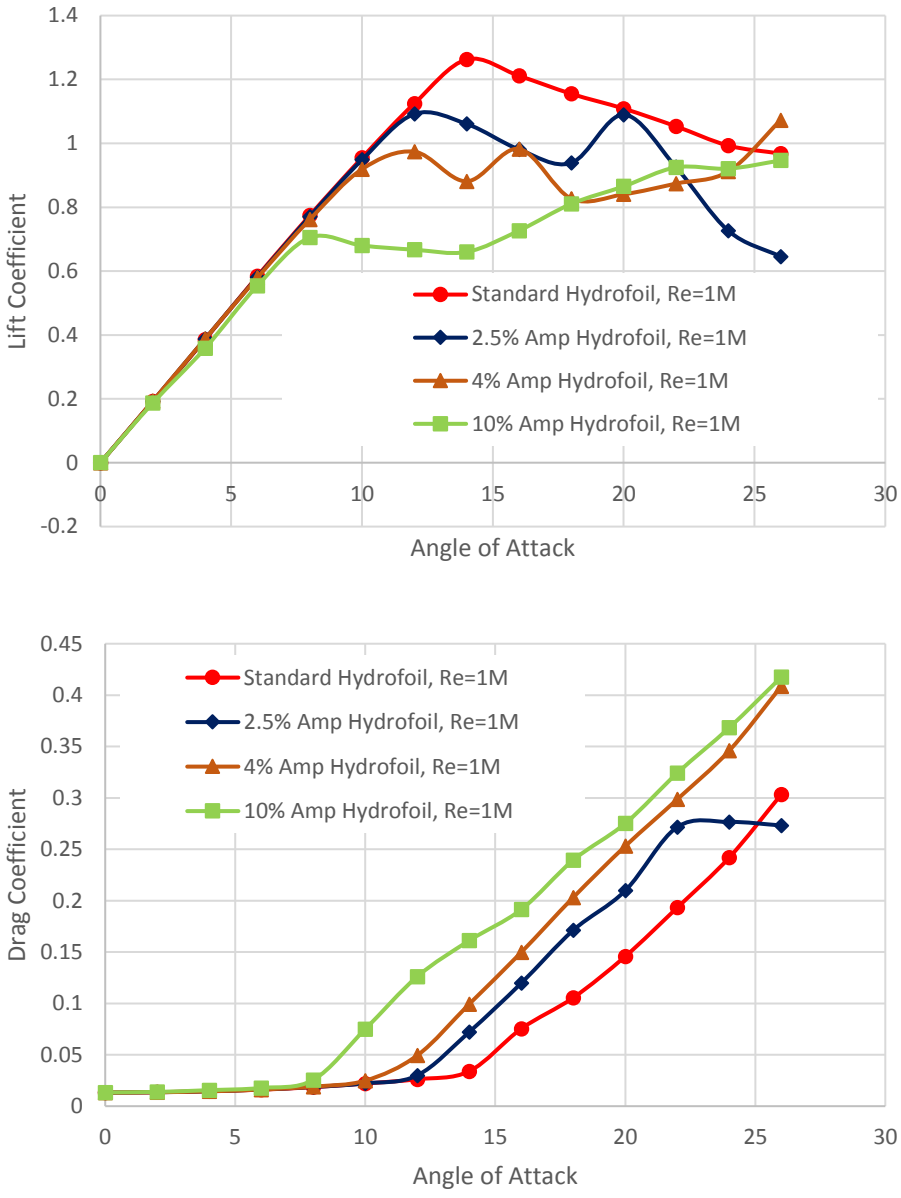

Figure 39: Lift coefficients (top) and drag coefficients (bottom) vs. angle of attack of hydrofoils with standard, 2.5, 4% and 10% sinusoidal leading-edges, at Re=1,000,000

Figures 39 to 47 show the comparison of the wall shear stress, pressure and velocity magnitude fields between each of the hydrofoils. Figures 40 and 41 show the different friction line patterns for the hydrofoils in the flow with Re=1,000,000. For the standard and the 4% amplitude hydrofoils, the flow was asymmetrical at 16°. The spiral pattern did not emerge on the hydrofoils with larger tubercles which indicated the pattern was most likely caused by the limitations of the modelling rather than being a realistic representation of the stress lines. Several other asymmetrical flow patterns were observed due to the limits of the RANS equations model. At 0°, only the hydrofoil with tubercles of 10% amplitude had friction lines that were not parallel. Symmetrical converging stress line patterns downstream of the leading-edge troughs were present on the 10% amplitude hydrofoil for all angles of attack, for 4% at all angles of attack higher than 8° and for 2.5% at all angles of attack higher than 16°. The highest wall shear stress was at the leading-edge of the standard hydrofoil and in the trough for the hydrofoils with sinusoidal leading edges.

For the pressure fields; the blue regions in between the tubercles as demonstrated in figures 42 and 43 were evidence of a larger negative pressure coefficient and faster flow both pre- and post-stall. Figures 42 and 43 showed that increasing the size of the tubercles decreased the pressure coefficient values between the troughs but gave higher values along the rest of the surface to the trailing edge. Although the flow separated in the trough, it appeared to remain attached at the peaks even after stall, as was observed with the lower Reynolds number simulations. This was further explored in the examination of the velocity profile at the peaks and troughs in figures 44, 45, 46 and 47. For all hydrofoils at a non-zero angle of attack, the highest pressure recorded was at the trailing edges.

Although the fluid appeared to flow faster through the troughs more as the tubercle size increased, the flow still separated from the surface evidenced by the early loss of lift (figure 39), friction coefficient field (figures 40 and 41) and the pressure coefficient field (figures 42 and 43). As previously stated, there appeared to be a correlation between the magnitude of the tubercles along the leading-edge and the flow remaining attached along those tubercles for higher angles of attack. This remained the same

regardless of the magnitude of the Reynolds number. Although the flow appeared to remain attached to the surface (see figures 45, 46 and 47) it also caused premature separation at the trough and so was detrimental to the performance of the hydrofoil in both laminar and turbulent flow fields. The velocity fields recorded for the standard hydrofoil under turbulent flow conditions in figure 44, did not have wake regions beginning at the leading-edge for any angles of attack. Additionally, the unmodified hydrofoil velocity profile at 24°, the flow appeared to separate where the thickness of the hydrofoil is maximum, whereas for the sinusoidal leading-edge hydrofoils of all magnitudes, the separation occurred at the leading-edge in the trough and further downstream than the standard hydrofoil at the peak, exact location dependent on tubercle magnitude. The profiles resembled the flow fields in figures 45, 44 and 45 for the peaks as the flow remained partially attached to the leading-edge of the hydrofoil as it did over the peak of the tubercles.

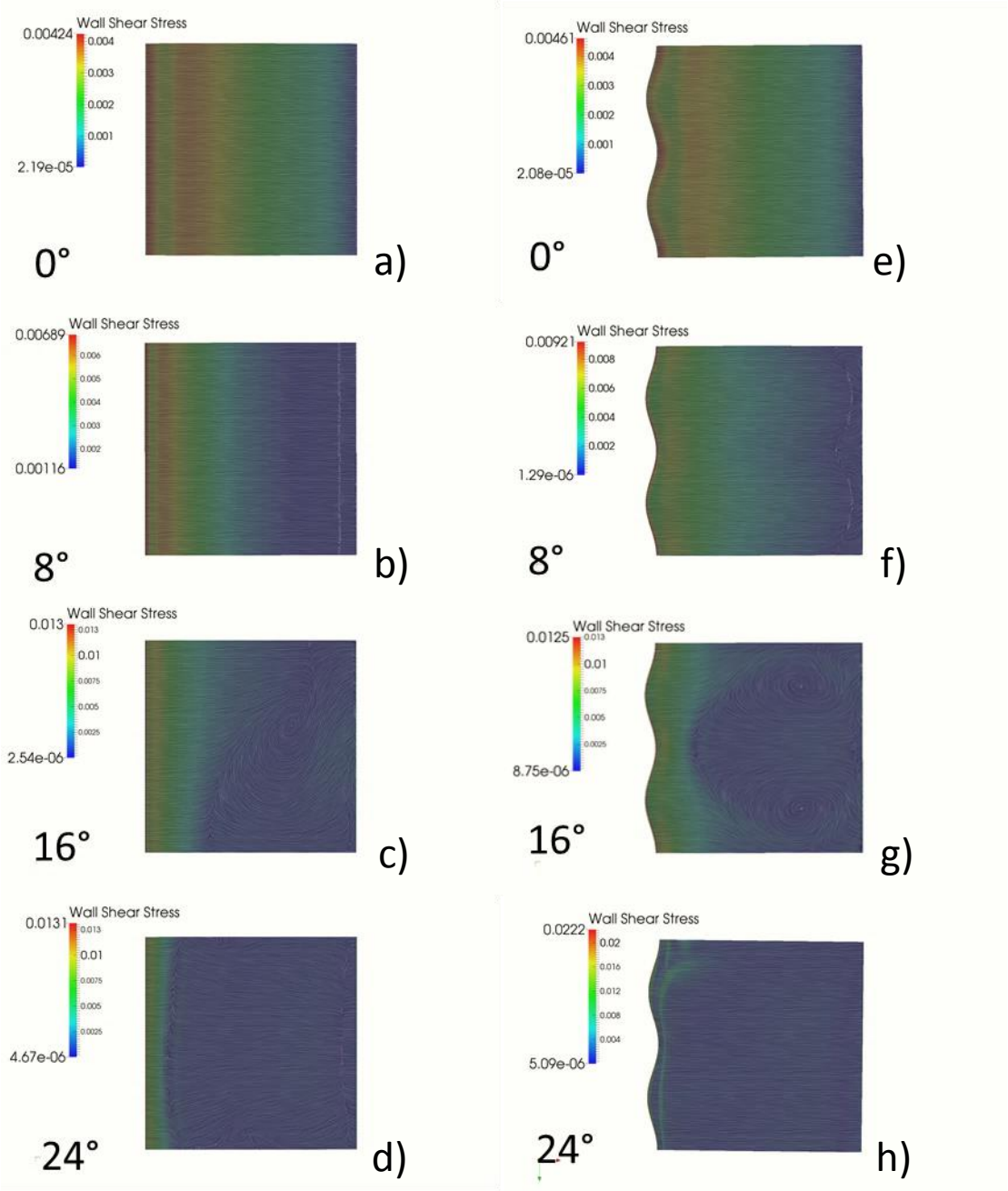

Figure 40: Wall shear stress magnitude field with friction lines on the top surface of a standard hydrofoil (left) and a hydrofoil with a sinusoidal leading-edge of 2.5% amplitude (right) at α=0°, α=8°, α=16°, α=24° at Re=1,000,000

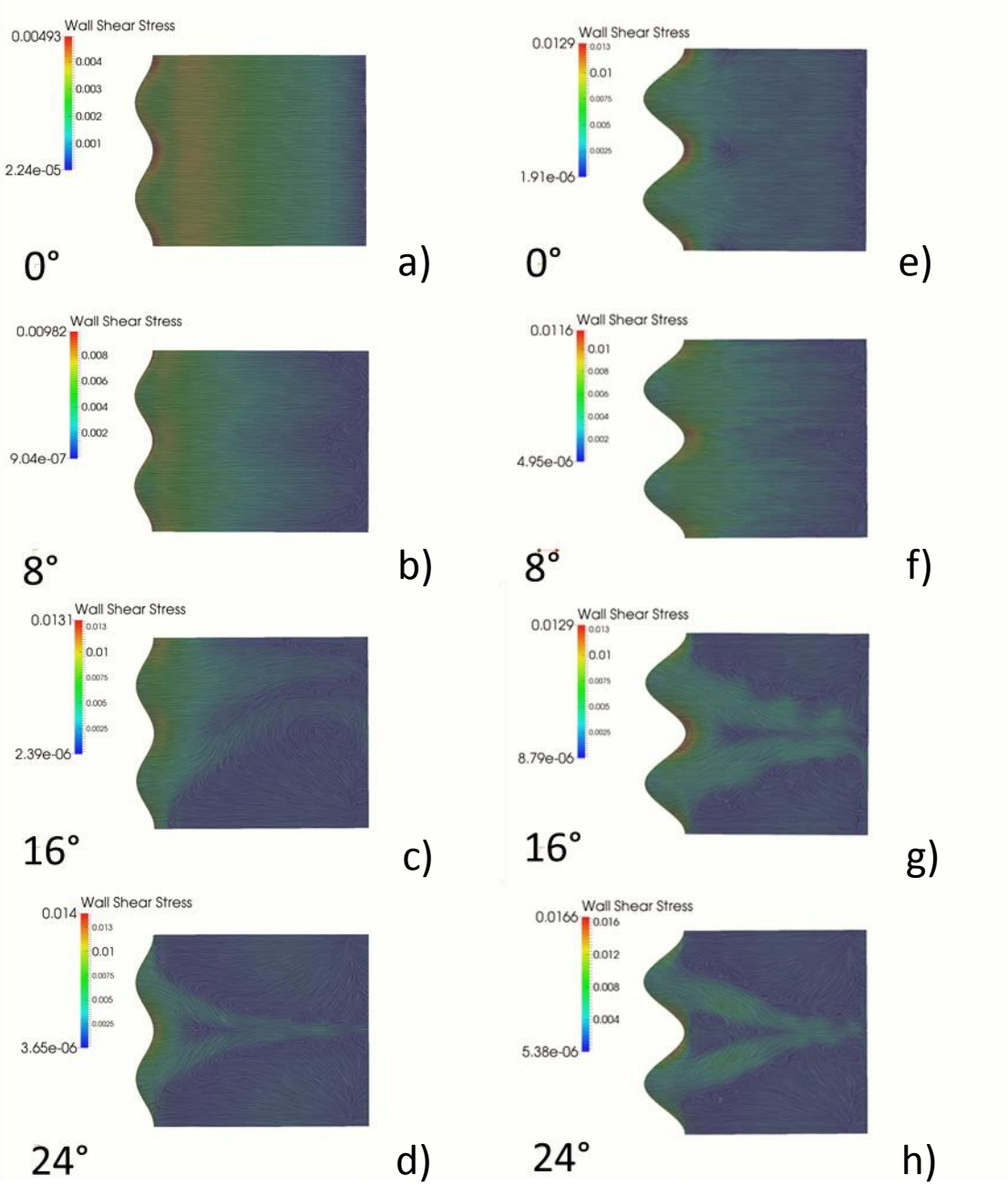

Figure 41: Wall shear stress magnitude field with friction lines on the top surface of a hydrofoil with a sinusoidal leading-edge of 4% amplitude and a 10% amplitude at α=0°, α=8°, α=16°, α=24° at Re=1,000,000

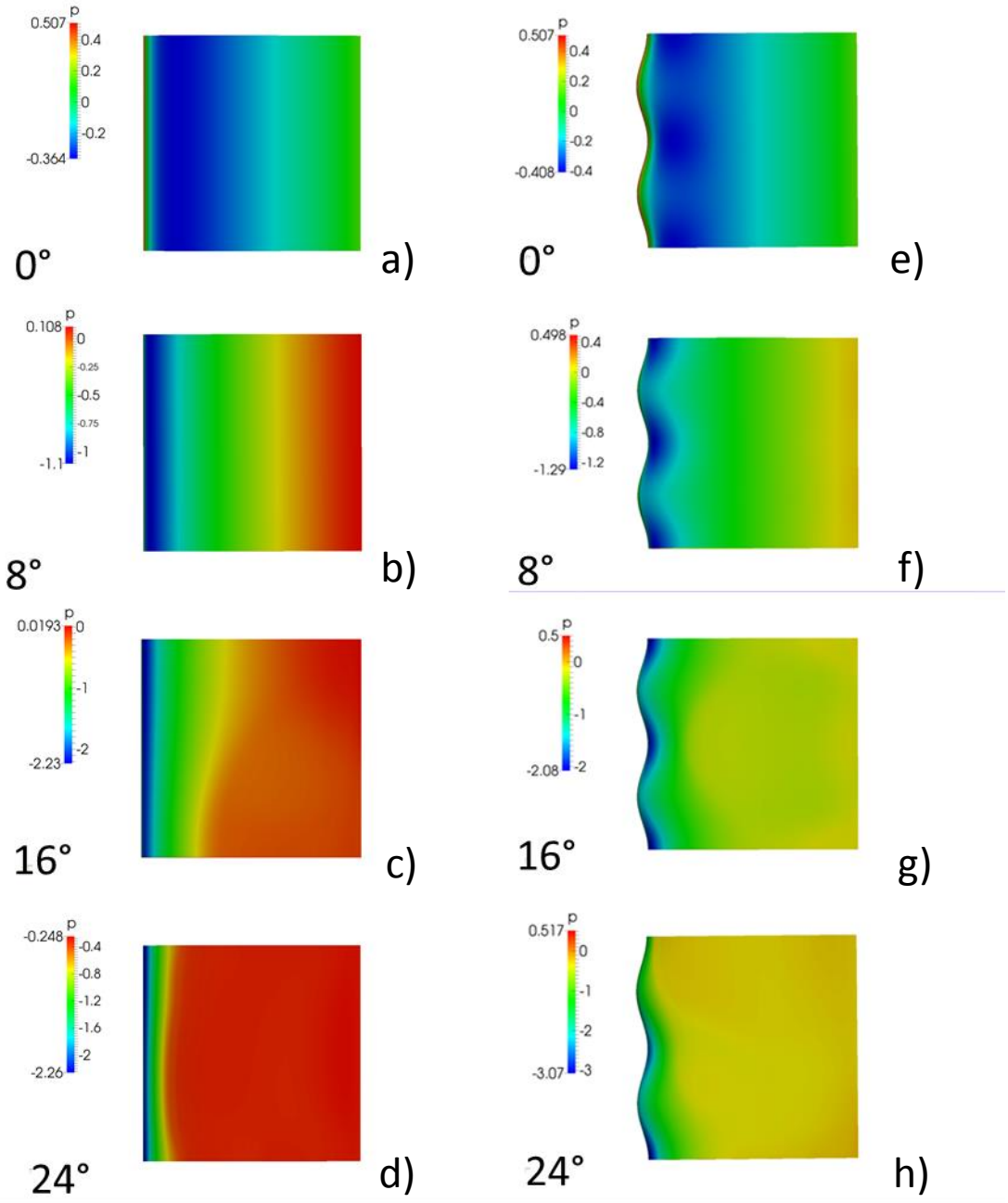

Figure 42: Pressure field on the top surface of a standard hydrofoil and a hydrofoil with a sinusoidal leading-edge of 2.5% amplitude at α=0°, α=8°, α=16°, α=24° at Re=1,000,000

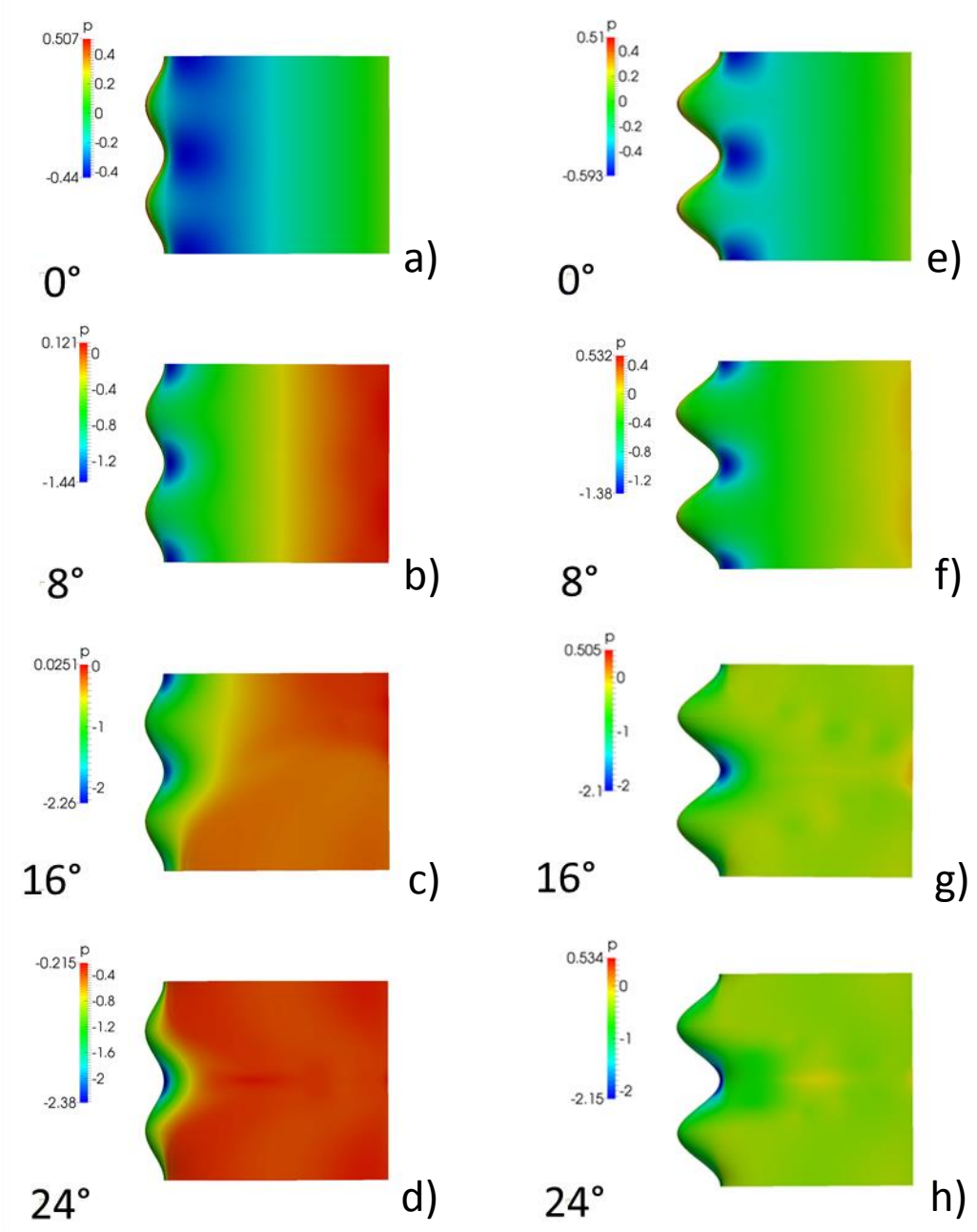

Figure 43: Pressure field on the top surface of a hydrofoil with a sinusoidal leading-edge of 4% amplitude and 10% amplitude at α=0°, α=8°, α=16°, α=24°, at Re=1,000,000

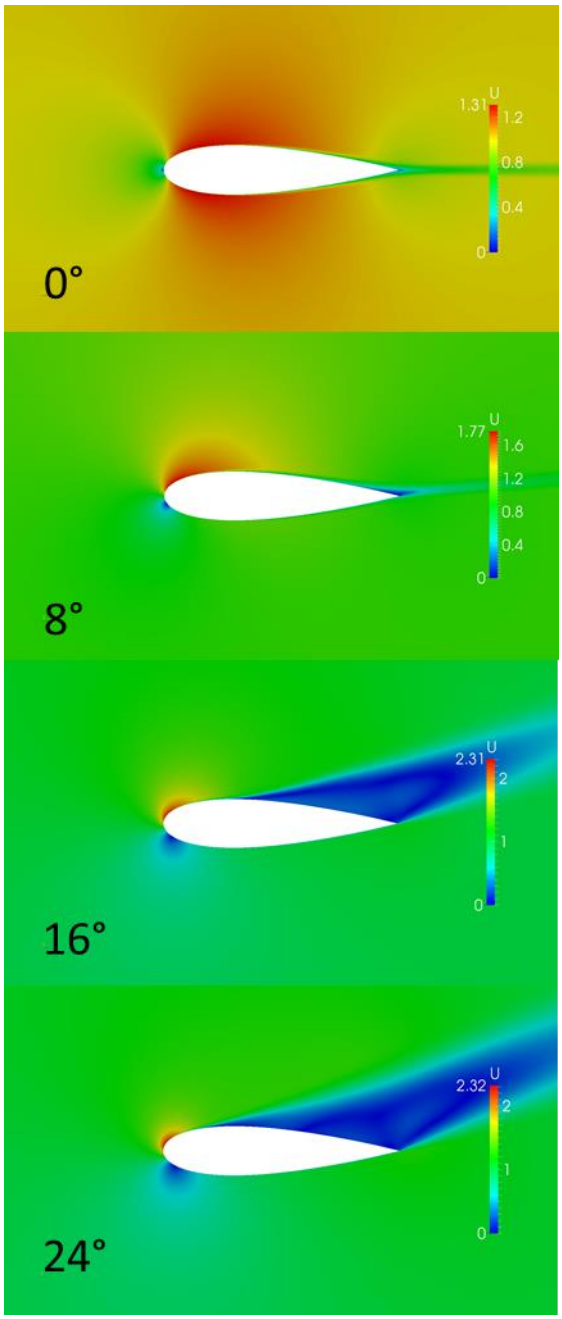

Figure 44: Velocity magnitude field of a standard hydrofoil at α=0°, α=8°, α=16°, α=24° at Re=1,000,000

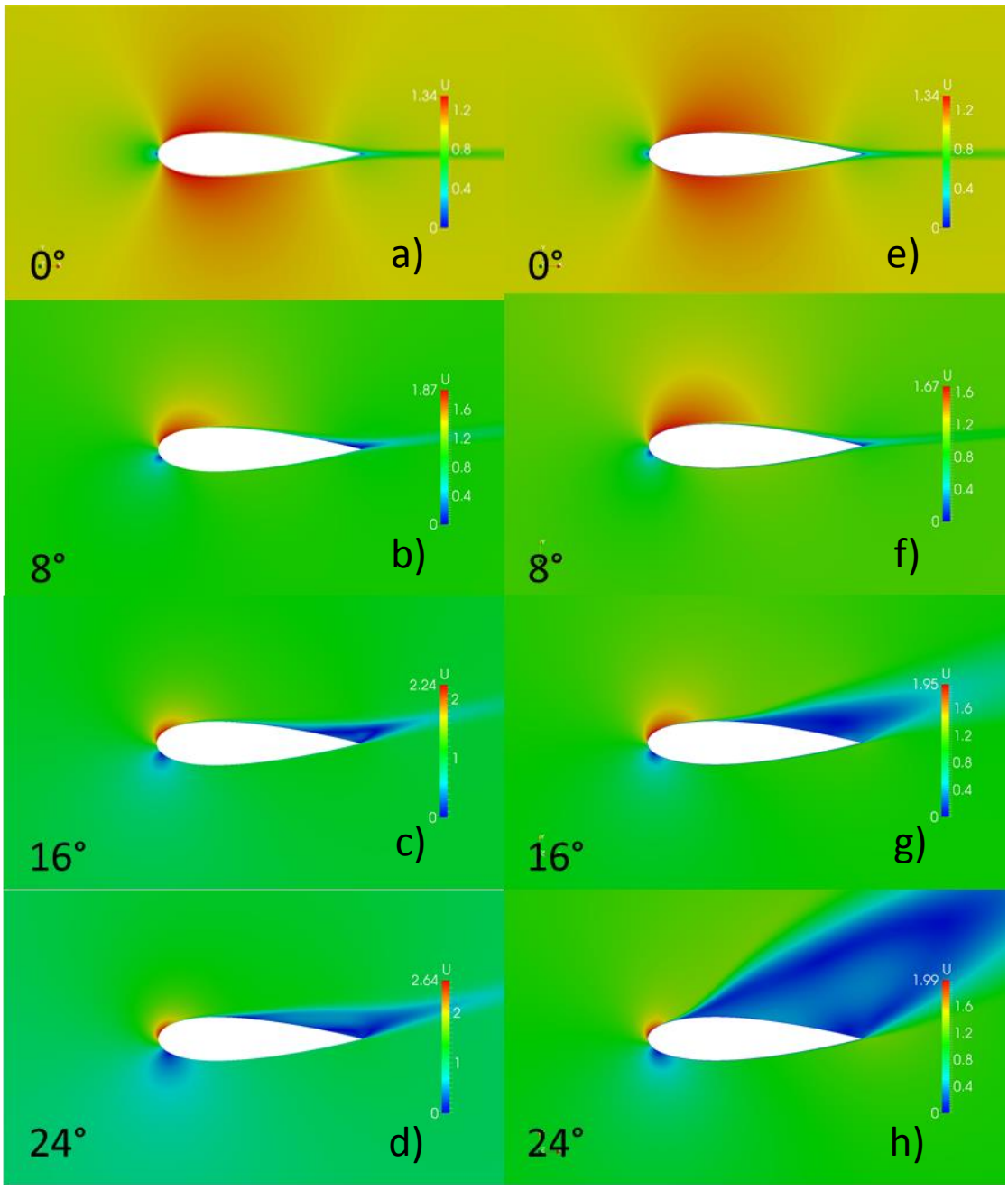

Figure 45: Velocity magnitude field of a hydrofoil with a sinusoidal leading-edge with a 2.5% amplitude at α=0°, α=8°, α=16°, α=24°, at the peak (left) and at the trough (right), at Re=1,000,000

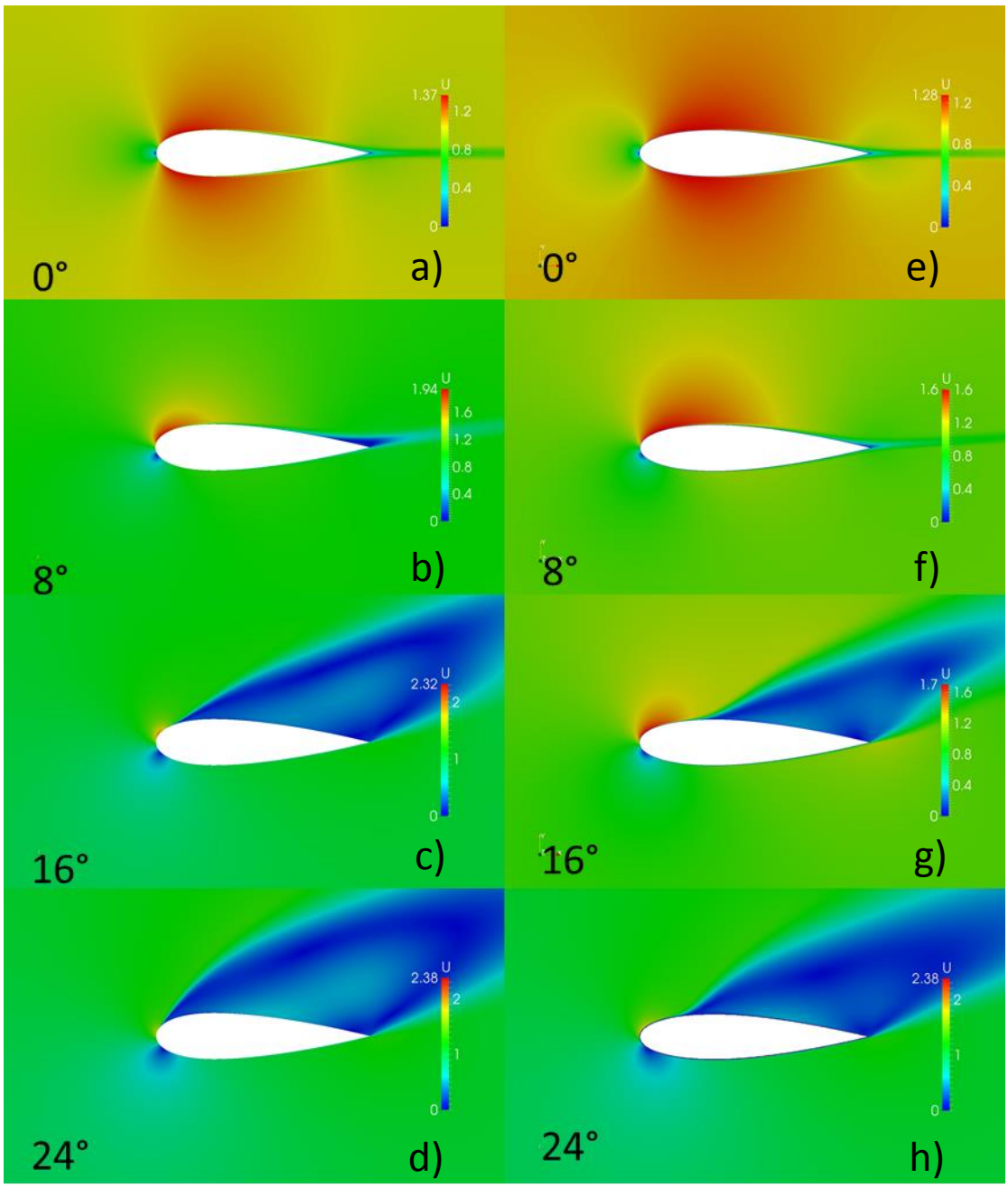

Figure 46: Velocity magnitude field of a hydrofoil with a sinusoidal leading-edge with a 4% amplitude at α=0°, α=8°, α=16°, α=24°, at the peak (left) and at the trough (right), at Re=1,000,000

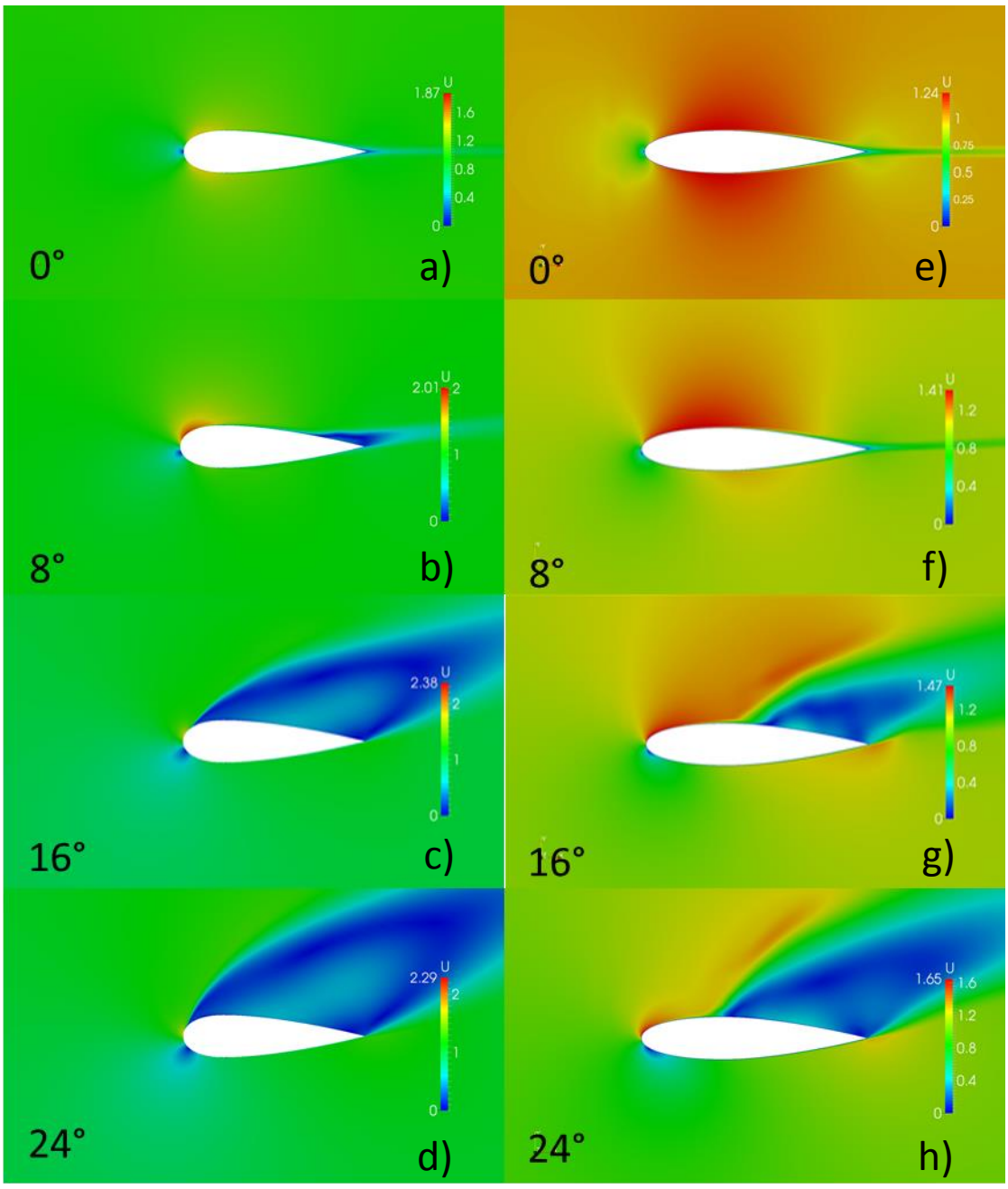

Figure 47: Velocity magnitude field of a hydrofoil with a sinusoidal leading-edge with a 10% amplitude at α=0°, α=8°, α=16°, α=24°, at the peak (left) and at the tough (right), at Re=1,000,000

4.5 Effect of Leading-Edge Tubercles for Re=2,770,000

The final set of simulations were performed on the same hydrofoils used in the previous simulations for the maximum velocity at which a humpback whale is capable of traveling. The Reynolds number for this experiment was calculated using the dimensions of the pectoral flipper for an average adult humpback, the maximum velocity of a humpback and the kinematic viscosity of sea water which resulted in Re=2,770,000 (see table 6).

The reason for this being tested was to examine any restrictions (such as high C_d) or benefits (such as high C_l) which emerged when travelling at this velocity that were not present for the velocities that corresponded to the flow conditions during hunting.

The results of C_l and C_d at Re=2,770,000 were very simlar to those generated at Re=1,000,000. The reason for this is that both the Reynolds numbers were for fully developed turbulent flow. The lift coefficient plots in figure 48 were consistent with the results in figure 39 as the difference in the values were low and both showed clearly that the hydrofoil with the uniform leading edge had superior lift generation both pre- and post-stall. The C_d plot in figure 48 also followed a similar pattern to all those that were generated before which starts as a gradual increase until the critical angle (12°) and then the values of C_d rise linearly with a high gradient. Comparitively, although the Reynolds number is 2.77 times higher in figure 48 compared to 39, the values for the lift and drag coefficients seem to remain constant indicating that they have the same values for any Reynolds number in fully turbulent flow. It also again showed that the leading-edge with no tubercles generated the least amount of drag and the most favourable lift. The simulations at this Reynolds number also re-confirmed the relationship between the increase in the tubercle amplitude magnitude and the consequent decrease in lift generation pre-stall.

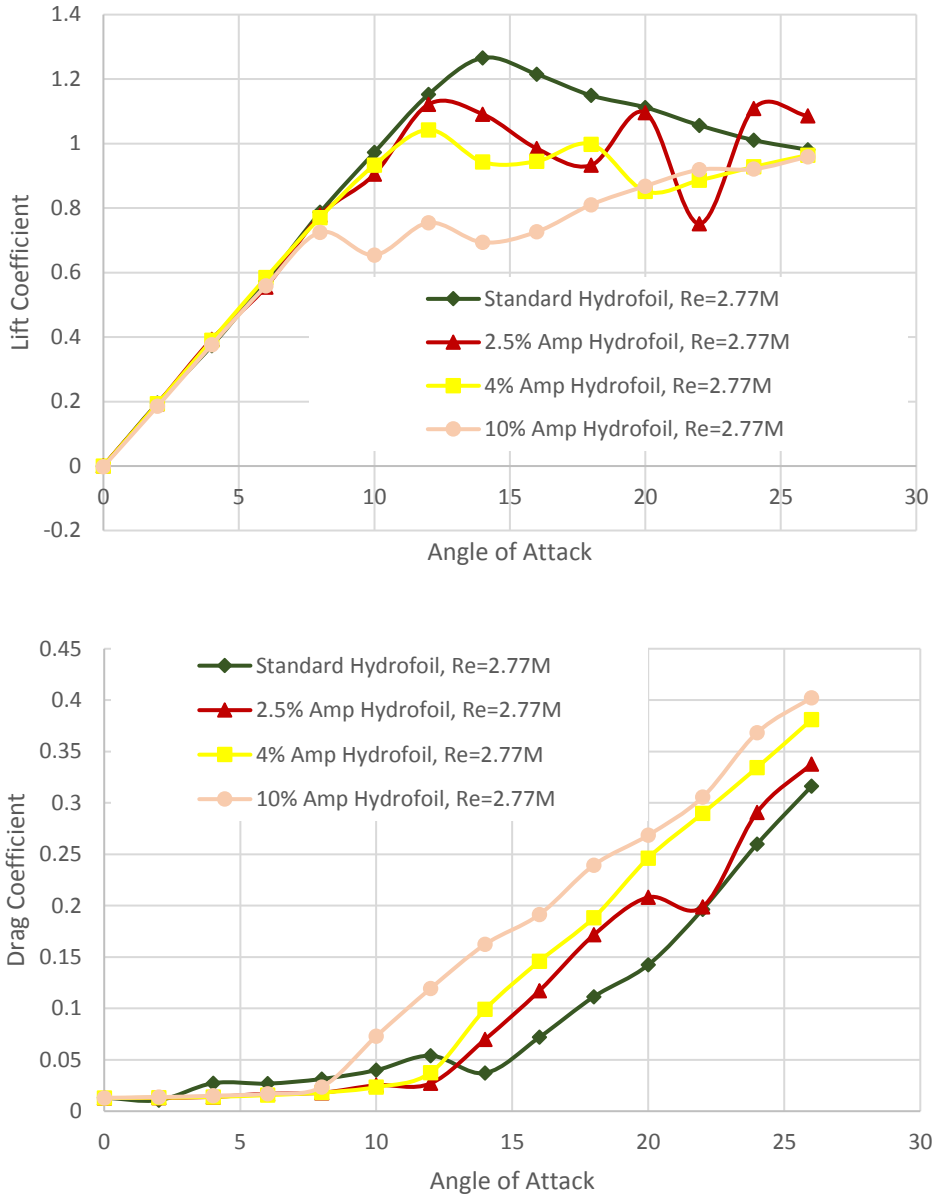

Figure 48: Lift coefficients (top) and drag coefficients (bottom) vs. angle of attack of hydrofoils with standard, 2.5, 4% and 10% sinusoidal leading-edges, at Re=2,770,000

4.6 Vortices Produced in the Flow

Counter-rotating vortices were generated downstream of the leading-edge tubercles on the suction side of the hydrofoil. There appeared to be a relationship between the size of the tubercles and the strength of the vortices generated. It should be noted that the resulting vortices produced at high angles of attack (16° and higher) in RANS are approaching the limit of the simulation capabilities as the flow becomes increasingly more unsteady which may lead to skewed vortices. This is discussed further in Section 4.9.

Figures 49 and 50 show the isocontours for a constant Q value with the magnitude of the velocity shown on the scale. Q is the second invariant of the velocity gradient tensor and is a good indicator of turbulent flow structures. The isocontours at Q=0.00144 for all four hydrofoil profiles at Re=120,000 and Re=1,000,000, for α=8° and α=16° are shown in figures 49 and 50 respectively, with the velocity magnitude. As observed from comparing the hydrofoils in figure 49, the size of the vortices generated increased with the value of α and the size of the tubercles. The standard hydrofoil did not induce stream-wise vortices owing to the infinite span (no tip vortices). The Q isocontour shape generated for the leading-edge tubercles of 2.5% amplitude is unique in that the magnitude was largest in the centre as was observed from figure 49. The fields generated from the 4% and 10% amplitude leading-edge tubercles are similar in size to each other however the largest tubercles generated the largest isocontours. As expected, the velocity magnitude was larger at 8° rather than 16° for all hydrofoils, close to the maximum width of the hydrofoil, at the leading edge, and between the tubercles for the hydrofoils with a sinusoidal leading edge.

Contrasted to the hydrofoil simulations with the Reynolds number of 120,000 in figure 49, the isocontours generated for Reynolds number of 1,000,000 in figure 50 are smaller in size but stronger in magnitude. This was expected for turbulent flow as the wake region is smaller in turbulent conditions. In figure 50 the isocontours in the standard and 4% hydrofoils were asymmetrical which may have been an indication that they were the result of complex 3-D flow over the hydrofoil at certain angles of attack. The isocontours for the hydrofoil with tubercles of 10% were more complex than the other hydrofoils for both Reynolds numbers. The higher velocities were

recorded in the simulations with higher Reynolds numbers and the highest was in the simulation with the hydrofoil of 10% tubercle amplitude.

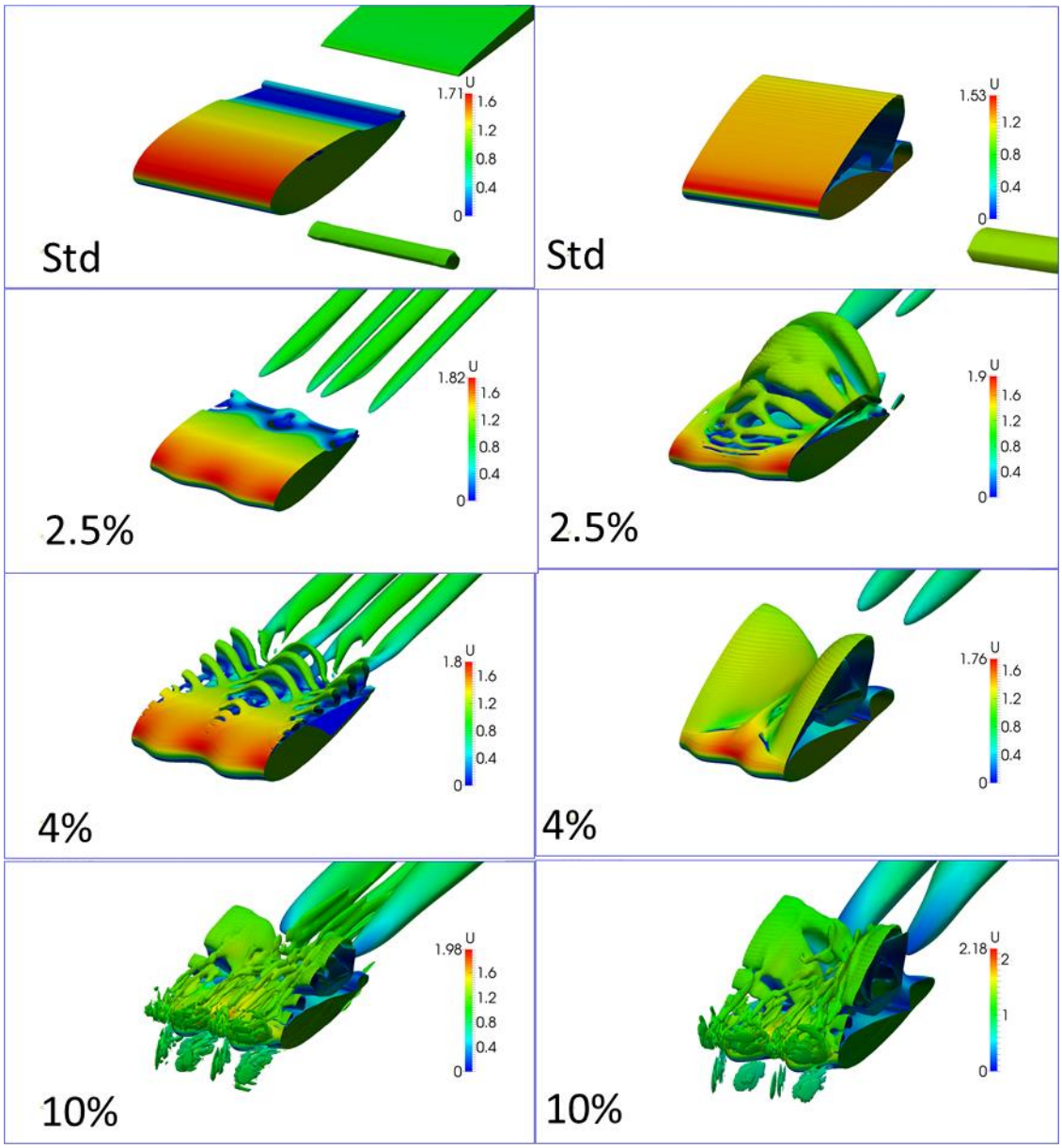

Figure 49: Isocontours for Q=0.00144, at Re=120,000 for hydrofoils of different tubercle amplitudes at α=8° (left) and α=16° (right)

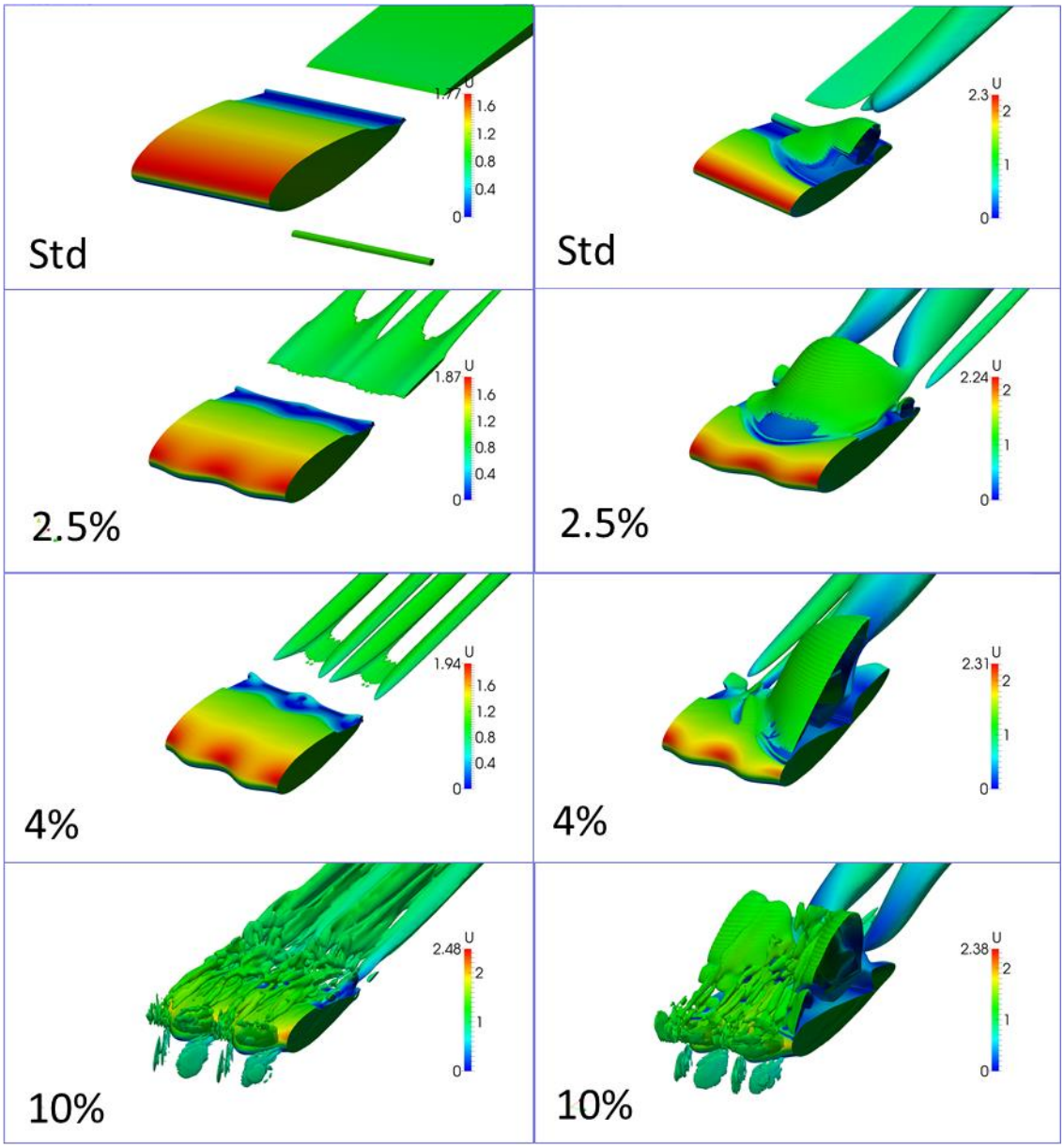

Figure 50: Isocontours for Q=0.00144, at Re=1,000,000 for hydrofoils of different tubercle amplitudes at α=8° (left) and α=16° (right)

4.7 Maximum Coefficient of Lift and Stall Angle of Attack

The hydrodynamic characteristics of hydrofoils with protuberances were found to be very different than those for a hydrofoil with a straight leading-edge of equivalent surface area. Table 8 summarises the stall angle and maximum lift coefficients of each hydrofoil. It allowed determining the most efficient hydrofoil leading-edge profile. As can be seen from table 8, change in the flow conditions had a significant impact on the hydrodynamic performance on the hydrofoil.

From the results in table 8, the most efficient hydrodynamic performance was of a standard hydrofoil in fully developed turbulent flow. Although not shown on the table, in comparing figures 30, 39 and 48, the drag values are lower in a turbulent flow. The reason for this is that, in a turbulent flow, the boundary layer around the hydrofoil has enough energy to overcome the adverse pressure gradient at the surface for greater angles of attack and thus performance is improved. The addition of tubercles along the leading-edge of the hydrofoil did not improve hydrodynamic performance in the pre-stall region for laminar flow or in the pre-stall and post-stall regions for turbulent flow.

For the post-stall region in laminar flow however, the hydrofoils with tubercles showed higher values of lift and drag. It was also observed from the figures 30, 39 and 48 that the hydrofoils with sinusoidal leading edges did not stall the same way as the uniform hydrofoils. Instead of flow separation occurring uniformly along the span, a hydrofoil with a scalloped leading-edge, had areas of separation (the troughs) and areas where the flow remained attached (the peaks), which proved beneficial to lift generation post-stall.

One possible reason for the lower lift and drag coefficients pre-stall caused by leading-edge tubercles could be linked to the tubercles providing a way for the fluid to more easily flow from the high pressure side (under the hydrofoil) to the low pressure side (top of the hydrofoil) which resulted in counter rotating vortices downstream of the leading-edge on the suction side. It should be also noted that the experiments to which this study has been compared were to hydrofoils which had uniform mean chord lengths and occupied the height of the wind-tunnels in which they were tested eliminating the possibility of wing-tip vortices. The data from the simulations indicates that the tubercles in isolation do not improve lift and drag characteristics for pre- and post-stall angles of attack as was originally hypothesised. The only region for which

the tubercles provided any benefit was post-stall for flow of Re=120,000. The value of C_l that the hydrofoils with sinusoidal leading-edges had post stall, were different in flows of Re=120,000 depending on the tubercle amplitude. The results of these hydrofoils are similar and follow the same trend. For the simulations with higher Reynolds numbers however, the values of C_l post-stall were different depending on the tubercle amplitude.

Table 8: Comparison of main hydrodynamic characteristics

Reynolds Number	Hydrofoil Leading-edge	Max C_l	Stall Angle of Attack α in degrees
120,000	Standard	1	12
	2.5% Amplitude	0.85	10
	4% Amplitude	0.62	8
	10% Amplitude	0.5	6
1,000,000	Standard	1.3	14
	2.5% Amplitude	1.1	12
	4% Amplitude	1	10
	10% Amplitude	0.7	8
2,770,000	Standard	1.3	14
	2.5% Amplitude	1.15	12
	4% Amplitude	1.05	12
	10% Amplitude	0.75	10

4.8 Effect of Reynolds Number

The results from the simulations of hydrofoils that were used; as the baseline model (standard), attempting to generate results similar to the base-line model (2.5%) and the simulation with the largest vortices (10%), were compared on the lift and drag coefficients for the same leading edges at different Reynolds numbers. The purpose was to demonstrate that the type of flow had a significant impact on the coefficients of lift and drag generated from the hydrofoil.

Examination of the lift and drag plots in figure 51 showed that the post-stall performance of the standard hydrofoil was superior in turbulent flow conditions. As observed from the lift coefficient plot, the hydrofoil in laminar flow stalled at 12°, with a maximum value of 0.99, which resulted in a drastic loss of lift. Comparitively, both the hydrofoils simulated in turbulent conditions stalled at 14° at a maximum of approximately 1.25 for angles of attack greater than 14° began to gradually decline. Similarly in the drag coefficient plot, the values of drag for the hydrofoils in turbulent flow were significantly lower than the hydrofoil in laminar flow post-stall. Once stall occurred the initial decline in lift value is gradual and small for both laminar/ transitional and turbulent flow. This is why for laminar/transitional flows, the leading-edge protuberances provide higher lift coefficients compared to standard hydrofoils which have a sudden loss of lift at the stall angle.

In figure 52, for a hydrofoil with a leading-edge amplitude of 2.5%, the value for C_l was much higher for the results simulated in a turbulent flow compared to a laminar/transitional flow. The values remained essentially identical between hydrofoils tested at the high Reynolds numbers for angles of attack less than or equal to 20°.

Examining the drag coefficient plot in figure 52, for the hydrofoils in turbulent flow conditions, the values for C_d were overlayed until α=20°. The stall angle was 10° for the laminar flow and 12° for the turbulent flow. The Cd plot for all Reynolds numbers maintained the same post-stall gradient. As with the unmodified hydrofoil, the stall angle was higher for turbulent flow than laminar flow, increasing from 10° to 12°.

For figure 53, the hydrofoil has a sinusoidal leading-edge with an amplitude of 10% and it appears to have significant differences in its performance post-stall between flow types. In a turbulent flow field however, the hydrofoil performs differently. When the critical angle is reached there is almost a 0% drop in lift and instead the lift coefficient remains constant until approximately 14° and then the value starts to increase again. Just as with figure 49, the drag coefficient plot in figure 50 has lower values for the hydrofoils simulated in turbulent flow. The plots of C_d from Re=1,000,000 and Re=2,770,000 overlap such the difference in their values is practically negligible. This meant that the same drag coefficients were present in the both turbulent flows on the hydrofoils.

The conclusion drawn from figures 51, 52 and 53 was that unless the application of the hydrofoil called for constantly high angles of attack in laminar flow, the addition of tubercles to the leading-edge would not improve hydrodynamic performance.

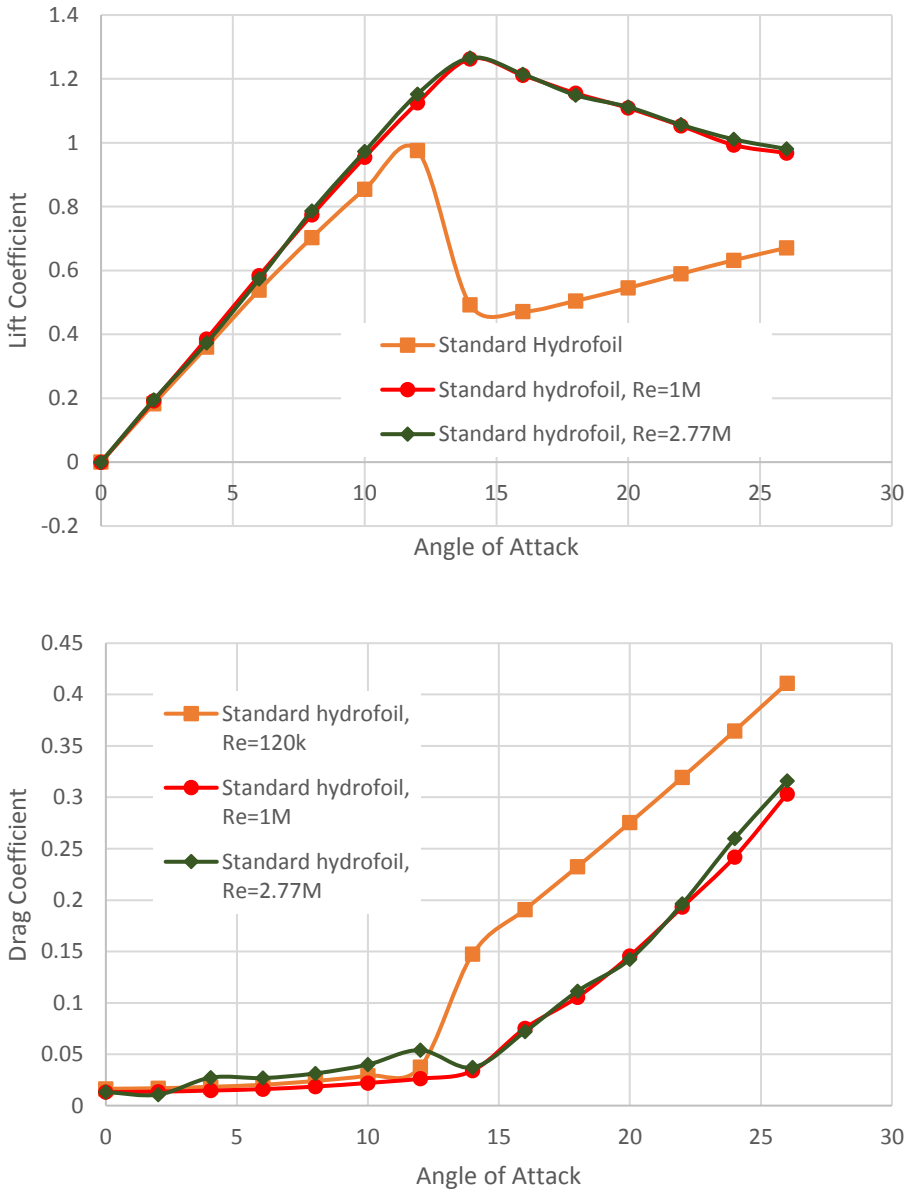

Figure 51: Comparison of the lift and drag coefficients for the standard hydrofoil at Re=120,000, Re=1,000,000 and Re=2,770,000

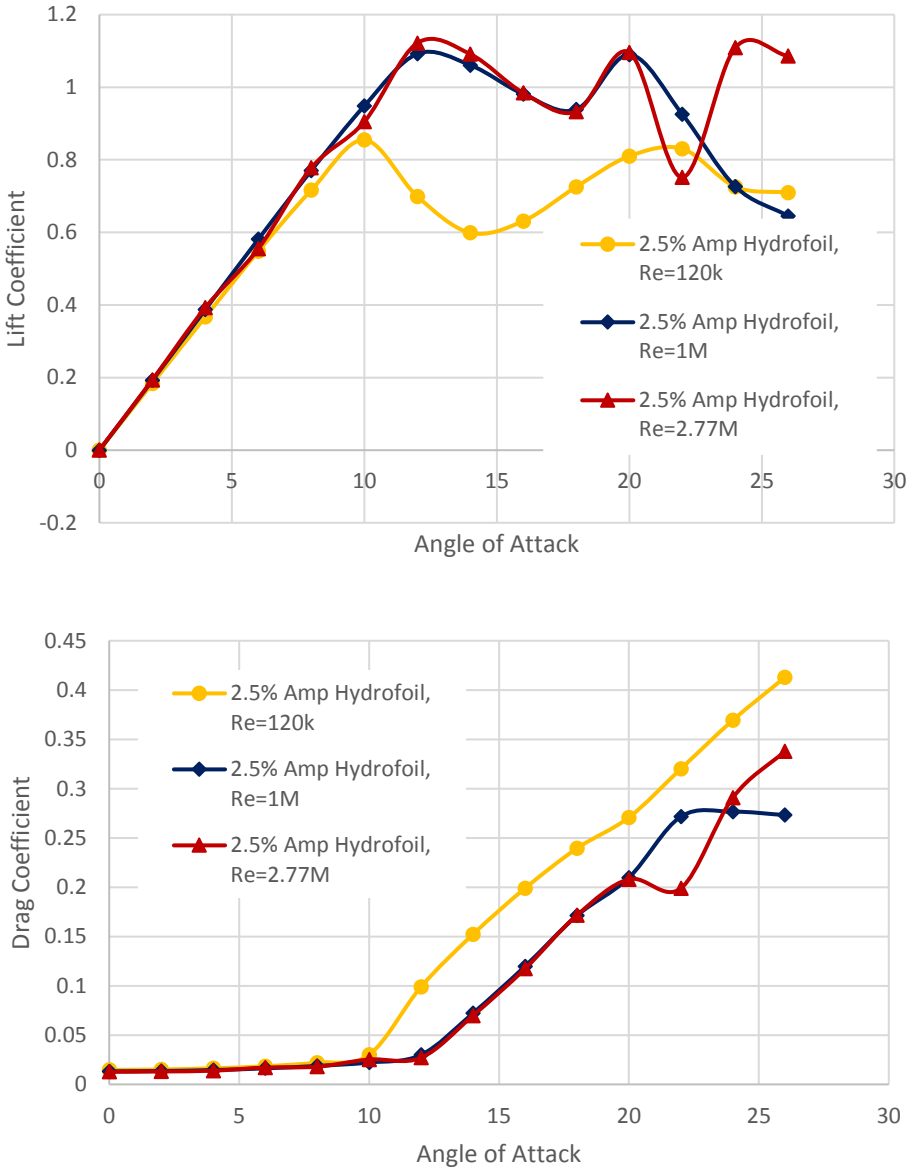

Figure 52: Comparison of the lift and drag coefficients for the hydrofoil with a sinusoidal leading-edge of 2.5% amplitude at Re=120,000, Re=1,000,000 and Re=2,770,000

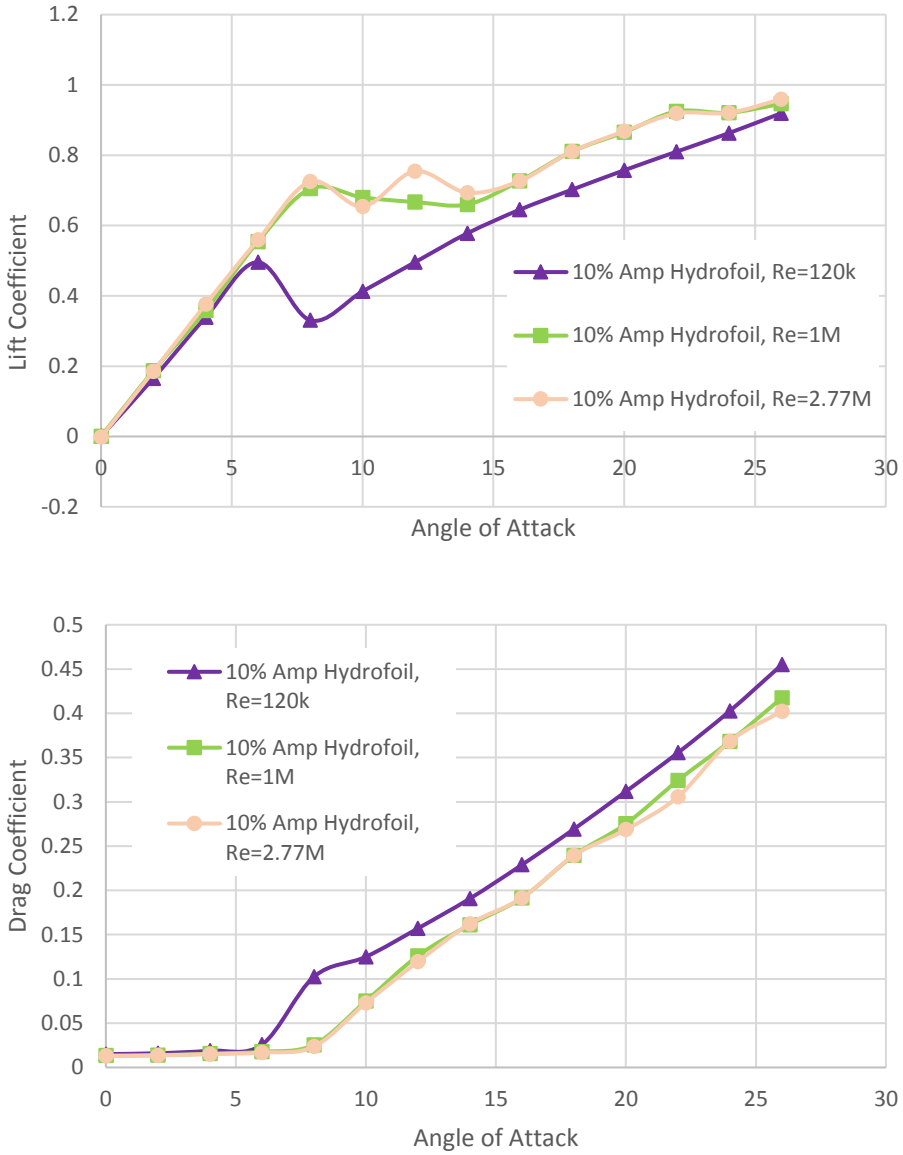

Figure 53: Comparison of the lift and drag coefficients for the hydrofoil with a sinusoidal leading-edge of 10% amplitude at Re=120,000, Re=1,000,000 and Re=2,770,000

4.9 Discussion of limitations of the model

While the agreement between the 2-D simulations in this study and the experimental results are good, the 3-D cases simulated have a higher error percentage. The lift and drag coefficient results between 5° and 20° angle of attack are substantially different from the validation sources which makes it difficult to determine if the pre- and post-stall behaviours are well captured.

One reason for the discrepancies could be that the separation bubble was not included as a factor in the simulations. It was deemed unnecessary to include as the research in Crivellini et al. (2014) [30] concluded that the Spalart-Allmaras turbulence model with a low turbulence intensity (as defined by the low values of ν_t and $\tilde{\nu}$) reasonably captures the behaviour of the laminar separation bubble. It is therefore unlikely that any errors were caused by the Spalart-Allmaras turbulence model. Originally, the k-ω SST solver was used but the error in the results was higher than the current results. Spalart-Allmaras solver yielded results closer to the experimental results and hence it was used.

Another cause could be that the turbulent intensity of the simulations was inconsistent with the intensity inside the wind-tunnel. The Spalart-Allmaras variable and kinematic turbulent viscosity were defined by 3 divided by the Reynolds number which corresponded to a low turbulent intensity. For the simulations with flow fields governed by high Reynolds numbers, the equivalent turbulent intensity would have been lower based on the relationship of ν_t and $\tilde{\nu}$ to Re. Hence a different definition resulting in a higher magnitude of these variables may have been more appropriate in these cases [32].

Another source of error could be that for the flow in the wake region over the top surface of the hydrofoils, the high adverse pressure gradients had magnitudes too large for a RANS solver to accurately resolve. One of the selection criteria for using the Spalart-Allmaras turbulence model was that it has success with adverse pressure gradients however, it is possible that for the high attack angles, it was beyond the model's capabilities.

Finally, while all the simulations converged, at high angles of attack, the convergence did not produce a realistic solution of the fluid behaviour. Converging on an unrealistic result would also account for the non-uniformity in the wall shear stress magnitude and pressure magnitude fields on the hydrofoils which had symmetry boundary conditions along the span.

[This page has been left blank intentionally]

5.0 Summary and Conclusions

Inspired by the protuberances along the pectoral flippers of humpback whales, the effects of leading-edge tubercles were simulated on hydrofoils of infinite span (eliminating tip vortices) under laminar and turbulent flow conditions. Two validation case hydrofoils with different leading-edges and four test case hydrofoils with different leading-edges were tested with sinusoidal protuberances, identical wavelengths and amplitudes of 0%, 2.5%, 4%, 5.71% and 10% of the chord length, all within the range found on the humpback's flipper.

Most previous experiments in this area had not extensively explored the effect of tubercles in fully developed turbulent flow, for that reason the simulations were run at Reynolds numbers of 120,000, 1,000,000 and 2,770,000. The simulations were run in OpenFOAM using Reynolds Averaged Navier-Stokes equations and the Spalart-Allmaras turbulence model.

The recorded values and compared for each hydrofoil simulation were the lift and drag coefficients, the wall shear stress magnitude, pressure coefficient magnitude and velocity magnitude. From past experiments, the resultant forces on the standard hydrofoil were used as verification that the Computational Fluid Dynamics simulations were working correctly and that the results were reliable. For the hydrofoils with leading-edge tubercles, flow separation at the trough on the leading-edge was observed at lower angles of attack than for a hydrofoil with a straight leading-edge, although only between the tubercles. This was contradictory to the hypothesis that the tubercles would delay stall by energising the flow. At the peaks the flow remained attached to the hydrofoil surface even after stall had occurred. The effect was the same in flow fields with both high and low Reynolds numbers.

One benefit for modified hydrofoils was that for low Reynolds number flow, there was a large drop in the coefficient of lift for a standard hydrofoil when stall occurred, whereas for hydrofoils with leading-edge tubercles, the drop was much smaller or appeared to be almost non-existent. Another advantage observed for hydrofoils with tubercles along the leading-edge was a generation of lift up to 50% higher than the standard hydrofoil in the post-stall regime in laminar/transitional flow. This was not seen in turbulent flow, as the standard hydrofoil was found to generate consistently

higher lift than any other design, both pre- and post-stall. The standard hydrofoil also generated the least amount of drag, in laminar and turbulent flow, and in both the pre- and post-stall regions. In this study the tubercles were found to cause significantly higher drag on a hydrofoil when compared to a model with a straight leading edge.

The friction lines on the hydrofoil surfaces in the wall shear stress magnitude figures, showed the strength and direction of the frictional forces acting on the surface of the hydrofoil. The friction line patterns remained strongly consistent between low and high Reynolds number flow fields. The simulations with standard hydrofoils showed parallel friction lines to the direction of the flow (for low angles of attack), whereas the hydrofoils with tubercles showed wave patterns beginning at the leading-edge trough and expanding outwards pre-stall and definite orientation towards the trough between the tubercles in the post-stall region indicating that flow was being channelled between the tubercles. This was also supported by the higher values of wall shear stress in the area where flow was being channelled.

The pressure fields reflected the results found from the wall shear stress fields. In laminar flow (Re=120,000) for the standard hydrofoil, the overall pressure was lower over the surface when compared with the same hydrofoil in turbulent flow (Re=1,000,000). The hydrofoils with tubercles experienced their lowest pressure in the troughs where the flow speed was maximum. The smallest leading-edge tubercles (2.5%) had a pressure field very similar to the unmodified hydrofoil, where the values of the pressure were almost uniform along the leading edge. The hydrofoils with leading-edge tubercle amplitudes of 4% and 10% showed signs of flow being channelled between the tubercles from the leading edge to the trailing edge.

The velocity fields for the standard hydrofoil show different wake sizes under different flow conditions (i.e. laminar and turbulent) for the same angle of attack. At the angles of attack pre-stall, the flow fields for laminar/transitional and turbulent flow conditions presents many similitudes. However, for higher angles of attack the hydrofoil in the laminar flow had a larger wake region, which began at the leading-edge and continued over the entire length of the hydrofoil denoting flow separation at the leading-edge and stall. In turbulent flow for the same high angles of attack, the wake began at about one third of the chord length, indicating longer flow attachment and therefore better hydrodynamic performance.

For the hydrofoils with the leading-edge tubercles, the flow patterns seemed to be similar regardless of the tubercle amplitude. For each tubercle cross-section pre-stall, the flow fields would look quite like an unmodified hydrofoil. Post-stall, the flow field taken at the trough of the hydrofoil was like the field for the standard hydrofoil in laminar flow post-stall whereas for the slice taken at the tubercle peak the flow field resembled the standard hydrofoil velocity profile in turbulent flow post-stall. The greatest delay of boundary layer separation was seen along the peak of the hydrofoil with leading edge tubercles 10% of the chord length, however it also experienced the largest wake in the tubercle trough.

In summary, the results generated through CFD confirm most previous findings on hydrofoils at low Reynolds numbers (laminar flow). The presence of tubercles caused stall at lower angles of attack than hydrofoils with a straight leading edge. As a result, the hydrofoil which generated the highest lift and lowest drag was a standard hydrofoil. Post-stall, the hydrofoils with sinusoidal leading edges had higher values of lift and drag than the standard hydrofoil. The hydrofoils with tubercles did not stall in the same manner as the standard hydrofoil. The flow separated at the troughs but remained attached at the peaks, even post-stall. This resulted in a less abrupt stall characterised by a lower loss of lift and higher lift values post-stall compared to the standard hydrofoil.

However, most of these benefits were not found at high Reynolds numbers (turbulent flow). In turbulent flow, as was observed in laminar flow, the standard hydrofoil had higher lift and lower drag pre-stall when compared to the hydrofoils with sinusoidal leading edges. The hydrofoils with tubercles also stalled at lower angles than the standard hydrofoil. But, they were beneficial for relatively low Reynolds numbers (120,000), improving the angles of attack at which the hydrofoil stalls. Post-stall, the standard hydrofoil had better hydrodynamic characteristics, with higher lift and lower drag than the sinusoidal leading-edge hydrofoils. The stall manner of the standard hydrofoil changed in turbulent flow from a sudden loss of lift and increase in drag to a gradual decline of lift and therefore the tubercles provided no obvious benefit in fully turbulent flow conditions. The reason for the more gradual loss of lift in this scenario is that for flow with higher Reynolds numbers, there is no laminar separation bubble and hence no abrupt loss of lift at the critical angle as there is for hydrofoils in flows with a Reynolds number of 120,000 [11].

The Reynolds numbers of 1,000,000 and 2,770,000 correspond to the hunting velocity and the maximum velocity of the humpback whale respectively. The hydrofoils were therefore tested under the same flow conditions to examine any advantages that the tubercles may provide. The results from the simulations do not support the hypothesis that the tubercles enhance the hydrodynamic performance of the whales' flipper. It appears that for an infinite span the tubercles are detrimental to the lift and drag characteristics.

5.1 Future Work and Suggestions

The first suggestion for future research in this area is to use a different method of simulation such as LES, using the results from this paper as the initial conditions, as RANS does not give the required level of accuracy to analyse the complex flow generated by the tubercles

In future simulations, the hydrofoil should be expanded to have at least 6 tubercles. Only two tubercles seemed to be associated with uncertainties on the predictions, particularly at high angles of attack. The hydrofoil should also be tested with a finite span and a tapered shape, fixed only at one end. This would give a more applicable results accounting for the tip vortices present at the end of the span of any physical hydrofoil.

For future work, it would be worth modelling a hydrofoil more closely resembling a humpback flipper like the hydrofoil in [6], and the hydrofoils presented here and comparing results. The shape of the hydrofoil and the aspect ratio have a significant influence on the hydrodynamic performance and a comparative study for that has not been presented here.

There was a theory (beyond the scope of the current study) that the tubercles along the leading-edge of a fan blade could assist in noise dampening. This is another direction the research could take, or another area to expand into as the application of tubercles on wind power generators and fan blades could eliminate significant noise pollution [33].

6 References

1. "Ask Nature". 2015. "Beak provides streamlining". https://asknature.org/strategy/beak-provides-streamlining/.
2. Hennighausen Amelia and Eric Roston. 2015. "Science and Energy." Bloomberg. https://www.bloomberg.com/news/photo-essays/2015-02-23/14-smart-inventions-inspired-by-nature-biomimicry.
3. Watts, P. and F. E. Fish. 2001. "The Influence of Passive Leading Edge Tubercles on Wing Performance." Proceedings of the Twelfth International Symposium on Unmanned Untethered Submersible Technology (UUST), UUST01, Autonomous Undersea Systems Inst., Lee,
4. Fish, F, and J. Battle. 1995. "Hydrodynamic-Design of the Humpback Whale Flipper." *Journal of Morphology*. 225(1): 51-60.
5. Karbus, George 2016. "George Karbus Photography." http://www.emerald-vision.com/category/cape-verde/.
6. Custodio, D. 2007. "The Effect of Humpback Whale-like Leading-edge Protuberances on Hydrofoil Performance." Master's Thesis. Worcester Polytechnic Institute.
7. Conforth, J. 2016. "Cornforth Wilderness Photography." http://cornforthimages.com/product/humpback-whale/humpback-whale-pectoral-fin-10/.
8. Miklosovic, D. S., M. M. Murray, L. E. Howle, and F. E. Fish. 2004. "Leading-edge tubercules delay stall on humpback whale (Megaptera novaeangliae) flippers." *Physics of Fluids 16*, L39. doi: 10.1063/1.1688341
9. Gad-el-Hak, M. 2006. *Flow Control: Passive, Active and Reactive Flow Management.* New York: Cambridge University Press.
10. Skillen, A., Revell, A., Pinelli, A., Piomelli, U. and J. Favier. 2014. "Flow over a Wing with Leading-Edge Undulations." *AIAA Journal, American Institute of Aeronautics and Astronautics*. 53 (2), pp 464-472 doi: 10.2514/1.J053142
11. Rostamzadeh, N., Hansen, K. L., Kelso R. M., and B. B. Dally. 2014. "The formation mechanism and impact of streamwise vortices on NACA 0021

airfoil's performance with undulating leading edge modification." *Physics of Fluids* 26, 107101 (2014); doi: 10.1063/1.4896748

12. Hansen, K. L., Rostamzadeh, N., Kelso, R. M., and B. B. Dally. 2016. "Evolution of the streamwise vortices generated between leading edge tubercles." *Journal of Fluid Mechanics. Vol. 788. pp 730-766.* doi: 10.1017/jfm.2015.611
13. Bushnell, D. M., and K. J. Moore. 1991 "Drag Reduction in Nature." *Annual Review of Fluid Mechanics*. 23: 65-79. doi: 10.1146/annurev.fl.23.010191.000433.
14. Fish, F. E. and G. V. Lauder. 2006. "Passive and active flow control by swimming fishes and mammals." *Annual Review of Fluid Mechanics*. 38: 193-224. doi: 10.1146/annurev.fluid.38.050304.092201.
15. Johari, H., C. Henoch, D. Custodio and A. Levshin. 2007. "Effects of Leading-Edge Protuberances on Airfoil Performance." *AIAA Journal* 45 (11): 2634-2641. doi: 10.2514/1.28497.
16. Van Nierop, E. A., Alben, S., and M. P. Brenner. 2008. "How Bumps on Whale Flippers Delay Stall: An Aerodynamic Model." *Physical Review Letters*. DOI: 10.1103/PhyRevLett.100.054502.
17. Rostamzadeh, N., R. M. Kelso, B. B. Dally, and K. L. Hansen. 2013. "The effect of undulating leading-edge modifications on NACA 0021 airfoil characteristics." Physics of Fluids 25. doi: 10.1063/1.4828703
18. Pedro, H. T. C. and M. H. Kobayashi. 2008. "Numerical Study of stall delay on humpback whale flippers." *American Institute of Aeronautics and Astronautics Paper 2008-5084.*
19. Rostamzadeh, N., Kelso, R. M., and B. B. Dally. 2017. "A numerical investigation into the effects of Reynolds number on the flow mechanism induced by a tubercled leading edge." *Theoretical and Computational Fluid Dynamics. February 2017, Vol. 31, Issue 1. pp 1-32.* doi: 10.1007/s00162-016-0393-x
20. Versteeg, H. K. and W. Malalasekera. 2007. *An introduction to Computational Fluid Dynamics: The Finite Volume Method*. London: Pearson Education Limited.
21. Muller, P. 2012. *The Equations of Oceanic Motions*. Cambridge: Cambridge University Press.

22. Anderson, J. D. Jr. 1991. “Incompressible Flow over Finite wings.” In *Fundamentals of Aerodynamics*, McGraw-Hill.
23. Mahesh, K. 2012. “The Interaction of Jets with Crossflow.” *Annual Review of Fluid Dynamics.* 45: 379-407.
24. Rumsey, C. 2014. “Langley Research Centre Turbulence Modelling Resource”. NASA. https://turbmodels.larc.nasa.gov.
25. Spalart, P. R. 2000. “Strategies for turbulence modelling and simulations.” *International Journal of Heat and Fluid Flow.* 21(3):252-263. doi: 10.1016/S0142-727X(00)00007-2.
26. Hansen, K. L., Kelso, R. M. and B. B. Dally. 2011. “Performance Variations of Leading-Edge Tubercles for Distinct Airfoil Profiles.” *University of Adelaide, Adelaide, South Australia 5005, Australia*. doi: 10.2514/1.J050631
27. Cai, C., Z. Zuo, S. Liu and Y.Wu. 2015. “Numerical Investigations of Hydrodynamic performances of hydrofoils with leading-edge protuberances.” *Advances in Mechanical Engineering 7*. doi: 10.1177/1687814015592088.
28. Gregorek, G. M., Hoffmann, M. J. and M. J. Berchak. 1989. “Steady State and Oscillatory Aerodynamic Characteristics of a NACA 0021 Airfoil: Data Report,” Ohio State University, Columbus, OH.
29. Wolfe, W. P. and S. S. Ochs. 1997. *Predicting Aerodynamic Characteristics of Typical Wind Turbine Airfoils Using CFD*. Sandia National Laboratories. http://prod.sandia.gov/techlib/access-control.cgi/1996/962345.pdf.
30. Crivellini, A., D’Alessandro, V., Di Benedetto, D., Montelpare, S. and R. Ricci. 2014. “Study of laminar separation bubble on low Reynolds number operating airfoils: RANS modelling by means of an high-accuracy solver and experimental verification*.” Journal of Physics: Conference Series 501 (2014) 012024.* doi:10.1088/1742-6596/501/1/012024
31. Laval, J-P., C. Braud, G. Fournier and M. Stanislas. 2010. “Large-eddy simulations of control of a separated flow over a 2-D bump by means of pulsed jets.” *Journal of Turbulence 11*. doi: 10.1080/14685248.2010.522579

32. Basse, N.T. 2018. "Turbulence Intensity Scaling: A Fugue", https://arxiv.org/abs/1801.06203
33. Hansen, K., Richard Kelso and Con Doolan. 2012. “Reduction of flow induced airfoil tonal noise using leading edge sinusoidal modifications.” *Acoustics Australia*. 40(3): 172-177.